



2  
2006



This is to certify that the  
dissertation entitled

**ELECTRO-OXIDATION AND DETECTION OF  
CHLORINATED PHENOLS USING BORON-DOPED THIN-  
FILM DIAMOND ELECTRODES**

presented by

**Grace Wangechi Muna**

has been accepted towards fulfillment  
of the requirements for the

Ph.D degree in Chemistry/Environmental  
Toxicology

*Greg M. Leonard*  
Major Professor's Signature

7-7-05

Date

**PLACE IN RETURN BOX** to remove this checkout from your record.  
**TO AVOID FINES** return on or before date due.  
**MAY BE RECALLED** with earlier due date if requested.

DATE DUE	DATE DUE	DATE DUE
<del>08 29 07</del> NOV 28 2007		

**ELECTRO-OXIDATION AND DETECTION OF  
CHLORINATED PHENOLS USING BORON-DOPED THIN-  
FILM DIAMOND ELECTRODES**

By

**Grace Wangechi Muna**

**A DISSERTATION**

Submitted to  
Michigan State University  
In partial fulfillment of the requirements  
For the degree of

**DOCTOR OF PHILOSOPHY**

**DEPARTMENT OF CHEMISTRY AND CENTER FOR  
INTEGRATIVE TOXICOLOGY**

**2005**

## **ABSTRACT**

# **ELECTRO-OXIDATION AND DETECTION OF CHLORINATED PHENOLS USING BORON-DOPED THIN- FILM DIAMOND ELECTRODES**

**By**

**Grace Wangechi Muna**

Historically, electrochemical detection methods for the chlorinated phenol (CP's) analysis have been plagued by fouling of the electrode. Diamond is a new electrode material that shows little tendency to be deactivated and fouled by adsorbed reaction products and intermediates during the oxidation of CP's. This new electrode reopens the door to electrochemical detection of these pollutants. In this work cyclic voltammetry with microcrystalline and nanocrystalline diamond electrodes was used to study the chlorophenol oxidation reaction in acidic media and to learn how the film morphology might affect the reaction mechanism. Amperometry with both diamond types was coupled with flow injection analysis, high performance liquid chromatography (HPLC-EC), and capillary zone electrophoresis (CE-EC), for the analysis of chlorinated phenols.

Diamond electrodes exhibited good responsiveness for the electro-oxidation of these compounds and resisted fouling during extended use. The electrode performance was evaluated in terms of the linear dynamic range, limit of quantitation, response precision and response stability. Both diamond types exhibited excellent detection figures of merit. For example in HPLC – EC, the

limit of quantitation for the 2-chlorophenol was 0.1  $\mu\text{M}$  (13 ppb) with a response precision of 4.1 % (n = 7) for the microcrystalline diamond electrode. In CE-EC using diamond microelectrode, the limit of quantitation for 2-chlorophenol was 0.1  $\mu\text{M}$  (13 ppb) and the response precision was 4.7% (n = 9).

Real samples were also analyzed. The HPLC – EC assay was used for the determination of 2-chlorophenol in a contaminated soil sample. Red Cedar water was spiked with CP's and was extracted by solid phase extraction (SPE) prior to analysis, and then assayed for using CE-EC. This lowered the limit of quantitation to mid to high ppt range. The results demonstrate that electrochemical detection methods using diamond electrode can be employed for the analysis of CP's.

## **ACKNOWLEDGMENTS**

My sincere appreciation and thanks go to my advisor Dr. Swain who provided academic directions and a good environment for me to grow in as a scientist, for his patience and great support. I admire and appreciate his quest for excellence, vast knowledge in analytical chemistry, personality, character and a great sense of humor. Thank you Greg!

I would also like to thank the members of my committee: Dr. McGuffin, Dr. Blanchard, Dr. Voice and Dr. Garrett. Thank you for all the comments concerning my research, and also for your kindness. Your input and support has been valuable for my development as a scientist. Thanks.

I would like to thank the former and present Swain group members: Dr. Jian Wang, Dr. Malgorzata Witek, Dr. Mateuz Hupert, Dr. Shannon Haymond, Dr. Josef Cvacka, Suzana Cvackova, Dr. Yoshiyuki Show, Karolina Peckova, Dr. Jesse Seegmiller, Dr. Prema Sonthalia, Dr. Jason Stotter, Pushwinder Kaur, Dr. Veronika Mocko, Jason Bennett, Ann Fischer, Audrey Martin, Jinwoo Park, Gloria Pimienta, Doug Knigge, Yang Song, Shihua Wang, Elizabeth McGaw, Hua Dong, Luther Schaeffer, and Yingrui Dai. Thank you all for your great support. Special thanks to Dr. Show who fabricated the diamond planar films and Dr. Mocko who fabricated the diamond microelectrodes. Thank you guys for your great support. I am indebted in my heart.

I would like to thank the Department of Chemistry here at Michigan State University for giving me an opportunity to attend graduate school.

Finally and most importantly, I thank God for His abundant grace and for giving me a wonderful and supportive family: My husband, Muna; daughter, Nishi; and son, Ushindi. Thank you guys for your love and moral support!

I dedicate this dissertation to my wonderful husband, Muna Kangethe who has faithfully encouraged and supported me over the years to achieve my academic dreams, and for his unending love.

*Grace Muna*



## Table of Contents

<b>List of figures</b> .....	<b>x</b>
<b>List of tables</b> .....	<b>xiv</b>
<b>CHAPTER 1</b> .....	<b>1</b>
<b>Background and Motivations</b> .....	<b>1</b>
1.1 Chlorinated Phenols.....	1
1.1.1 Environmental Importance.....	1
1.1.2 Chlorinated Phenols Analysis.....	3
1.2. Conductive Boron-Doped Diamond Electrodes.....	8
1.3 Diamond Electrode Deposition and Doping.....	12
1.4 Outline of the Dissertation.....	18
1.5 References .....	20
<b>CHAPTER 2</b> .....	<b>28</b>
<b>Experimental Procedures and Instrumentation</b> .....	<b>28</b>
2.1 Diamond Thin-Film Deposition.....	28
2.1.1 Planar Film Electrodes.....	28
2.1.1.1 Microcrystalline Diamond Thin-Films Electrodes.....	28
2.1.1.2 Nanocrystalline Diamond Thin-Film Electrodes.....	31
2.1.2 Boron-Doped Diamond Thin-Film Microelectrodes.....	33
2.2 Glassy Carbon Electrode Preparation.....	35
2.3 Characterization of the Diamond Thin-Film Electrodes.....	36
2.3.1 Scanning Electron Microscopy (SEM).....	36
2.3.2 Atomic Force Microscopy (AFM).....	36

2.3.3 Raman Spectroscopy.....	36
2.3.4 X-ray Diffraction (XRD).....	37
2.3.4 Electrical Resistivity.....	37
2.4.5 Contact Angle Measurements.....	38
2.4 Electrochemical Measurements.....	38
2.5 Flow Injection Analysis.....	40
2.6 High Performance Liquid Chromatography.....	42
2.7 Capillary Electrophoresis.....	43
2.8 Solid Phase Extraction.....	46
2.9 Materials and Chemicals.....	47
2.10 References.....	50
<b>CHAPTER 3.....</b>	<b>51</b>
<b>The Physical and Electrochemical Characterization of Boron-Doped Diamond Thin-Film Electrodes.....</b>	<b>51</b>
3.1 Introduction.....	51
3.2 Results and Discussion.....	53
3.2.1. Morphology and Microstructure.....	53
3.2.2 Electrochemical Responsiveness.....	58
3.3 Conclusions.....	70
3.4 References.....	71
<b>CHAPTER 4.....</b>	<b>74</b>
<b>Cyclic Voltammetric Studies of the Electro-oxidation of Chlorinated Phenols on Boron-Doped Diamond Thin-Film Electrodes.....</b>	<b>74</b>
4.1 Introduction.....	74

4.2 Results and Discussions.....	79
4.3 Conclusions.....	93
4.4 References.....	95
<b>CHAPTER 5.....</b>	<b>97</b>
<b>Detection of Chlorinated Phenols by Flow Injection Analysis and High Performance Liquid Chromatography Using Amperometric Detection with a Boron-Doped Diamond Thin-Film Electrode.....</b>	<b>97</b>
5.1 Introduction.....	97
5.2 Results and Discussion.....	100
5.2.1 Flow Injection Analysis with Electrochemical Detection.....	100
5.2.2 High Performance Liquid Chromatography with Electrochemical Detection.....	111
5.2.3 Soil Sample Analysis.....	117
5.3 Conclusions.....	120
5.4 References.....	121
<b>CHAPTER 6.....</b>	<b>123</b>
<b>Capillary Zone Electrophoresis Separation Chlorinated Phenols with Amperometric Detection Using a Diamond Microelectrode.....</b>	<b>123</b>
6.1 Introduction.....	123
6.2 Results and Discussions.....	126
6.2.1 Surface morphology and microstructure of diamond microelectrodes.....	126
6.2.2. Basic Voltammetric Response.....	128
6.2.3 Direct Amperometric Detection of Chlorinated Phenols.....	132
6.2.4 Indirect Amperometric Detection of Chlorinated Phenols.....	143

6.3 Conclusions.....	151
6.4 References.....	153
<b>CHAPTER 7.....</b>	<b>156</b>
<b>Chlorinated Phenol Analysis Using Solid Phase Extraction Coupled with Amperometric Detection.....</b>	<b>156</b>
7.1 Introduction.....	156
7.2. Results and Discussion.....	159
7.2.1 Separation and Amperometric Detection of Chlorinated Phenols.....	159
7.2.2. Off-line Coupling of SPE with CE-EC.....	162
7.3 Conclusions.....	169
7.4 References.....	171
<b>CHAPTER 8.....</b>	<b>173</b>
<b>Summary.....</b>	<b>173</b>

## List of Figures

<b>Figure 1.1</b> A schematic for the band structure of boron-doped diamond.....	17
<b>Figure 2.1</b> Microwave-assisted CVD apparatus.....	29
<b>Figure 2.2</b> Schematic of a boron-doped diamond microelectrode sealed in a pipette tip.....	35
<b>Figure 2.3</b> Design of the three-electrode, single compartment electrochemical cell.....	39
<b>Figure 2.4</b> A schematic of the FIA system.....	40
<b>Figure 2.5</b> Design of the thin-layer flow cell.....	41
<b>Figure 2.6</b> Capillary electrophoresis set up.....	44
<b>Figure 2.7</b> Design of the end-column electrochemical detection cell.....	45
<b>Figure 2.8</b> SPE extraction steps.....	47
<b>Figure 3.1</b> AFM images showing a (A) microcrystalline and (B) nanocrystalline diamond thin film deposited on Si.....	53
<b>Figure 3.2</b> Visible Raman spectra for a (A) microcrystalline and (B) nanocrystalline diamond thin film.....	56
<b>Figure 3.3</b> XRD patterns for a (A) microcrystalline and (B) nanocrystalline diamond thin-film electrode.....	58
<b>Figure 3.4</b> Background cyclic voltammetric i-E curve in 0.1 M HClO <sub>4</sub> for a microcrystalline diamond film deposited on Si.....	60
<b>Figure 3.5</b> Cyclic voltammetric i-E curves for (A) ) Fe(CN) <sub>6</sub> <sup>-3/-4</sup> (B) Ru(NH <sub>3</sub> ) <sub>6</sub> <sup>+2/+3</sup> (C) IrCl <sub>6</sub> <sup>-2/-3</sup> (D) methyl viologen in 1 M KCl, and (E) Fe <sup>+2/+3</sup> , (F) tert-butyl catechol in 0.1 M HClO <sub>4</sub> at a boron-doped microcrystalline diamond thin-film electrode.....	64
<b>Figure 3.6</b> Cyclic voltammetric i-E curves for (A) ) Fe(CN) <sub>6</sub> <sup>-3/-4</sup> (B) Ru(NH <sub>3</sub> ) <sub>6</sub> <sup>+2/+3</sup> (C) IrCl <sub>6</sub> <sup>-2/-3</sup> (D) methyl viologen in 1 M KCl, and (E) Fe <sup>+2/+3</sup> , (F) tert-butyl catechol in 0.1 M HClO <sub>4</sub> at a boron-doped nanocrystalline diamond thin-film electrode.....	65

<b>Figure 3.7</b> (A) Plots of $i_p^{ox}$ vs. scan rate <sup>1/2</sup> for $Fe(CN)_6^{-3/4}$ , $Ru(NH_3)_6^{+3/+2}$ , $IrCl_6^{-2/-3}$ , methyl viologen, $Fe^{+2/+3}$ , tert-butyl catechol at a boron-doped microcrystalline diamond thin-film electrode. (B) Experimental and theoretical comparison for $Fe(CN)_6^{-3/4}$ curves.....	69
<b>Figure 4.1</b> Phenoxy radical formation.....	74
<b>Figure 4.2</b> The different possible reaction pathways for phenol oxidation .....	75
<b>Figure 4.3</b> Cyclic voltammetric i-E curves for (A) microcrystalline diamond, (B) nanocrystalline diamond, and (C) GC in 0.05 M phosphate buffer, pH 3.5.....	80
<b>Figure 4.4</b> Cyclic voltammetric i-E curves for 2-CP, 4-CP, and phenol at (A) microcrystalline diamond, (B) nanocrystalline diamond electrodes in 0.05 M phosphate buffer, pH 3.5.....	83
<b>Figure 4.5</b> Cyclic voltammetric i-E curves for phenol, 2-CP, and 4-CP at (A) microcrystalline and, (B) nanocrystalline diamond electrodes in 0.05 M phosphate buffer, pH 3.5.....	85
<b>Figure 4.6</b> Cyclic voltammetric i-E curves for 0.1 mM PCP at (A) microcrystalline and (B) nanocrystalline diamond electrodes in 0.05 M phosphate buffer, pH 3.5.....	88
<b>Figure 4.7</b> AFM images after 25 cycles of 0.1 mM PCP in 0.05 M phosphate buffer, pH 3.5, at a microcrystalline diamond electrode.....	90
<b>Figure 4.8</b> Cyclic voltammetric i-E curves for 0.1 mM 3-CP at (A) microcrystalline and (B) nanocrystalline diamond electrodes in 0.05 M phosphate buffer, pH 3.5.....	91
<b>Figure 4.9</b> Cyclic voltammetric i-E curves for 0.1 mM 2-CP at GC in 0.05 M phosphate buffer, pH 3.5.....	93
<b>Figure 5.1</b> FIA-EC hydrodynamic voltammetric background i-E curves for microcrystalline and nanocrystalline diamond, and GC in 0.05 M phosphate buffer, pH 3.5.....	101
<b>Figure 5.2</b> Hydrodynamic voltammetric i-E curves for 40 $\mu$ M concentrations of each phenolic compound in 50 mM phosphate buffer, pH 3.5, at a (A) microcrystalline and (B) nanocrystalline diamond thin-film electrode.....	104
<b>Figure 5.3</b> S/B vs potential plots for 40 $\mu$ M concentrations of each phenolic compound in 50 mM phosphate buffer, pH 3.5, at a (A) microcrystalline and (B) nanocrystalline diamond thin-film electrode.....	105

<b>Figure 5.4</b> Calibration curves for phenol and chlorinated phenols obtained at microcrystalline diamond.....	107
<b>Figure 5.5</b> FIA-EC response for multiple injections of 40 $\mu$ M 2-CP. ....	110
<b>Figure 5.6</b> FIA-EC responses for multiple injections of 40 $\mu$ M phenol, 2-CP, 3-CP, 4-CP, and PCP on GC.....	111
<b>Figure 5.7</b> Reversed-phase chromatogram for phenol and the chlorinated phenols with amperometric detection using a microcrystalline diamond thin-film electrode.....	114
<b>Figure 5.8</b> Calibration curves for phenol and chlorinated phenols at a (A) microcrystalline and (B) nanocrystalline diamond thin-film electrode.....	115
<b>Figure 5.9</b> Reversed-phase chromatogram for the separation and amperometric detection of 2-CP in a contaminated soil sample at a microcrystalline diamond thin-film electrode.....	119
<b>Figure 6.1</b> SEM images of an electrochemically etched 76- $\mu$ m sharpened platinum wire coated with a polycrystalline diamond film.....	126
<b>Figure 6.2</b> Raman spectrum for a microcrystalline boron-doped diamond film deposited on a 76- $\mu$ m platinum wire.....	127
<b>Figure 6.3</b> (A) Background cyclic voltammeter I-E curve for a boron-doped diamond microelectrode in 1 M ACL. Scan rate = 100 mV/s. (B) Cyclic voltammeter I-E curve for 1 mM $\text{Fe}(\text{CN})_6^{3-/4-}$ in 1 M ACL at a boron-doped diamond microelectrode.....	130
<b>Figure 6.4</b> Cyclic voltammeter I-E curve for 50 $\mu$ M 2-chlorophenol in a 10/20 mM mixed-borate/phosphate run buffer, pH 8.4 at a boron-doped diamond microelectrode.....	132
<b>Figure 6.5</b> Hydrodynamic voltammeter I-E curves for the six chlorinated phenols at a boron-doped diamond microelectrode recorded in a 10/20 mM borate/phosphate run buffer, pH 8.4.....	135
<b>Figure 6.6</b> A typical electropherogram for phenol and six chlorinated phenols using direct amperometry recorded in a 10/20 mM borate/phosphate run buffer, pH 8.4.....	139
<b>Figure 6.7</b> Cyclic voltammetric i-E curve for 0.8 mM ferrocene carboxylic acid in 10 mM phosphate buffer, pH 8.1, at a boron-doped diamond microelectrode...	145

**Figure 6.8** An electropherogram for 3-chlorophenol, 2-chlorophenol, and 2,4-dichlorophenol using indirect amperometry recorded in a 10 mM phosphate run buffer, pH 8.1.....147

**Figure 7.1** An electropherogram for a standard solution of chlorinated phenols using direct amperometry recorded in a 10/20 mM borate/phosphate run buffer, pH 8.4.....161

**Figure 7.2** Calibration curve for a river water sample spiked with different concentrations of 2-CP.....164

**Figure 7.3** An electropherogram for a river water sample spiked with 0.1-0.2 ppm of chlorinated phenols after extraction, recorded in a 10/20 mM borate/phosphate run buffer, pH 8.4.....165



## List of Tables

<b>Table 1.1</b> EPA current national recommended water quality criteria.....	4
<b>Table 2.1</b> Microcrystalline Diamond Thin Film Deposition Parameters.....	31
<b>Table 2.2</b> Nanocrystalline Diamond Thin Film Deposition Parameters.....	33
<b>Table 2.3</b> Properties of Phenol and the Chlorinated phenols.....	49
<b>Table 3.1</b> Analytical Techniques Used for Film Characterization.....	52
<b>Table 3.2</b> Cyclic Voltammetric Data for the Microcrystalline Boron-Doped Diamond Electrode.....	66
<b>Table 3.3</b> Cyclic Voltammetric Data for the Nanocrystalline Boron-Doped Diamond Electrode.....	66
<b>Table 5.1</b> FIA-EC Data for Phenol and Chlorinated Phenols at a Microcrystalline Diamond Thin-Film Electrode.....	108
<b>Table 5.2</b> FIA-EC Data for Phenol and Chlorinated Phenols at a Nanocrystalline Diamond Thin-Film Electrode.....	108
<b>Table 5.3</b> Response precision for phenol and chlorinated phenols at microcrystalline and nanocrystalline diamond, and GC in 50 mM phosphate buffer, pH 3.5.....	110
<b>Table 5.4</b> HPLC-EC Detection Figures of Merit for Phenol and the Chlorinated Phenols at a Microcrystalline Diamond Thin-Film Electrode.....	116
<b>Table 5.5</b> HPLC-EC Detection Figures of Merit for Phenol and the Chlorinated Phenols at a Nanocrystalline Diamond Thin-Film Electrode.....	116
<b>Table 6.1</b> $pK_a$ Values and Elution Order for Phenol and the Chlorinated Phenols.....	135
<b>Table 6.2</b> Detection Figures of Merit for Phenol and the Chlorinated Phenols in Direct Amperometry Coupled with Capillary Electrophoresis.....	140
<b>Table 6.3</b> Detection Figures of Merit for Chlorinated Phenols in CZE with Indirect Amperometric Detection.....	151

**Table 7.1** Recovery of chlorinated phenols from 50 mL river water (pH 2.5) spiked with 0.1 – 0.2 ppm of the pollutants.....165

**Table 7.2** Detection Figures of Merit for Chlorinated Phenols using off-line SPE with Capillary Electrophoresis and Amperometric Detection.....167

# **CHAPTER 1**

## **Background and Motivations**

### **1.1. Chlorinated Phenols**

#### **1.1.1. Environmental Importance**

Chlorinated phenols are ubiquitous pollutants present in the wastewater from several industrial processes including the manufacture of dyes, plastics, pesticides, antioxidants, paper and petroleum products.<sup>1-3</sup> Leaching of these priority pollutants from point sources, such as landfills, is another source of contamination in ground and surface water. Pentachlorophenol and 2,4,6-trichlorophenol have been used as wood preservatives and pesticides, whereas 2,4-dichlorophenol and 2,4,5-trichlorophenol are used as precursors for the synthesis of herbicides.<sup>4</sup> Chlorinated phenols can also be formed by biotic and abiotic transformation of pesticides in agriculture. Photolytic degradation of substituted phenols is connected with the formation of lower chlorinated phenols and chlorinated catechols, dihydrobenzenes, hydroxybiphenyls and chlorophenoxyphenols.<sup>3</sup>

Chlorinated phenols are of particular importance in the environment because of their toxicity to most aquatic organisms and tendency to bioaccumulate in the food chain.<sup>5,6,7</sup> The more highly chlorinated phenols, such as trichlorophenols and pentachlorophenol (PCP), are also persistent. Large-scale use of chlorinated phenols over the years has led to the contamination of terrestrial and aquatic ecosystems.

Chlorinated phenols are readily absorbed when administered by oral, inhalation or dermal contact.<sup>8,9</sup> They accumulate mostly in the liver and kidney of experimental animals and to a lesser degree in the brain, muscle and fat.<sup>8</sup> PCP is enriched easily in adipose tissue of humans and animals. Chlorinated phenols are bound to glucuronide or sulphate in the liver. Their elimination from the organism occurs via the urine either in the free form or as sulphate and glucuronide conjugates.<sup>10</sup> The toxic effects of chlorinated phenols are directly proportional to the degree of chlorination. PCP is the most toxic of these compounds, presumably as a result of increased lipophilicity. An increase in the number of chloro-substituents can also promote the accumulation of these compounds in fish and other organisms, thus increasing their toxic effects.<sup>11</sup> The major mode of action of chlorinated phenols involves the uncoupling of oxidative phosphorylation and the inhibition of the electron transport system. The chlorophenolate ion is evidently responsible for the uncoupling reaction, while the undissociated molecule causes convulsions.<sup>8</sup>

Acute exposure to lesser chlorinated phenols in humans results in muscular twitching, spasms, tremors, weakness, ataxia, convulsions and collapse. Acute poisoning by PCP is characterized by general weakness, fatigue, ataxia, headache, anorexia, sweating, hyperpyrexia, nausea, vomiting, tachycardia, abdominal pain, terminal spasms and death. Soft-tissue sarcomas, Hodgkin's disease, and leukaemia have been reported in epidemiological studies of occupational groups exposed to chlorinated phenols and phenoxy acids.<sup>12</sup> Some chlorinated phenols have been suspected of embryotoxicity and tetragenicity properties.<sup>8</sup> Studies dealing with chronic toxicity of some phenol congeners have confirmed their carcinogenic (hepatocellular tumors, leukaemia) and immunosuppressive properties.<sup>3,8</sup> For example, PCP has been classified as a B2 probable carcinogen for humans on the basis of a large body of evidence from animal toxicity studies and human clinical data.<sup>13</sup> PCP can also provoke damage to the eyes, pharynx and larynx.<sup>9</sup>

### **1.1.2. Chlorinated Phenols Analysis**

Development of sensitive, reproducible and stable detection methods for chlorinated phenols is an important area of research. Several chlorinated phenols, such as 2-chlorophenol, 2,4-dichlorophenol, 2,4,6-trichlorophenol, and pentachlorophenol, have been classified as priority pollutants by the Environmental Protection Agency.<sup>14</sup> For example, PCP is regulated in drinking water with a maximum allowable contaminant level (MCL) of 1 µg/L (1 ppb).<sup>15</sup> The EPA has also set the maximum limit in drinking water of 2-chlorophenol at

40 µg/L and 2,4-dichlorophenol at 20 µg/L for “lifetime exposure” which is defined as the concentration of a chemical in drinking water that is not expected to cause any adverse noncarcinogenic effects for a lifetime exposure.<sup>16</sup> Chlorinated phenols can also impart foul taste and odor to drinking water and food products (fish), even at low concentrations.<sup>6,7</sup> Table 1.1 shows the current EPA recommended water quality criteria for organoleptic effect of some chlorinated phenols.<sup>17</sup>

**Table 1.1 EPA Recommended Water Quality Criteria**

<b>Compound</b>	<b>Organoleptic effect criteria (µg/L)<sup>a</sup></b>
Phenol	300
2-chlorophenol	0.1
3-chlorophenol	0.1
4-chlorophenol	0.1
2,4-dichlorophenol	0.3
2,4,6-trichlorophenol	2
Pentachlorophenol	30

<sup>a</sup> maximum allowed concentration in water that does not cause any organoleptic effect in water

The most commonly used separation and detection methods for phenol and chlorinated phenol analysis are reversed-phase liquid chromatography (HPLC) and gas Chromatography (GC).<sup>18-28</sup> In LC, UV detection is usually employed. The sensitivity for UV-Vis for chlorinated phenols is low leading to detection limits in low ppm range.<sup>18-21</sup> In GC, various detection techniques are employed, such as flame ionization (FID), electron-capture (ECD), atomic

emission, or mass spectrometry (MS). In order to enhance the volatility and detectability of phenols, derivatization is usually necessary.<sup>22-28</sup> Derivatization procedures increase the complexity of the assay, the analysis time, and the risk for possible indeterminate error. The EPA-recommended protocols (methods 604 and 625) for phenol and chlorinated phenol speciation and detection involve liquid-liquid extraction (LLE) or solid phase extraction (SPE) followed by either GC with electron capture or mass spectrometric (MS) detection of derivatized phenols.<sup>29,30</sup> Typical detection limits are in the range of 0.2 – 5 µg/L (0.2 -5 ppb). These methods utilize expensive instrumentation and complex sample treatment, which involves preconcentration and derivatization of phenols to pentafluorobenzoyloxy derivatives. Another protocol (method 8041) involves methylation of the chlorinated phenols using diazomethane prior to GC analysis.<sup>31</sup> Unfortunately, this derivatization agent is carcinogenic and explosive.<sup>32</sup> Even with these accepted protocols, there remains a need for an inexpensive, reliable, fast, and sensitive method for monitoring chlorinated phenols in the aqueous environments.

Separation science coupled with electrochemical detection is a practical approach for the speciation and detection of chemical contaminants (electroactive ones) in water supplies. The instrumentation required is relatively inexpensive, easy to use, and field deployable. Electrochemical detection can be readily combined with separation techniques (e.g., HPLC, CE). Due to the high sensitivity of electrochemical detection, detection limits in mid to high ppb range

are possible.<sup>33-36</sup> The limiting factor in implementing electrochemical detection for water quality monitoring is often the electrode material in terms of the stability of its structure and properties, and its electrochemical responsiveness. This is particularly true for the detection of phenol and chlorinated phenols. Phenols are electro-oxidizable at positive potentials (+ 1.0 V vs. Ag/AgCl) in aqueous media, making electrochemistry a viable detection method. Unfortunately, electrochemical detection of this class of pollutants is often plagued by the strong irreversible adsorption (i.e. fouling) of reaction intermediates and products.<sup>37</sup> Mechanistic studies by several groups reveal that the phenol oxidation reaction proceeds initially through the formation of a phenoxy radical species, which can subsequently undergo radical-radical coupling to form polymeric and oligomeric species.<sup>37-42</sup> Fouling by oligomeric and/or polymeric (e.g. polyphenol) leads to poor electrode response reproducibility and stability, and sometimes complete response attenuation. In such cases, the electrode must be reconditioned (e.g. mechanical polishing), recalibrated and revalidated.

Most of the reported electrochemical detection studies of chlorinated phenol analysis have used modified electrodes due to the complications with direct detection on bare electrodes.<sup>33-36</sup> Lu and co-workers modified a Pt electrode with the conducting polymers, polyaniline and polypyrrole, to alleviate electrode fouling during phenol oxidation.<sup>35</sup> The phenol oxidation response was unchanged during multiple injections, and low detection limits (10 ppb) were achieved in flow injection analysis with amperometric detection (FIA-EC). In



another report, Saby and co-workers immobilized glucose oxidase on a glassy carbon electrode for the detection of chlorinated phenols.<sup>33</sup> The detection limits were in nanomolar range (4 – 65 nM) for several chlorinated phenols. Given the electrode fouling issue and the need to have an inexpensive, sensitive, and reproducible analysis method for the chlorinated phenols, it would be advantageous to have an electrode that is resistant to fouling but is still responsive to the analytes of interest. Boron-doped, hydrogen-terminated, polycrystalline diamond thin-film is an advanced electrode material that is more microstructurally stable and exhibits less tendency to foul than do other carbon materials.<sup>43,44</sup> This is due, at least in part, to the fact that the electrodes are relatively non-polar when hydrogen terminated and contain no extended  $\pi$ -electron system. Adsorption studies conducted in our laboratory using anthraquinone-2,6-disulfonate (AQDS) on glassy carbon, graphite and diamond electrodes showed that physisorption of AQDS was not observed on diamond presumably because of the relative absence of polar carbon-oxygen functional groups which promote strong dipole-dipole and ion-dipole interactions with the adsorbate.<sup>44</sup>

More important is that diamond exhibits superb response stability. The advantage of this property for electroanalysis is the fact many analytes are detectable via electrooxidation at positive potentials. A problem with  $sp^2$ -bonded carbon electrodes for example, is the alteration in the surface microstructure and chemistry that occurs over a wide potential range. These changes lead to

progressive increases in the background current (i.e., decreasing S/B), pH-dependence of background and faradaic signals, a greater susceptibility to fouling due to molecular adsorption, and sometimes an attenuation in the analyte response. While the diamond surface chemistry can easily be changed, the microstructure and morphology are extremely stable, leading to excellent long-term response precision and stability.<sup>45,46</sup>

*The objective for this research was to investigate the use of the boron-doped diamond electrodes for the electrochemical detection of chlorinated phenols in water supplies. More specifically, this research sought (i) to gain a fundamental understanding of how the chlorinated phenols oxidation reaction kinetics and mechanism are affected by the physicochemical properties of the diamond electrode and (ii) to develop a sensitive and stable monitoring method for chlorinated phenols by coupling separation techniques, such as liquid chromatography and capillary electrophoresis with electrochemical detection.*

## **2. Conductive Boron-Doped Diamond Electrodes**

$sp^2$  bonded carbon materials in the forms of highly ordered pyrolytic graphite (HOPG), glassy carbon (GC), carbon paste, and carbon fibers, have been used for over four decades in electrochemical measurements. Carbon electrodes are used in electrosynthesis, electroanalysis, and electrochemical-based energy storage and conversion devices.<sup>47</sup>  $sp^2$  carbon electrodes have several important properties such as being (i) available in a variety of forms, (ii)

inexpensive (iii) chemically modifiable to control electron-transfer and molecular adsorption and (iv) stable over a wide potential range.<sup>48-53</sup>

Single crystal graphite and HOPG are benchmark carbon materials that possess an anisotropic structure and properties. These well ordered materials have dimensions on the order of a few  $\mu\text{m}$ 's ( $> 1 \mu\text{m}$ ) compared to tens of  $\text{\AA}$  for more disordered materials, like GC and carbon black. HOPG consists of stacked graphite sheets with an interplane distance of  $3.354 \text{ \AA}$ . GC resembles a twisted, bent, interlocked mass of graphite ribbons. The interplane spacing is  $3.48 \text{ \AA}$ , slightly larger than that of HOPG. The graphite ribbons are composed of basic structural units made up of 10-20 rings stacked up more or less in parallel by two to four layers. GC contains graphite like domains ranging from 25 to  $100 \text{ \AA}$ . GC is one of the most widely used  $\text{sp}^2$  carbon electrode materials for electroanalysis.<sup>53</sup> It has low porosity, a reversible surface and is chemically inert in most common solvents.

Diamond is a new carbon material that possesses unique properties for a wide range of applications. It consists of a tetrahedrally bonded, face-centered cubic (FCC) crystal structure. Diamond possesses  $\text{sp}^3$ -bonded carbon and has unique properties including chemical inertness, extreme hardness, a wide bandgap, optical transparency, low dielectric constant, high thermal conductivity, and high carrier mobility. These properties are as a consequence of the small interatomic distance of the carbon atoms in the lattice and the hydrogen surface

termination.<sup>54-56</sup> A unique property of diamond is its morphological and microstructural stability as compared to conventional electrode materials. The stability arises from the high density and the strong directional  $sp^3$  C-C bonding. Diamond electrodes, for example, are stable during anodic polarization in harsh acidic and alkaline media. Surface damage, pitting, grain roughing and delamination are not normally observed even after lengthy electrolysis times producing chlorine and ozone.<sup>57,58</sup>

Diamond possesses a number of practical electrochemical properties that distinguish it from other commonly conventional  $sp^2$ -bonded carbon electrode materials. These properties include (i) a low and stable background current that leads to improved signal-to-background (SBR) and signal-to-noise (SNR) ratios, (ii) a wide working potential window in aqueous and nonaqueous media, (iii) superb microstructural and morphological stability at high temperature and current density, (iv) good responsiveness for several aqueous and nonaqueous redox analytes without conventional pretreatment, (v) weak adsorption of polar molecules due to the hydrophobic and non-polar nature of the hydrogen-terminated surface, and (vi) long-term response stability.<sup>59</sup> and references therein The wide working potential window of diamond in aqueous media stems from the large overpotential for the hydrogen evolution (HER) and oxygen reduction reactions (OER). The as-deposited diamond surface is hydrogen-terminated and is not favorable for physical and chemical interactions promoting adsorption and stabilization of radicals. Thus, electrochemical processes that involve adsorbed

intermediates or radical intermediates are generally kinetically hindered at diamond.<sup>60,61</sup> The poor stabilization of reaction intermediates, like those involved in water electrolysis (oxygen or hydrogen evolution), leads to the large working potential window in aqueous media.<sup>62</sup> For high quality diamond, the potential window is usually 3.5 V or more. The wide working potential window and superb morphological and microstructural stability of the diamond surface permits electrochemical reactions at extreme potentials that otherwise would be difficult to accomplish. Within the working potential window, diamond generally shows a small double layer capacitance and low background current.<sup>63</sup> The capacitance ranges from 1 to 5  $\mu\text{F}/\text{cm}^2$  for diamond as compared to GC which ranges from 30 to 40  $\mu\text{F}/\text{cm}^2$ . The background current for diamond is generally an order of magnitude lower than that for GC. The reasons for the low capacitance for diamond are explained in Chapter 3. The low background current and noise magnitudes give improved signal-to-background and signal-to-noise ratios.<sup>64</sup>

Several factors influence the electrochemical properties of polycrystalline diamond films including: (i) the dopant type, level, and distribution, (ii) the surface termination (H vs. O), (iii) non-diamond carbon impurity phases, (iv) the grain boundaries and other morphological defects, and (vi) the primary crystallographic orientation. The complexity of the diamond electrode properties resulting from these factors is known, but not completely understood. Several groups have contributed to the development of and applications for diamond electrodes (i.e. aspects of growth and nucleation mechanisms of diamond, the factors

influencing the electrochemical response, application in electroanalysis and electrocatalysis), including, Fujishima et al.,<sup>94-97</sup> (Japan), Pleskov et al.,<sup>75-78</sup> (Russia), Angus et al.,<sup>79-82</sup> (USA), Miller, et al.,<sup>97-101</sup> (USA), Gruen et al.,<sup>90-96</sup> (USA), and Compton et al.,<sup>83-89</sup> (England).

Diamond shows more versatility as an electrode than any other material. It can be used in electroanalysis to provide sensitive detection of analytes with superb precision and stability; for high current density electrolysis in aggressive solution environments without any microstructural or morphological degradation, and as a optically transparent electrode for spectrochemical measurements in the UV/Vis and iR regions of the electromagnetic spectrum.<sup>105-107,115,116</sup> Diamond electrodes have been used successively used for the amperometric detection of several analytes (e.g. azides,<sup>107</sup> chlorinated phenols,<sup>44,110-113</sup> chlorpromazine,<sup>59</sup> aliphatic amines<sup>117</sup> carbamate pesticides<sup>66</sup>, cysteine<sup>72</sup>). Diamond has also been used for the detection of trace metal ions by anodic stripping voltammetry.<sup>118,119</sup> In general, hydrogen-terminated diamond electrodes provide superior detection figures of merit in terms of the linear dynamic range, response precision, response stability, and limit of detection, as compared to all other sp<sup>2</sup> carbon materials.

### **1.3. Diamond Electrode Deposition and Doping**

Diamond electrodes for electrochemical applications can be formed in several different geometries: (i) a planar thin film deposited on a conducting

substrate, like Si (macroelectrode) (ii) thin films deposited on sharpened metal wire, like Pt (microelectrode), (iii) a thin film deposited on high surface area metal meshes (gas diffusion electrode), and (iv) a pattern of electrically-isolated diamond array elements (e.g., discs) on a planar support (microelectrode array).

Synthetic diamond can be produced by high-pressure, high temperature (HPHT) techniques or by low pressure chemical vapor deposition (CVD). During the HPHT process, solid carbon is heated under extreme pressure in the presence of a molten salt catalyst. The diamond crystals produced are used for a wide range of industrial applications that require thermal conductivity, hardness and wear resistance. A drawback, however, is the cost and the fact that the method produces diamond only in a single crystal.<sup>54, 121,122</sup> CVD techniques used to produce diamond require activation of gas phase precursor molecules. This activation can be accomplished thermally (e.g., a hot filament), by electric discharge (e.g. DC, RF, or microwave) or by a combustion flame (e.g. an oxyacetylene torch).<sup>54,120,121</sup> Microwave plasma CVD (MWCVD) is the most widely used method for diamond growth. In this method, microwave power is coupled into the chamber via a dielectric window to create a plasma discharge. The microwaves transfer energy into electrons in the gas phase, which in turn transfer their energy to the gas molecules through collisions. This leads to heating and dissociation of the gas molecules, and the formation of the active species, that react on the substrate to form diamond.<sup>54,120,121</sup>

Diamond is deposited from a hydrogen-rich hydrocarbon source gas mixture (CH<sub>4</sub>/H<sub>2</sub>).<sup>123-125</sup> It is recognized that hydrogen, specifically atomic hydrogen formed in the plasma, plays an essential role in diamond growth. Hydrogen atoms react with neutral species such as CH<sub>4</sub> to create CH<sub>3</sub>• reactive radicals in close proximity to the substrate surface and can attach to surface sites. Atomic hydrogen is known to gasify graphitic sp<sup>2</sup>-carbon. The gasification (formation of CH<sub>4</sub> or C<sub>2</sub>H<sub>2</sub>) rate for sp<sup>2</sup> bonded carbon is significantly higher than sp<sup>3</sup> bonded carbon. This means that the non-diamond carbon that does form is rapidly removed from the surface. Atomic hydrogen also serves to activate gas phase reactants by hydrogen abstraction and to activate growth or attachment sites on the surface by hydrogen abstraction.

Diamond films, grown by CVD, can be formed in two morphologies: microcrystalline and nanocrystalline. CH<sub>4</sub>/H<sub>2</sub> source gas mixtures are used to produce microcrystalline diamond thin film. This film possesses a well-faceted, polycrystalline morphology with a nominal crystallite size of ~ 2 μm, or greater. CH<sub>4</sub>/H<sub>2</sub>/Ar source gas mixtures are used to produce nanocrystalline diamond thin film.<sup>126,127</sup> The fraction of atoms in the grain boundaries of microcrystalline films relative to the bulk is extremely small. The nanocrystallinity is a result of a new growth and nucleation mechanism that involves insertion of the carbon dimer, C<sub>2</sub>, into surface carbon-carbon and carbon-hydrogen bonds. Very high heterogeneous renucleation rates are observed and the resulting films consist of randomly oriented, phase pure diamond grains with well-defined grain



boundaries.<sup>90,128</sup> Very simply, to grow nanograined films, the growth conditions are adjusted such that the rate of renucleation exceeds the rate of crystal growth. The opposite is the case for the growth of microcrystalline films. The nanocrystalline diamond consists of randomly oriented 3 – 10 nm crystallites, compared with the columnar microstructure of the microcrystalline film. The difference in individual crystallite size means that secondary nucleation rates associated with growth from hydrogen-poor plasmas are much higher than from CH<sub>4</sub>/H<sub>2</sub> plasmas.<sup>90,128</sup> Grain boundaries of a nanocrystalline are different from those of microcrystalline. It was found that they are mainly three fold coordinated and form  $\pi$  bonds. The electronic band structure of grains was characterized by a smaller band gap than the bulk diamond and it was shown that these states can participate in hopping conduction.<sup>90,128</sup> The special nature of  $\pi$ -bonded grain boundaries imparts unique electrical properties on nanocrystalline diamond films, and the conducting grain boundaries will rule the electronic properties of undoped film. With increasing crystallite size their number vastly increases, and the entire film becomes electrically conducting. Changes in nanocrystallites, therefore, can dramatically alter film properties.<sup>90,128</sup> More detailed discussion of the film morphology and microstructure, along with evaluation of the electrochemical properties of boron-doped microcrystalline and nanocrystalline diamond is presented further in Chapter 3.

Diamond is a very good electrical insulator with a band gap of 5.5 eV. Impurities, such as boron, can be incorporated into the film during growth that

impart semiconducting or semimetallic electronic properties depending on the doping level. Naturally occurring impurities that have implications for the host diamond consists of N, H, and B.<sup>90,129</sup> The N incorporation gives diamond n-type electronic character. Substitutional nitrogen is a deep donor with ionization energy of about 1.7 eV. The donors are typically too deep to provide any useful semiconducting properties to the material at room temperatures. Among the common dopants, boron is the most often used and can be introduced into diamond without significant distortion of the lattice. Boron may be introduced into CVD diamond film from a gaseous source, like B<sub>2</sub>H<sub>6</sub>, a solid state source, such as B<sub>2</sub>O<sub>3</sub> or h-BN, or from a boron containing solution such as B<sub>2</sub>O<sub>3</sub> dissolved in organic solvents from which vapors are carried into the reaction chamber by the growth gases.<sup>130</sup> Boron atoms substitutionally insert for some of the carbon atoms in the growing diamond lattice. These boron atoms function as electron acceptors, with an activation energy of 0.37 eV or less, depending on the doping level, and, at room temperature, contribute to the formation of free-charge carriers (i.e., holes or electron vacancies).<sup>131</sup> The film's electrical conductivity is directly related to the carrier concentration and the carrier mobility. For both types of diamond, typical carrier concentrations are in the range of 10<sup>18</sup> to 10<sup>20</sup> cm<sup>-3</sup> with carrier mobilities (holes) of 10-500 cm<sup>2</sup>/V-s. Of course, the mobility is limited by the defect density within the film. Activation energy of acceptors is observed to decrease with increasing boron concentration. This decrease of the energy can be explained by acceptor band width increase, impurity band formation and conduction as a result of it. For highly doped films, activation

energies as low as 2 meV have been reported.<sup>132</sup> For these highly doped films, the impurity band merges with the valence band, and metallic conduction is observed. The abundance of boron during diamond deposition can degrade the film quality which is manifested by increased point defects and, in extreme instances, by graphitization of the diamond film.<sup>129,133</sup> Figure 1.1 shows the bandgap diagram for boron-doped diamond electrode.

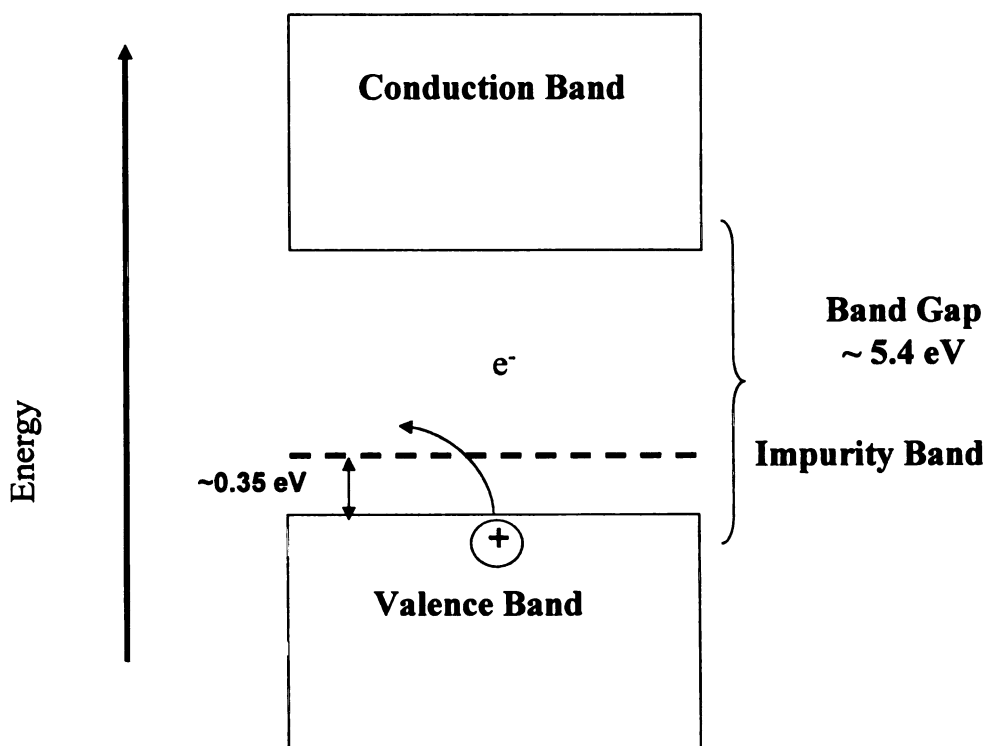


**Figure 1.1** A schematic for the band structure of boron-doped diamond.

Highly boron-doped polycrystalline diamond electrodes are more or less degenerate semi-metals. They deviate from ideal p-type semiconductor behavior

because of a high density of mid-gap electronic states. The mid gap density of states results from at least four factors: (i) boron doping level, (ii) lattice hydrogen content, (iii) inherent grain boundaries and other defects in the polycrystalline films, and (iv) non-diamond carbon impurity at the surface.<sup>59,109</sup> Among these factors, the surface non-diamond carbon phases exert little influence on the response of doped diamond films.<sup>134</sup> The role of morphological defects and grain boundaries on the electrode kinetics, specifically the electrical conduction, at polycrystalline film is still not clearly understood. Diamond is host for a variety of extended defects such as stacking faults, microtwins, dislocation, grain boundaries, and mixed habit growth features.<sup>59</sup> and references therein These defects could serve as discrete sites for electron transfer or could simply affect the electronic properties of the material by increasing the density of states. The mid-gap density of states arising from grain boundaries and defects, is relatively low compared to the number of states arising from the boron doping and lattice hydrogen.

#### **1.4. Outline of the Dissertation**

Details of experimental approaches used are given in Chapter 2. A discussion of the basic electrochemical and physical properties of boron-doped microcrystalline and nanocrystalline diamond thin films is given in Chapter 3. In Chapter 4, the voltammetric studies of several different chlorinated phenols are reported for both microcrystalline and nanocrystalline diamond. The analysis of the chlorinated phenols in standard solutions by flow injection analysis (FIA) and

liquid chromatography (LC), both with amperometric detection, is discussed in Chapter 5. The analysis of the chlorinated phenols in standard solutions by capillary electrophoresis (CE) with amperometric detection is described in Chapter 6. Finally, in Chapter 7, results for the analysis of chlorinated phenol using off-line solid phase extraction (SPE) and capillary electrophoresis with amperometric detection are presented. A brief conclusion follows, summarizing the results and the main contribution of the work.

## 1.5. References

1. Masque, N.; Pocurull, E.; Marce, R.; Borull, F.; *Chromatographia*, **1998**, *47*, 176.
2. Galceran, M.; Jauregui, O.; *Anal. Chim. Acta* **1995**, *304*, 75.
3. Veningerova, M.; Prachar, V.; Uhnak, J.; Lucacsova, M.; Tmovec, T.; *J. Chromatogr. B* **1994**, *657*, 103.
4. Lindstrom, K.; Nordin, J.; *J. Chromatogr.* **1976**, *128*, 13.
5. Vuorinen, P.J.; *Chemosphere* **1985**, *14*, 1729.
6. Sarkka, J.; *Chemosphere* **1985**, *14*, 469.
7. Realini, P.A.; *J. Chromatogr. Sci.* **1981**, *19*, 124.
8. WHO, *Environmental health criteria for chlorophenols other than pentachlorophenol*, Supplement Draft, July 31, **1986**.
9. WHO, *Environmental health criteria for pentachlorophenol*. Draft, March 19, **1986**.
10. Braun, W.H.; Blau, G.E.; Chenowith, M.B. *Toxicol. Appl. Pharmacol.* **1978**, *45*, 278.
11. Kishino, T.; Kobayshi, K.; *Wat. Res.* **1996** *30*, 393.
12. WHO. *Guidelines for drinking-water quality. Vol. 2. Health criteria and other supporting information*. Geneva **1984**.
13. Tanjore, S.; Viraraghavan, *Int. J. Environ. Stud.* **1994**, *45*, 155.
14. Noguera, P.; Maquieira, A.; Puchades, R.; Brunet, E.; Carramolino, M.; Rodriguez-Ubis, J.C.; *J. Environ. Monit.* **2002**, *4*, 442.
15. National Primary Drinking Water Regulations, Technical Factsheet on Pentachlorophenol, Office of Ground and Drinking Water, U.S. EPA, **1998**.
16. Drinking Water Standards and Health Advisories, Summer 200, U.S. EPA, **2000**.
17. [http:// www.epa.gov/water/science/criteria/wqcriteria.html](http://www.epa.gov/water/science/criteria/wqcriteria.html) accessed June 27<sup>th</sup>.

18. Andres, M.P.; Leon-Gonzalez, M.E.; Perez-Arribas, L.V.; Polo-Diez, L.M.; *J. High Resol. Chromatogr.* **2000**, *23*, 367.
19. Coman, V.; Moldovan, Z.; *J. High Resol. Chromatogr.* **2000**, *23*, 699.
20. Xueliang, L.; Frank, H.; *J. High Resol. Chromatogr.* **1998**, *21*, 309.
21. Frebortova, J.; Tatarkovicova, V.; *Analyst*, **1994**, *19*, 1519.
22. Angelino, S.; Gennaro, M.C.; *Anal. Chim. Acta.* **1997**, *346*, 61.
23. Turnes, I.; Rodriguez, I.; Gracia, C.M.; Cela, R.; *J. Chromatogr. A* **1996**, *743*, 283.
24. Hoogerbrugge, R.; Gort, S.M. Van der Velde, E.G.; Zoonen, P.; *Anal. Chim. Acta.* **1999**, *388*, 119.
25. Rodriguez, I.; Turnes, M.I.; Mejuto, M.C.; Cela, R.; *J. Chromatogr. A* **1996**, *721*, 297.
26. Hedges, J.I.; Ertel, J.R.; *Anal. Chem.*; **1982**, *54*, 174.
27. Ruana, J.; Urbe, I.; Borrull, F.; *J. Chromatogr. A*, **1993**, *665*, 217.
28. Pocurull, E.; Sanchez, G.; Borrull, F.; Marce, R.M.; *J. Chromatogr. A* **1995**, *696*, 31.
29. EPA Method 604, Phenols, in Federal Register, Environmental Protection Agency, Part VIII, 40 CFR Part 136, Washington DC, **1984**, 58.
30. EPA Method 625, Base/Neutrals and Acids, in Federal Register Environmental Protection Agency, Part VIII, 40 CFR Part 136, Washington DC, **1984**, 153.
31. EPA Method 8041, Phenols by Gas Chromatography: Capillary Column Technique, Environmental Protection Agency, Washington DC, **1995**, 1.
32. Bruno, F.; Pham, M.C.; Dubois, J.E.; *Electrochim. Acta.* **1977**, *22*, 451.
33. Saby, C.; Luong, J.H.T.; *Electroanalysis*, **1998**, *10*, 7.
34. Agui, L.; Serra, B.; Yanez-Sedeno, P.; Reviejo, A.J.; Pingarron, J.M.; *Electroanalysis*, **2001**, *13*, 1231.
35. Lu, W.; Wallace, G.G.; Imisides, M.D.; *Electroanalysis*, **2002**, *14*, 325

36. Saterlay, A. J.; Foord, J.S.; Compton, R.G.; *Electroanalysis*, **2001**, *13*, 1065.
37. Gattrell, M.; Kirk, D.W.; *J. Electrochem. Soc.* **1993**, *140*, 1534.
38. Belhadj Tahar, N.; Savall, A.; *J. Electrochem. Soc.* **1998**, *145*, 3427.
39. Rodgers, J.D.; Jedral, W.; Bunce, N.; *J. Environ. Sci. Technol.* **1999**, *33*, 1453.
40. Gattrell, M.; Kirk, D.W.; *J. Electrochem. Soc.* **1993**, *140*, 903.
41. Mengoli, G.; Daolio, S.; Musiani, M.M.; *J. Electrochem. Soc.* **1980**, *10*, 459.
42. Gattrell, M.; Kirk, D.W.; *Can. J. Chem. Eng.* **1990**, *68*, 997.
43. Xu, J.; Chen, Q.; Swain, G.M.; *Anal. Chem.* **1998**, *70*, 3146.
44. Muna, G.W.; Tasheva, N.; Swain, G.M.; *Environ. Sci. Technol.* **2004**, *38*, 3674.
45. Swain, G.M.; Anderson, A. B.; Angus, J.C.; *MRS Bull.* **1998**, *23*, 56.
46. Hupert, M.; Muck, A.; Wang, J.; Stotter, J.; Cvackova, Z.; Haymond, S.; Show, Y.; Swain, G.M.; *Diam. Rel. Mater.* **2003**, *12*, 1940.
47. Kinoshita, K.; *Carbon: Electrochemical and Physicochemical Properties*; John Wiley & Sons: New York, **1988**.
48. Arihara, K.; Kitamura, F.; Nukanobu, K.; Ohsaka, T.; Tokuda, K.; *J. Electroanal. Chem.* **1999**, *473*, 138.
49. Edstrom, K.; Herranen, M.; *J. Electrochem. Soc.*, **2000**, *147*, 3628.
50. Chen, P.; McCreery, R.L.; *Anal. Chem.* **1996**, *68*, 3958.
51. Duebgen, R.; *Can. Chem. News*, **1987**, *39*, 13.
52. Engelman, E. E.; Evans, D.H.; *Langmuir*, **1992**, *8*, 1637.
53. Kamau, G.N.; *Anal. Chim. Acta.* **1988**, *207*, 1.
54. Angus, J.C.; Argoitia, A.; Gat, R.; Li, Z.; Sunkara, M.; Wang, L.; Wang, Y.; *Philos. Trans. R. Soc. Lond. Ser. A-Math. Phys. Eng. Sci.* **1993**, *342*, 195.
55. Angus, J.C.; Collins, A.T.; *Nature*, **1994**, *370*, 601.



56. Angus, J.C. Martin, H.B.; Landau, U.; Evstefeeva, Y.E.; Miller, B.; Vinokur, N.; *New Diamond and Frontier Carbon Technology* **1999**, *9*, 175.
57. Chen, Q.; Granger, M.C.; Lister, T.E.; Swain, G.M.; *J. Electrochem. Soc.* **1997**, *144*, 3806.
58. Katsuki, N.; Wakita, S.; Nishiki, Y.; Shimamune, T.; Akiba, Y.; Iida, M.; *Jpn. J. Appl. Phys. Lett.* **1997**, *36*, L260.
59. Granger, M.C.; Witek, M.; Xu, J.; Wang, J.; Hupert, M.; Hanks, A.; Koppang, M.D.; Butler, J.E.; Lucazeau, G.; Mermoux, M.; Strojek, J.W.; Swain, G.M.; *Anal. Chem.* **2000**, *72*, 3793.
60. Anderson, A.; Kang, D.; *J. Phys. Chem.*; **1998**, *102*, 5993.
61. Vinokur, N.; Miller, B.; Avyigal, Y.; Kalish, R.; *J. Electrochem. Soc.* **1996**, *143*, L238.
62. Ramesham, R.; Rose, M.; *Thin Solid Films*, **1997**, *300*, 144.
63. Swain, G.M.; Ramesham, R.; *Anal. Chem.* **1993**, *65*, 345.
64. Xu, J.; Granger, M.; Chen, Q.; Strojek, J.; Lister, T.; Swain, G.M.; *Anal. Chem.* **1997**, *69*, 591A.
65. Terashima C.; Rao Tata, N.; Sarada, B.V.; Tryk, D.A.; Fujishima, A.; *Anal. Chem.* **2002**, *74*, 895.
66. Rao, T.N.; Loo, B.H.; Sarada, B.V.; Terashima, C.; Fujishima, A.; *Anal. Chem.* **2002**, *74*, 1578.
67. Fujishima, A.; Popa, E.; Wu, Z.; Rao, T.N.; *Novel trends in Electroorganic Synthesis, [Papers presented at the International Symposium on Electroorganic Synthesis], 3<sup>rd</sup>, Kurashiki, Japan, Sept. 24-27, 1998*, 421.
68. Ohta, N.; Nakabayashi, S.; Fujishima, A.; *Chem. Lett.* **1999**, 1147.
69. Rao, T.N.; Yagi, I.; Miwa, T.; Tryk, D.; Fujishima, A.; *Anal. Chem.* **1999**, *71*, 2605.
70. Rao, T.N.; Sarada, B.V.; Tyrk, D.; Fujishima, A.; *J. Electroanal. Chem.* **2000**, *491*, 175.
71. Sarada, B.V.; Rao, T.N.; Tyrk, D.; Fujishima, A.; *Proceedings Electrochemical Society* **2000**, 99-32, 502.

72. Chailapakul, O.; Aksharandana, P.; Frelink, T.; Einaga, Y.; Fujishima, A.; *Sens. Actuators B* **2001**, *B80*, 193.
73. Notsu, H.; Fukazawa, T.; Tatsuma, T.; Tyrk, D.A.; Fujishima, A.; *Electrochemical and Solid-State Letters* **2001**, *4*, H1.
74. Tsunozaki, K.; Einaga, Y.; Rao, T.N.; Fujishima, A.; *Chem. Lett.* **2002**, 502.
75. Pleskov, Y.V.; *J. Chem. Vap. Deposition*, **1997**, *5*, 126.
76. Pleskov, Y.V.; Mishuk, V.Y.; Abaturov, M.A.; Elkin, V.V.; Krotova, M.D.; Varnin, V.P.; Teremetskaya, I.G.; *Russ. J. Electrochem.* **1997**, *33*, 61.
77. Modestov, A.D.; Evstefeeva, Y.E.; Pleskov, Y.V.; Mazin, V.M.; Varnin, V.P.; Teremetskaya, I.G.; *J. Electroanal. Chem.* **1997**, *431*, 211.
78. Pleskov, Y.V.; Sakharova, A.Y.; Churikov, A.V.; Varnin, V.P.; Teremetskaya, I.G.; *Russ. J. Electrochem.* **1996**, *32*, 1075.
79. Angus, J.C.; Will, H.A.; Stanko, W.S.; *J. Appl. Phys.* **1968**, *39*, 2915.
80. Sunkara, M.; Angus, J.C.; Hayman, C.C.; Buck, F.A.; *Carbon* **1990**, *28*, 745.
81. Lambrecht, W.R.L.; Lee, C.H.; Segall, B.; Angus, J.C.; Li, Z.D.; Sunkara, M.; *Nature* **1993**, *364*, 607.
82. Mearini, G.T.; Krainsky, I.L.; Dayton, J.A.; Wang, Y.X.; Zorman, C.A.; Angus, J.C.; Hoffman, R.W.; *Appl. Phys. Lett.* **1994**, *65*, 2702.
83. Hyde, M.; Saterlay, A.J.; Wilkins, S.J.; Foord, J.S.; Compton, R.G.; Marken, F.; *J. Solid State Electrochem.* **2002**, *6*, 183.
84. Saterlay, A.J.; Foord, J.S.; Compton, R.G.; *Electroanalysis*, **2001**, *13*, 1065.
85. Saterlay, A.J.; Wilkins, S.J.; Holt, K.B.; Foord, J.S.; Compton, R.G.; Marken, F.; *J. Electrochem. Soc.* **2001**, *148*, E66.
86. Holt, K.B.; Delcampo, J.; Foord, J.S.; Compton, R.G.; Marken, F.; *J. Electroanal. Chem.* **2001**, *513*, 94.
87. Qui, F.; Compton, R.G.; Marken, F.; Wilkins, S.J.; Goeting, C.H.; Foord, S.J.; *Anal. Chem.* **2000**, *72*, 2362.

88. Goeting, C.H.; Marken, F.; Gutierrez-Sosa, A.; Compton, R.G.; Foord, S.J.; *New Diamond and Frontier Technology*, **1999**, *9*, 207.
89. Prado, C.; Flechsig, G.-U.; Gruendler, P.; Foord, S.J.; Marken, F.; Compton, R.G.; *Analyst*, **2002**, *127*, 329.
90. Gruen, D.M.; *MRS Bull.* **1998**, *23*, 32,
91. Krauss, A.R.; Gruen, D.M.; Auciello, O.H.; Carlisle, J.A.; Swain, G.M.; Ding, M. In *PCT Int. Appl.*; (The University of Chicago, USA) WO 2002 pp 48.
92. Chen, Q.; Gruen, D.M.; Krauss, A.R.; Corrigan, T.D.; Witek, M.; Swain, G.M.; *J. Electrochem. Soc.* **2001**, *148*, E44.
93. Fausett, B.; Granger, M.C.; Hupert, M.L; Wang, J.; Swain, G.M. Gruen, D.M.; *Electroanalysis*, **2000**, *12*, 7.
94. Zhou, D.; Gruen, D.M.; Qin, L.C.; McCauley, T.G.; Krauss, A.R.; *J. Appl. Phys.* **1998**, *84*, 1981.
95. Zhou, D.; McCauley, T.G.; Qin, L.C.; Krauss, A.R.; Gruen, D.M.; *J. Appl. Phys.* **1998**, *83*, 540.
96. Qin, L.C.; Zhou, D.; Krauss, A.R.; Gruen, D.M.; *Nanostructured Materials*, **1998**, *10*, 649.
97. Yoo, K.; Miller, B.; Kalish, R.; Shi, X.; *Proceedings-Electrochemical Society*, **2000**, *99-17*, 440.
98. Vinokur, N.; Miller, B.; Avyigal, Y.; Kalish, R.; *Electrochemical and Solid State letters*, **1998**, *1*, 265.
99. Vinokur, N.; Miller, B.; Avyigal, Y.; Kalish, R.; *J. Electrochem. Soc.*, **1999**, *146*, 125.
100. Vinokur, N.; Miller, B.; *Proc-Electrochem. Soc.* **1997**, *91-17*, 384.
101. Sopchak, D.; Miller, B.; Kalish, R.; Avyigal Y.; Shi, X.; *Electroanalysis*, **2002**, *14*, 473.
102. Muna, G.W.; Quaiserova-Mocko, V.; Swain, G.M.; *Electroanalysis*, **2005**, *17*, 1160.
103. Muna, G.W.; Quaiserova-Mocko, V.; Swain, G.M.; *Anal.Chem.* Submitted.

104. Stotter, J.M.; Haymond, S.; Butler, J.E.; Swain, G.M.; Zak, J.K.; *Abstracts of papers, 222<sup>nd</sup> ACS National Meeting, Chicago, IL, USA, August 26-30 2001*, ANYL-117.
105. Zak, J.K.; Butler, J.E.; Swain, G.M.; *Anal. Chem.* **2001**, *73*, 908.
106. Witek, M.; Wang, J.; Stotter, J.; Hupert, M.; Haymond, S.; Sonthalia, P.; Swain, G.M.; Zak, J.K.; Chen, Q.; Gruen, D.M.; Butler, J.E.; Kobashi, K.; Tachibana, T.; *Journal of Wide Bandgap Materials*, **2002**, *8*, 171.
107. Xu, J.; Swain, G.M.; *Anal. Chem.* **1998**, *70*, 1502.
108. Reuben, C.; Galun, E.; Tenne, R.; Kalish, R.; Muraki, Y.; Hashimoto, K.; Fujishima, A.; Butler, J.M.; Levy-Clement, C.; *NATO ASI Ser.* **1995**, *1*, 137.
109. Granger, M.C.; Xu, J.; Strojek, J.W.; Swain, G.M.; *Anal. Chim. Acta.* **1999**, **397**, 145.
110. Gherardini, L.; Comninellis, C.; Vatistas, N.; *Annali di Chim.* **2001 Mar-Apr**, *91*, 161.
111. Terashima, C.; Rao, T.N.; Sarada, B.V.; Fujishima, A.; *Chemical Sensors*, **2001**, *17*, 124.
112. Terashima, C.; Rao, T.N.; Sarada, B.V.; Tryk, D.A.; Fujishima, A.; *Anal. Chem.* **2002**, *74*, 895.
113. Fujishima, A. Terashima, C.; Honda, K.; Sarada, B.V.; Rao, T.N.; *New Diamond and Frontier Carbon Technology*, **2002**, *12*, 73.
114. Spataru, N.; Rao, Sarada, B.V.; Popa, E.; Tryk, D.A.; Fujishima, A.; *Anal. Chem.* **2001**, *73*, 514.
115. Martin, H.B.; Morrison, P.W.; Jr.; *Electrochemical and Solid-State letters*, **2001**, *4*, E17.
116. Argoitia, A.; Martin, H.B.; Rozak, E.J.; Landau, U.; Angus, J.C.; *Mater. Res. Soc. Symp. Proc.* **1996**, *416*, 349.
117. Witek, M.A.; Swain, G.M.; *Anal. Chim. Acta.* **2001**, *440*, 119
118. Show, Y.; Witek, W.A.; Sonthalia, P.; Swain, G.M.; *Chem. Mater.* **2003**, *15*, 879.

119. Sonthalia, P.; McGaw, E.; Show, Y.; Swain, G.M.; *Anal. Chim. Acta.* **2004**, 522, 35.
120. May, P.W.; *Philosophical Transactions of the Royal society of London, Series A: Mathematical, Physical and Engineering Sciences*, **2000**, 358, 473.
121. Angus, J.C.; *MRS Bull.* **1998**, 21, 4
122. Angus, J.C.; Li, Z.; Sunkara, M.; Gat, R.; Anderson, A.B.; Mehandru, S.P.; Geis, M.W.; *Proc-Electrochem. Soc.* **1991**, 91-8, 125.
123. Bachmann, P.K.; *EMIS Datareviews Series*, **1994**, 9, 354.
124. Bachmann, P.K.; *EMIS Datareviews Series*, **1994**, 9, 349.
125. Bachmann, P.K.; *EMIS Datareviews Series*, **1994**, 9, 364
126. Gruen, D. M.; *MRS Bull.* **1998**, 23, 32.
127. Gruen, D. M.; *Annu. Rev. Mater. Sci.* **1999**, 29, 211.
128. Gruen, D.M.; *Annual Review of Materials Science*, **1999**, 29, 211.
129. Spitsyn, B.V.; Aleksenko, A.E.; Sokorina, G.A.; Laptev, V.A.; *New Diamond Sci. Technol.; Proc. Int. Conf., 2<sup>nd</sup>* **1991**, 909.
130. Looi, H.J.; Pang, L.Y.S.; Molly, A.B.; Jones, F.; Foord, J.S.; Jackman, R.B.; *Diam. Rel. Mater.* **1998**, 7, 550.
131. R. F. Mamin, T. Inushima, *Phys. Rev. B* **2001**, 63, 033201.
132. Popa, E.; Notsu, H.; Miwa, T.; Tryk, D.A.; Fujishima, A.; *Electrochem. Solid-State Lett.* **1999**, 49.
133. Spear, K.E.; *Synthetic Diamond Emerging CVD Science and Technology*. John Wiley & Sons, Inc. New York, **1994**.
134. Granger, M.C.; Swain, G.M.; *J. Electrochem. Soc.* **1999**, 146, 4551

## **CHAPTER 2**

# **Experimental Procedures and Instrumentation**

## **2.1. Diamond Thin-Film Deposition**

Boron-doped diamond thin films were deposited using a commercial chemical vapor deposition (CVD) system (1.5 kW ASTEX Corp., Lowell, MA). Microwave energy originating from a magnetron was directed into a quartz reaction chamber to generate a plasma above the sample stage. Deposition occurred on the surface of the substrate, which was placed on a molybdenum stage positioned in the middle of the reaction chamber. The substrate was in contact with the lower region of the plasma discharge. Figure 2.1 shows a schematic of the CVD reactor. Details of the deposition and substrate preparation are presented in the following paragraphs.

### **2.1.1. Planar Film Electrodes**

#### **2.1.1.1. Microcrystalline Diamond Thin-Film Electrodes**

Microcrystalline diamond thin film was deposited on p-Si (100) (Virginia Semiconductor Inc., Fredricksburg, VA) substrate. The substrate (ca. 1 x 1 cm<sup>2</sup>) was prepared for deposition by, first, rinsing with ultrapure water, methanol, and

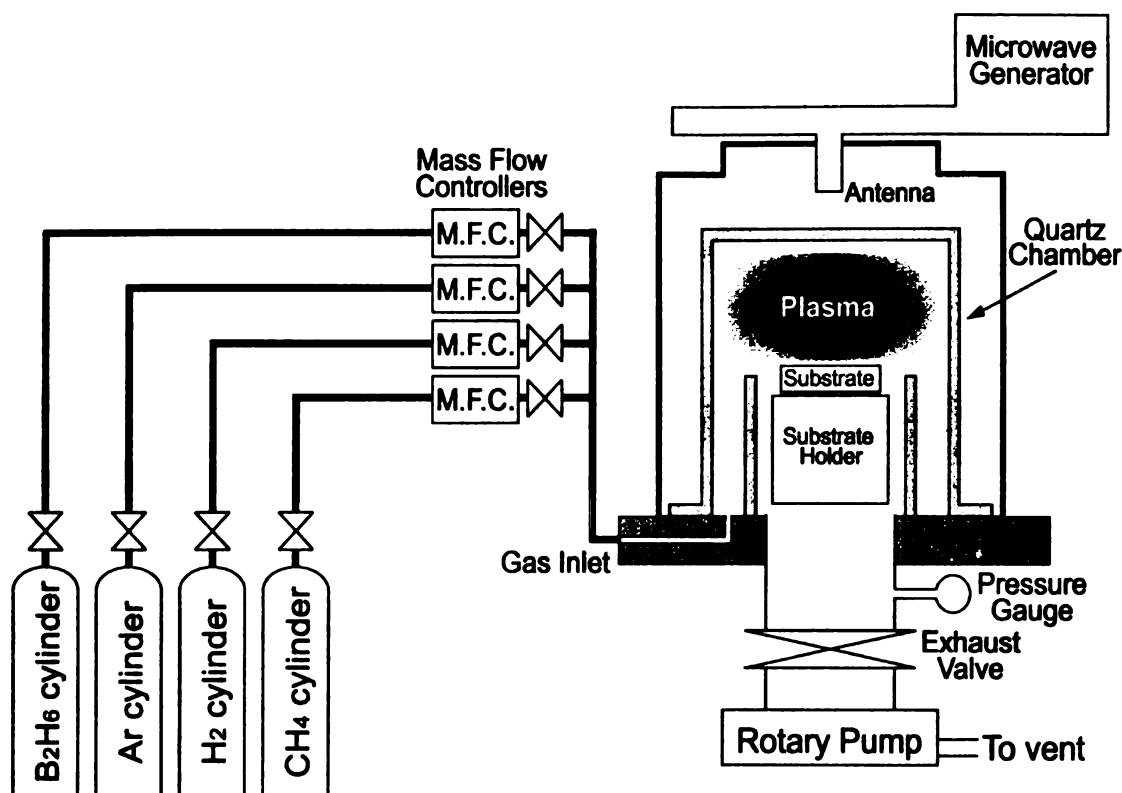


**Figure 2.1** Microwave-assisted CVD apparatus for diamond growth.

acetone. It was then polished with 0.1  $\mu\text{m}$  diameter diamond powder (GE Superabrasives, Worthington, OH) for 5 min on a felt pad. The scratched substrate was then ultrasonically cleaned in acetone for several minutes until the polishing debris was removed. The clean scratches, as well as residual diamond particles, serve as the initial nucleation sites for film growth.

The microcrystalline film was deposited from a 0.5% CH<sub>4</sub>/H<sub>2</sub> (C/H) source gas mixture at a total gas flow of 200 sccm, 1 kW of microwave power, a system

pressure of 45 torr, an estimated substrate temperature of 800°C, and a growth time ca. 10 h. Ultrahigh purity (99.999%) CH<sub>4</sub> and H<sub>2</sub> were used as the source gases for the growth. Boron doping was accomplished using either a solid state boron diffusion source (BoronPlus GS 126, Techneglas, Inc. Perrysburg, OH) or by adding B<sub>2</sub>H<sub>6</sub> diluted in H<sub>2</sub> to the source gas mixture. The diffusion source was placed underneath the substrate with B<sub>2</sub>O<sub>3</sub> diffusing from the disc and serving as the source for the dopant atoms. In the case of gas phase doping, B<sub>2</sub>H<sub>6</sub> concentration of 10 ppm was used. After deposition, the CH<sub>4</sub> flow was stopped and the film remained exposed to the H<sub>2</sub> plasma for an additional 15 min at the growth conditions. After this annealing period, the plasma power and system pressure were gradually reduced over a 15 - 30 min period, to 400 W and 20 torr, repeatedly in order to cool the samples (<400 °C) in the presence of atomic hydrogen. Post growth annealing in atomic hydrogen is critical for etching adventitious non-diamond phases, minimizing dangling bonds, and ensuring full hydrogen termination. The plasma was then extinguished and the films further cooled to room temperature under a flow of hydrogen. Table 2.1 lists the typical deposition conditions for microcrystalline diamond thin film growth. The film thickness was nominally 5 μm and the boron dopant concentration was in the low to mid 10<sup>20</sup> cm<sup>-3</sup> range. The doping level was determined from boron nuclear reaction analysis measurements made at the surface characterization facility at Case Western Reserve University. The film resistivity was ~0.01 Ω-cm, or less, as measured with a tungsten four-point probe. Therefore, the electrical



conductivity of the diamond is comparable to that along the C-axis of the HOPG (between the large planes).

**Table 2.1 Microcrystalline Diamond Thin-Film Deposition Parameters**

<b>Deposition Parameters</b>	
Substrate	Si
CH <sub>4</sub> /H <sub>2</sub> (v/v) ratio	0.5 %
Plasma forward power	1 kW
Deposition pressure	45 torr
Deposition time	10 h
Substrate temperature	800 °C
Boron dopant source	B <sub>2</sub> O <sub>3</sub> or B <sub>2</sub> H <sub>6</sub>
Doping level	~1x10 <sup>20</sup> B/cm <sup>3</sup>
Resistivity	~ 0.01 Ω-cm or less

### **2.1.1.2. Nanocrystalline Diamond Thin-Film Electrodes**

The boron-doped nanocrystalline diamond thin film was deposited on a p-Si (100) substrate (~ 10<sup>-3</sup> Ω-cm, Virginia Semiconductor Inc., Fredricksburg, VA). The substrate was prepared for diamond growth by, first, mechanically scratching the surface on a felt polishing pad for 5 min with 0.1 μm diameter diamond powder (GE Superabrasives, Worthington, OH). The scratched substrate was then washed with ultrapure water, isopropyl alcohol (IPA), acetone, IPA, and ultrapure water before being ultrasonically cleaned in acetone to remove the

polishing debris. Ultrahigh purity, CH<sub>4</sub>, Ar, and H<sub>2</sub> (99.999%) were used as the source gases.

The film was grown using flow rates of 1, 94, and 5 sccm, respectively, for CH<sub>4</sub>, Ar, and H<sub>2</sub>. The microwave power and system pressure were maintained at 800 W and 140 Torr, respectively. Table 2.2 lists the typical deposition conditions. B<sub>2</sub>H<sub>6</sub> was used for doping and was added to the gas source mixture at a concentration of 10 ppm. The substrate temperature was estimated, by optical pyrometry, to be about 800°C. The deposition time was 2 h giving approximately a 4 μm-thick film, as estimated from sample weight change.

All gases flowed into the reactor simultaneously to initiate the diamond deposition. At the end of the deposition period, the CH<sub>4</sub> flow was stopped and the Ar and H<sub>2</sub> flows continued. The film remained exposed to an H<sub>2</sub>/Ar plasma for approximately 10 min. The substrate was then cooled in presence of atomic hydrogen to an estimated temperature of less than 400°C by slowly reducing the plasma power and pressure over a period of 4 min. This leads to the formation of a thin and continuous nanocrystalline diamond thin film in a relatively short period of time.

**Table 2.2 Nanocrystalline Diamond Thin-Film Deposition Parameters**

<b>Deposition Parameters</b>	
Substrate	p-Si (100)
CH <sub>4</sub> /Ar/H <sub>2</sub> (v/v) ratio	1/94/5
Plasma forward power	0.8 kW
Deposition pressure	140 torr
Deposition time	2 h
Substrate temperature	800 °C
Boron dopant source	B <sub>2</sub> H <sub>6</sub>
Doping level	10 ppm
Resistivity	~ 0.01 Ω-cm or less

### **2.1.2. Boron-Doped Diamond Thin-Film Microelectrodes**

Boron-doped diamond thin film was deposited on sharpened, 76 μm diameter, Pt wires (St. Louis, MO, 99.99% pure).<sup>1</sup> Prior to deposition, the sharpened wire was prepared by, first, ultrasonic cleaning in acetone for 10 min. The wire was then ultrasonically “seeded” for 30 min in a diamond powder suspension (5 nm particles, ca. 20 mg in 100 mL of ethanol, Tomai Diamond Co., Tokyo, Japan). During the seeding process, the metal surface is scratched by the diamond particles with some getting embedded. Both the scratches and the embedded particles likely serve as the initial nucleation sites for film growth.

The pretreated Pt wire was mounted horizontally in the reactor on top of a quartz plate (10 x 10 x 1 mm). Four or five wires were coated during a deposition run. The quartz plate was placed in the center of the molybdenum substrate stage and served to thermally isolate the wires. Boron-doped diamond thin film was deposited from a 0.5 % CH<sub>4</sub>/H<sub>2</sub> source gas mixture with doping accomplished by adding 10 ppm of diborane, B<sub>2</sub>H<sub>6</sub>, diluted in H<sub>2</sub>. All source gases were ultrahigh purity (99.999 %). For growth, the system pressure was 45 torr, the substrate temperature ~ 600 °C (as estimated with an optical pyrometer), the microwave power was 400 W, and the total gas flow was 200 sccm. The deposition time was 10 h. The nominal growth rate under these conditions was estimated to be about 0.3 – 0.5 μm/h, leading to a final film thickness of 3-5 μm.

The Pt wire was sharpened electrochemically using 1 M KOH prepared with ultrapure water (Barnstead E-Pure system). The etching apparatus consisted of a small Teflon vessel equipped with four equidistantly-spaced carbon rod auxiliary electrodes electrically connected to one another. A 1.3-cm long piece of 76 μm diameter Pt wire was attached to a holder fabricated using a small metal clip soldered to a copper wire, immersed into the etching solution to a depth of 1 to 2 mm in the center of the four carbon rod electrodes. An AC polarization of 12 V (60 Hz) was applied using a variable autotransformer (Staco Energy Products, Dayton, OH,). The sharpening procedure was considered complete after approximately 25 s; a point at which visible gas evolution ceased.

After deposition, the diamond-coated Pt wire was attached to a copper wire (~7 cm in length, 0.2 mm in diameter, Goodfellow Cambridge Ltd., Huntingdon, England) using conductive silver epoxy (CW2400 Chemtronics, Kennesaw, GA), which was allowed to cure overnight at room temperature. The microelectrode was then sealed in a polypropylene pipet tip (Ultramicro pipet tip, Daigger, Vernon Hills, IL). After inserting the diamond-coated Pt wire into a tip, a heat gun was used to first melt the polypropylene at the top of the microelectrode assembly (securing the copper wire). The tip end was then carefully heated, which softened the polypropylene and formed a conformal coating around the rough microelectrode. The resulting microelectrode had both a conical and cylindrical geometry, as shown in Figure 2.2.

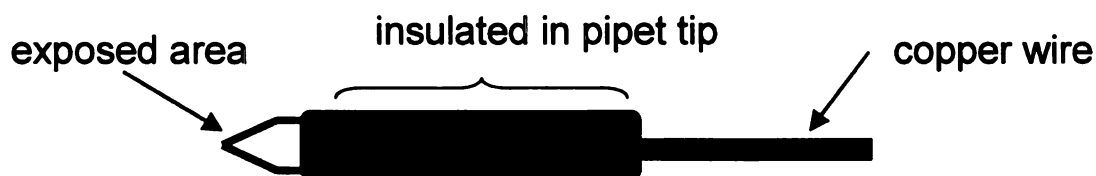


**Figure 2.2** Schematic of a boron-doped diamond microelectrode sealed in a polypropylene pipet tip.

## 2.2. Glassy Carbon Electrode Preparation

The glassy carbon (GC-30, Tokai, Japan) was polished with successively smaller sizes of alumina powder (Buehler, Lake Bluff, IL) slurried in ultrapure water (~18 M $\Omega$ -cm, Barnstead E-Pure) on a felt polishing cloth (Buehler). Grit sizes of 1.0, 0.3 and 0.05  $\mu$ m were used. The electrode was sonicated in

ultrapure water for 10 min after each polishing step to remove polishing debris. At the end of the polishing sequence, the electrode was thoroughly rinsed with water and allowed to soak in distilled IPA for 10 - 20 min prior to use. An electrode was used in electrochemical measurements immediately after completion of polishing steps.

## **2.3. Characterization of the Diamond Thin-Film Electrodes**

### **2.3.1. Scanning Electron Microscopy (SEM)**

SEM was performed with JOEL-6400 V electron microscope. Images were collected at a 2048 X 1536 pixel resolution with an ADDA II digital image acquisition system and AnalySIS Pro 3.2 image acquisition software (Soft Imaging system GmbH, Munster, Germany).

### **2.3.2. Atomic Force Microscopy (AFM)**

AFM was performed with a NanoScope III instrument (Veeco Metrology Group, Inc., Santa Barbara, CA) operated in the contact mode. Pyramidal  $\text{Si}_3\text{N}_4$  probe tips, mounted on Au-coated cantilevers (100  $\mu\text{m}$  legs, 0.38 N/m spring constant), were used in air to acquire topographical images of the films.

### **2.3.3. Raman Spectroscopy**

Raman spectra were obtained at room temperature. The instrument consisted of a diode-pumped, frequency-doubled CW Nd: yttrium aluminum garnet (YAG) excitation laser of 523 nm and objective lens of x 20 (Raman 2000,

Chromex, Inc., Albuquerque, NM). Spectra were collected with an incident power density of  $\sim 500 \text{ kW/cm}^2$  (100 mW at the sample and  $5 \text{ }\mu\text{m}$  diameter spot size), a 10 s integration time and spectra resolution of about  $2 \text{ cm}^{-1}$ . A white light spectrum collected under the same conditions was used for background correction.

#### **2.3.4. X-ray Diffraction (XRD)**

XRD analysis was using a Rigaku Rotaflex diffractometer equipped with a rotating anode and a Cu K-alpha radiation source. In the measurements, the thin film rotates by an angle,  $\theta$ , with respect to a fixed-positioned x-ray source, and the detector rotates by  $2\theta$  to measure the diffracted radiation. Diffraction profiles were collected using incident angles of  $30^\circ$  to  $100^\circ$  with respect to the sample surface.

#### **2.3.5. Electrical Resistivity**

Electrical resistance measurements were made using a tungsten four-point probe having a 1 mm probe spacing. Currents ( $\mu\text{A}$ ) were applied between the outer two electrodes and the resulting voltage drop between the inner electrodes was measured. Five measurements were taken from different regions on each film.

### **2.3.6. Contact Angle Measurements**

An automated contact angle apparatus (First Ten Angstroms) was used to deliver a 10  $\mu\text{L}$  drop of deionized water from a 50-mL syringe onto the diamond surface. The drop was formed at the end of the blunt, stainless steel syringe needle and the diamond film was then raised slowly to touch the drop. Images of the static drop on the film surface were captured with a video camera. The contact angle was obtained using image analysis software. The angle between a tangent line and the electrode surface was measured at the left and right sides of the drop. The right and left angles were averaged to give one contact angle value. Five measurements were made on a single film with the electrode rinsed with acetone and dried under  $\text{N}_2$  between measurements. Four microcrystalline diamond thin-film electrodes were tested and gave contact angles ranging  $69.2 \pm 5.5^\circ$ ,  $64.0 \pm 3.0^\circ$ ,  $72.8 \pm 2.3^\circ$ , and  $75.3 \pm 5.1^\circ$ .

### **2.4. Electrochemical Measurements**

Cyclic voltammetric measurements were made with a CYSY- 2000 computerized potentiostat (Cypress System Inc. Lawrence, KS) using a single compartment glass cell. A diagram of the cell is shown in Figure 2.3. The diamond film or glassy carbon electrode was pressed against a viton o-ring and clamped to the bottom of the glass cell. Ohmic contact was made by pressing a copper plate against the backside of the scratched and cleaned Si substrate, which contained a bead of Ga/In alloy or silver paste. A graphite rod was used as the counter electrode and a commercial Ag/AgCl electrode (4 M KCl) served as



the reference. The geometric area of the working electrode was ca. 0.2 cm<sup>2</sup>. All measurements were made at room temperature. All solutions were deoxygenated with nitrogen for 5 min prior to any measurement and remained blanketed with the gas during a measurement.

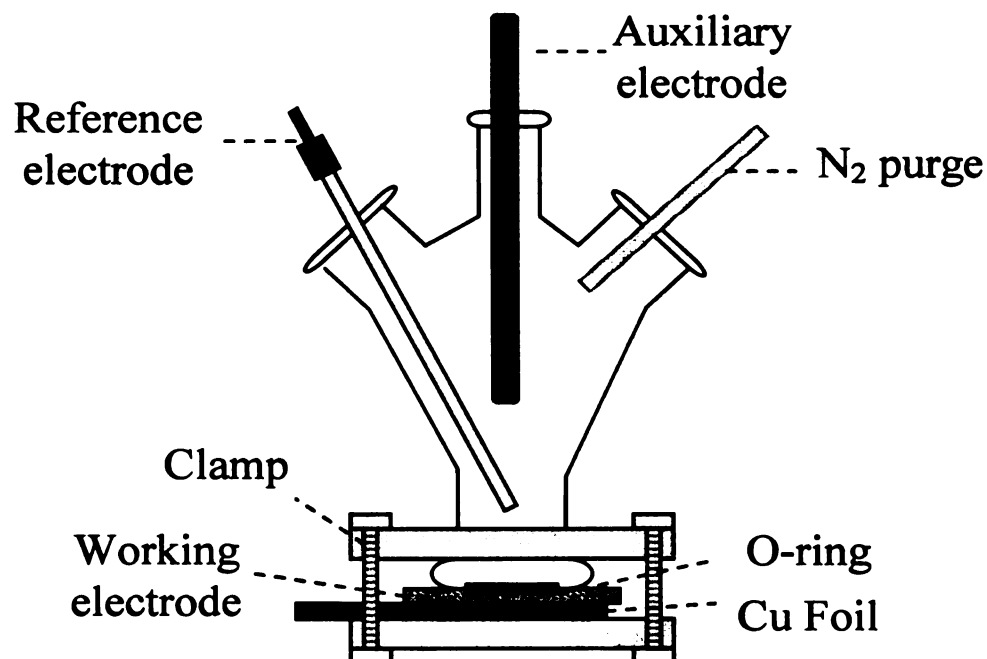


**Figure 2.3** Design of the three-electrode, single compartment electrochemical cell.

Electrochemical measurements using the diamond microelectrode were performed in a 10 mL glass vial with a cover that had openings for the auxiliary, reference, and working electrodes. A three-electrode system consisting of a diamond microelectrode, a Ag/AgCl reference electrode, and a carbon rod auxiliary electrode was connected to the potentiostat. The cell was housed in an

electrically-grounded Faraday cage to reduce the ambient electrical noise. All measurements were performed at room temperature in solutions deoxygenated with nitrogen for 5 min.

## 2.5. Flow Injection Analysis

Flow injection analysis (FIA) studies were performed using a home-made thin-layer electrochemical flow cell with a cross-flow geometry. The experimental set-up has been described elsewhere.<sup>2</sup> A block diagram of the FIA system and a schematic of the thin-layer flow cell are shown in Figures 2.4 and 2.5.

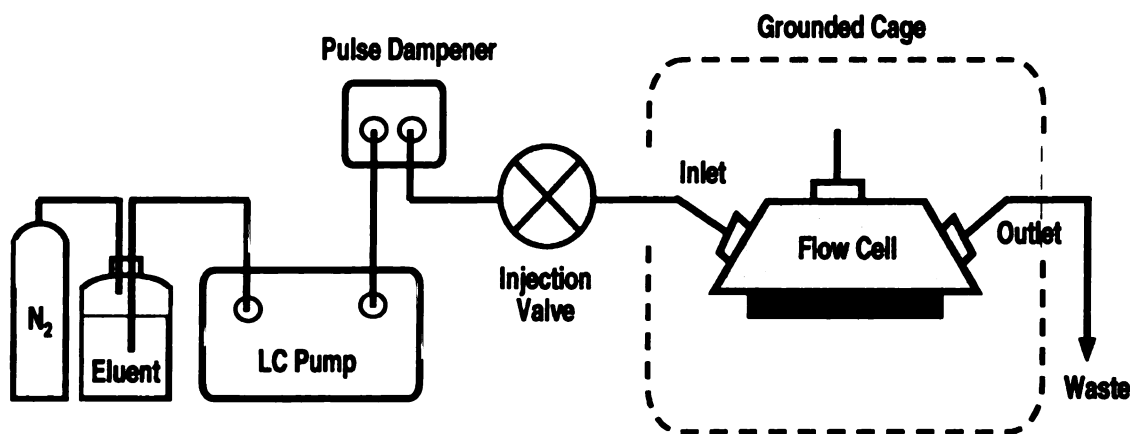


**Figure 2.4** A schematic of the FIA system.

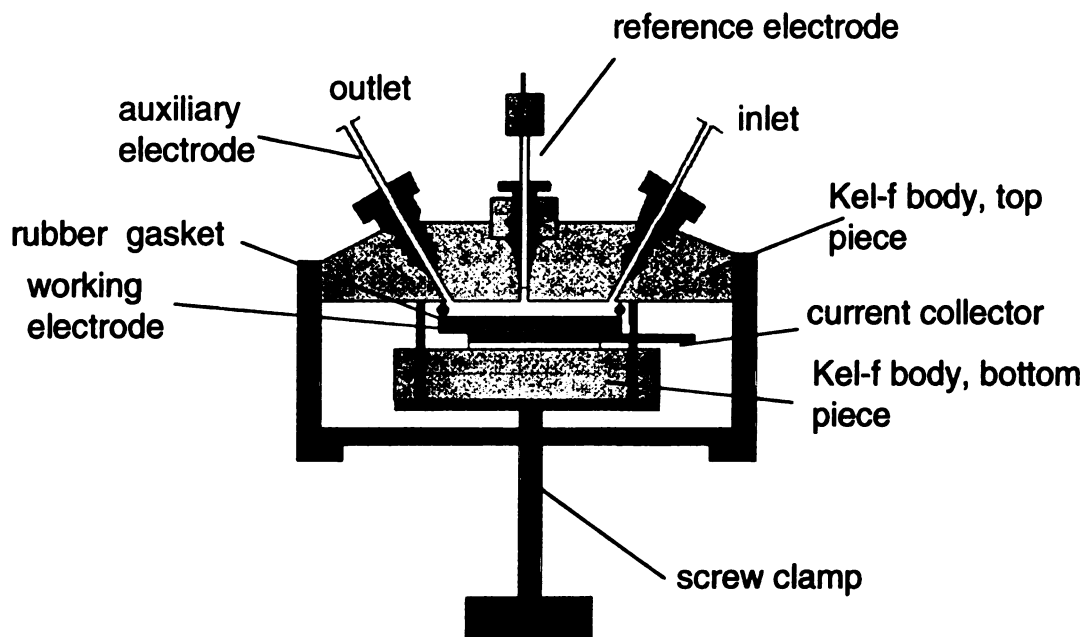


**Figure 2.5** Design of the thin-layer flow cell.

The flow rate of the carrier solution was regulated with a consta-Metric III metering pump (Milton Roy) through a model 7125 injector valve (Rheodyne) with a 20- $\mu$ L injection loop and into the flow cell. The carrier solution, flowing at 0.6 mL/min, was constantly sparged with nitrogen. Pump noise was reduced with a Model LP-21 pulse dampener (Scientific Systems) placed between the pump outlet and the injector valve. Amperometric detection was used and the current was recorded in analog form using a strip chart recorder. The entire set-up was grounded and the flow cell was housed in a Faraday cage to reduce the pick-up of electrical noise. The flow cell was constructed with two pieces of Kel-

F<sup>TM</sup>. The top piece contained the inlet and outlet for the fluid flow and a place for the reference electrode. The outlet port was fitted with a short piece of stainless steel tubing that served as the counter electrode. The bottom piece supported the working electrode. Electrical contact was made by pressing a piece of copper foil against the back side of the planar working electrode. A rubber (neoprene) gasket separated the surface of the working electrode from the top piece of the cell. A rectangular groove (7 mm x 1.5 mm x 1 mm) was cut into the gasket and this defined the flow channel. Assuming a 25% compression of the gasket when the top and bottom pieces of the cell were clamped together, the cell volume was estimated to be ~8  $\mu$ L. An Omni-90 analog potentiostat (Cypress Systems, Inc. Lawrence, KS) was employed to control the potential applied to the working electrode and to measure the current flowing during detection. The potential was applied with respect to a commercial Ag/AgCl mini-electrode (3 M NaCl, Cypress Systems, Inc. Lawrence, KS).

## **2.6. High Performance Liquid Chromatography**

Reversed-phase high performance liquid chromatography (HPLC) was performed using a commercial system (LC-10A, Shimadzu Corp., Columbia, MD), which consisted of a controller (SCL-10AVP), a solvent delivery module (LC-10ADVP), a degasser (DGU-14A), and an auto-injector (SIL-10ADVP). The same thin-layer flow cell described above was used for electrochemical detection. Elution was carried out by changing the 50 mM phosphate buffer (pH 3.5)/acetonitrile mobile phase composition from 65:35 to 20:80 (v/v). The flow

rate was maintained at 0.6 ml/min. The mobile phase was constantly sparged with nitrogen (99%). The separation of phenol and the chlorophenols was carried out using a C<sub>18</sub> reversed-phase column (X-Terra, 5 μm particle size, 3.9 x 150 mm, Waters). The stationary phase was 3-(chlorodimethylsilyl)propyl-N-dodecyl carbamate. This column has a modified silica support in which some of the silicon atoms are replaced with carbon. This substitution reduces the support's solubility at high pH, yet leaves sufficient silanol activity to enable the use of traditional bonding chemistry to covalently attach the stationary phase. An Omni-90 analog potentiostat (Cypress Systems, Inc. Lawrence, KS) controlled the potential applied to the working electrode and measured the current flowing during detection. Data acquisition and processing were performed with Class VP 7.0 chromatography software package (Shimadzu).

## **2.7. Capillary Electrophoresis**

Capillary electrophoresis was performed using a home-made system consisting of CZE1000R 30 kV variable power supply (Spellman, Hauppauge, NY), a home made electronic timer for the electrokinetic injection, and a plexiglas box with a safety interlock that housed the 76-cm long, 30 μm i.d. fused-silica capillary (Polymicro Technologies, Phoenix, AZ), buffer reservoir, sample vessel, and detection cell. Figure 2.6 show a block diagram of the system.

The separations were made by applying the desired positive voltage between the run buffer reservoir and the electrically-grounded detection reservoir. Electrokinetic injection was used to introduce the sample onto the

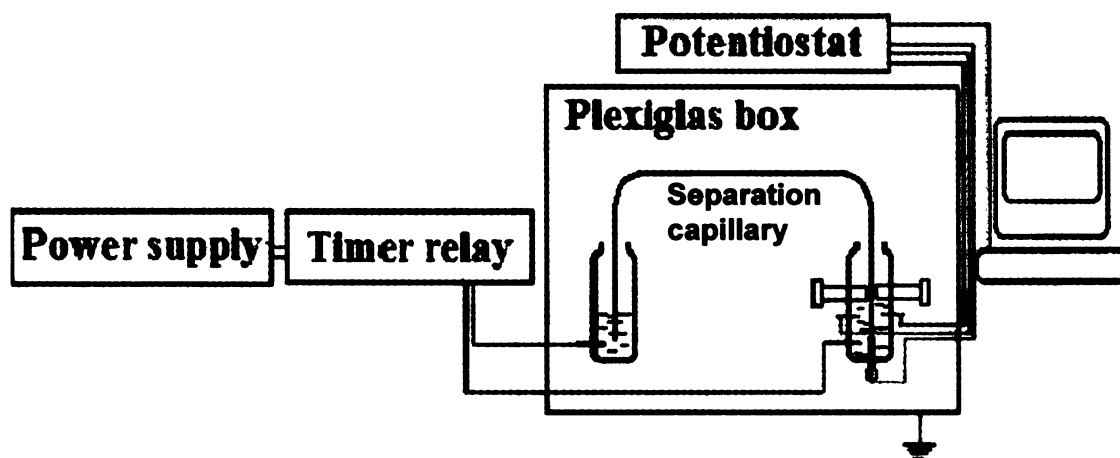


**Figure 2.6** Capillary electrophoresis set up.

column by applying 8 - 10 kV for 3s between the sample reservoir and the electrically-grounded detection reservoir. The plexiglas box was covered with aluminum foil and was electrically grounded in order to reduce the pick up of electrical noise.

The end-column detection cell was fabricated from glass and consisted of (i) four Teflon rods with Kel-F bolts for adjusting the capillary position in the  $x$  and  $y$  directions, (ii) two Pt wires with one serving as a ground for the high voltage and the other as an auxiliary electrode for the electrochemical cell, (iii) a bolt for

adjusting the separation capillary-electrode distance in the z direction, and (iv) two openings for mounting the working and the reference electrodes.<sup>1</sup> A three-electrode system was employed. Figure 2.7 shows a diagram of the detection cell.

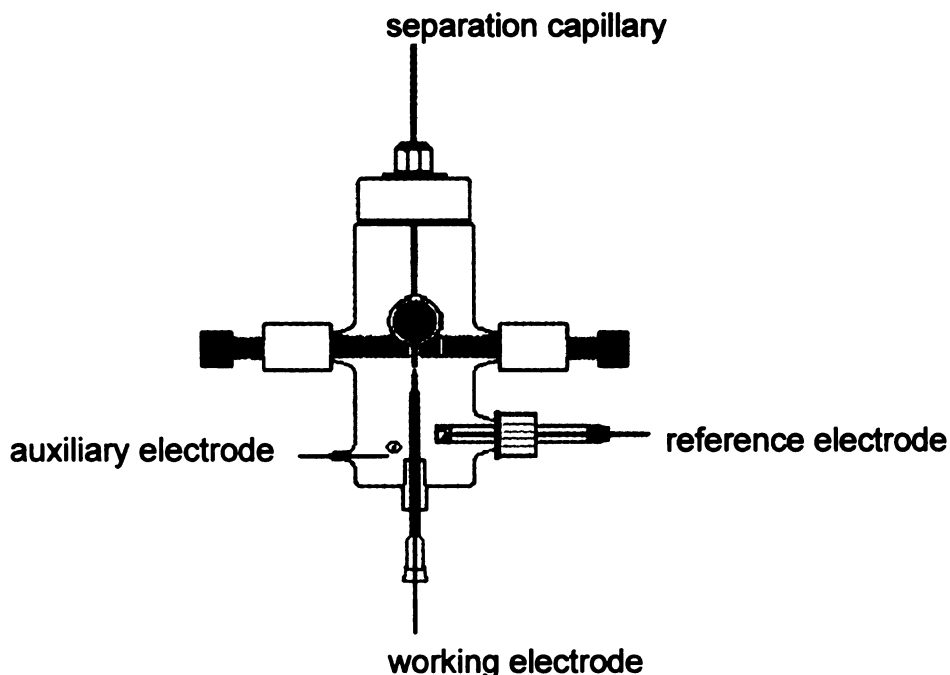


**Figure 2.7** Design of the end-column electrochemical detection cell.<sup>1</sup>

All the electrodes were connected to a digital potentiostat (EI-400 Bipotentiostat, Cypress Systems, Inc., Lawrence, KS) and the data were acquired digitally using Powerlab Chart 5 (ADInstruments, Colorado Springs, CO). Each new capillary was activated by sequentially flowing (pressure driven) a solution of 0.5 M NaOH, deionized water, and the run buffer for 20 min each. The capillary was then equilibrated in the run buffer under an electric field of 263 V/cm (20 kV) for approximately 20 min prior to sample injection.

## **2.7. Solid Phase Extraction**

Local river water (Red Cedar River, MSU Campus) was used as the sample from which to extract the chlorinated phenols. The river water was collected in a 500 mL Nalgene bottle. The bottle was flushed three times with the water before collecting a sample. The sample was stored in a capped bottle and transported back to the laboratory. The river water was first filtered through a nylon membrane with a 0.4  $\mu\text{m}$  pore size (Sigma-Aldrich, St. Louis, MO). After filtration, the pH of the water was adjusted to 2.5 using concentrated HCl and then spiked with chlorinated phenols. An Alltech Vacuum manifold was used for the SPE procedure. It consisted of a glass chamber, a vacuum Gauge and valve, manifold lid and stop cocks. The ENVI-Chrom P SPE tubes (80 – 160  $\mu\text{m}$  particle size, 800 – 950  $\text{m}^2/\text{g}$  surface area, 110 – 175  $\text{\AA}$  mean pore size, 3 mL tube volume and 0.25 g sorbent loading) were used for the extraction (Supelco, Bellefonte, PA). Prior to extraction, the sorbent were conditioned sequentially by passing 3 mL of ethyl acetate, 3 mL of methanol and 3 mL of ultrapure water adjusted to pH 2.5 using concentrated HCl. Solutions were passed through the sorbent by applying a vacuum (vacuum assisted). The filtered river water sample was passed through the moist sorbent at a low flow rate of < 5 mL/min. After sample passage, the solid phase was dried under vacuum for 5 min prior to analyte elution. Elution was performed by adding 2 mL of ethyl acetate and allowing it to interact with the solid phase for 5 min before elution. The elution was then performed at a flow rate of about 2 mL/min. The extract had two phases, aqueous and non-aqueous, which were separated out. Chlorinated



phenols were found in the non-aqueous phase and none in the other phase. The volume of the non-aqueous phase was adjusted to 1 mL using ethyl acetate. If the elution volume was greater than 1 mL, the volume was reduced to less than 1 mL by passing a stream of N<sub>2</sub>, and then readjusted to 1 mL using ethyl acetate. Figure 2.8 summarizes the steps involved in the extraction.

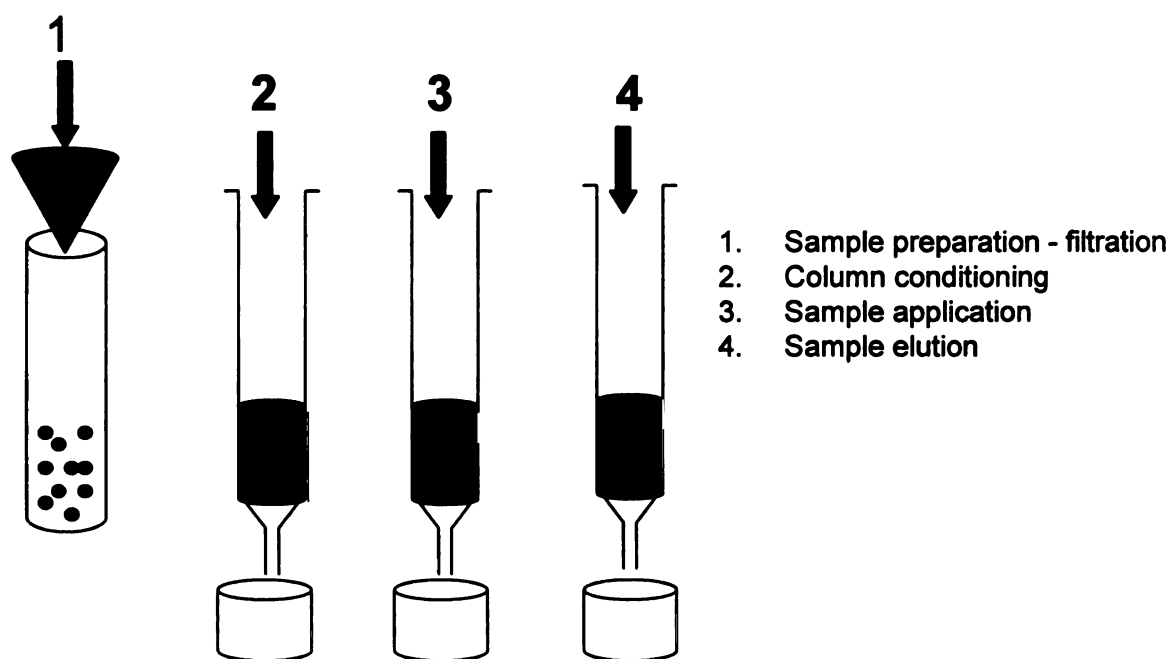


**Figure 2.8** SPE extraction steps.

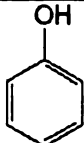
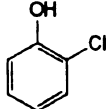
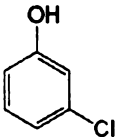
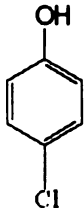
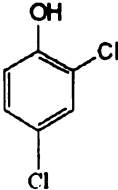
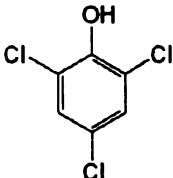
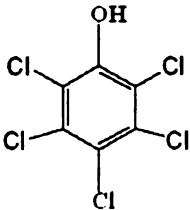
## **2.8. Materials and Chemicals**

Reagent-grade quality chemicals, or better; and ultrapure distilled and deionized water (~18 M $\Omega$ -cm, Barnstead E-Pure) were used to prepare all solutions. Potassium phosphate monobasic (Mallinckrodt, Germany) and acetonitrile (EM Science, Germany) were used to prepare the mobile phase for the HPLC measurements. Sodium phosphate monobasic, sodium tetraborate

( $\text{Na}_2\text{B}_4\text{O}_7 \cdot 10\text{H}_2\text{O}$ ), sodium phosphate dibasic, and sodium hydroxide (Spectrum Chemical, Gardena, CA) were used to prepare run buffer for capillary electrophoresis measurements. The run buffer was filtered through a nylon membrane with a 0.4  $\mu\text{m}$  pore size (Sigma-Aldrich, St. Louis, MO) before use. Ethyl acetate (Mallinckrodt, Germany) and methanol (Sigma-Aldrich, St. Louis, MO) were used in the SPE procedure.

The analytes of interest, phenol, 2-chlorophenol, 3-chlorophenol, 4-chlorophenol, 2,4-dichlorophenol, 2,4,6-trichlorophenol, and pentachlorophenol (Sigma-Aldrich, St. Louis, MO) were used without any additional purification. Table 2.3 shows the molecular structure, the  $\text{pK}_a$  and the formula weight for each analyte. The diamond film electrochemical response was characterized by cyclic voltammetry using the following inorganic and organic redox systems: potassium ferrocyanide ( $\text{Fe}(\text{CN})_6^{-3/-4}$ ), hexamine ruthenium (III) chloride ( $\text{Ru}(\text{NH}_3)^{+3/+2}$ ), iridium (IV) hexachloride ( $\text{IrCl}_6^{-2/-3}$ ), methyl viologen dichloride hydrate ( $\text{MV}^{+2/+1/0}$ ), 4-*tert*-butylcatechol, and ferric sulfate ( $\text{Fe}^{+2/+3}$ ) and ferrocene carboxylic acid (Sigma-Aldrich, St. Louis, MO). All of these chemicals were reagent-grade quality, or better, and used without additional purification. The supporting electrolyte for  $\text{Fe}(\text{CN})_6^{-3/-4}$ ,  $\text{Ru}(\text{NH}_3)^{+2/+3}$ ,  $\text{IrCl}_6^{-2/-3}$ ,  $\text{MV}^{+2/+1/0}$  was 1 M KCl. The supporting electrolyte for 4-*tert*-butylcatechol and  $\text{Fe}^{+2/+3}$  was 0.1 M  $\text{HClO}_4$ . The potassium chloride (Fisher) and perchloric acid (Sigma-Aldrich, St. Louis, MO) were ultrahigh purity (99.999%).

**Table 2.3 Properties of Phenol and the Chlorinated Phenols**

Compound	Molecular structure	pK <sub>a</sub> values	Formula Mass (g/mol)
Phenol		10.00	94
2-chlorophenol		8.52	128
3-chlorophenol		8.97	128
4-chlorophenol		9.37	128
2,4-dichlorophenol		7.90	163
2,4,6-trichlorophenol		6.10	197
Pentachlorophenol		4.74	266

## 2.10. References

1. Cvacka, J.; Quaiserova, V.; Park, J.W.; Show, Y.; Muck, A. Jr.; Swain, G.M.; *Anal. Chem.* **2003**, *75*, 2678.
2. Jolley, S.; Koppang, M.; Jackson, T.; Swain, G.M.; *Anal. Chem.* **1997**, *69*, 4099.

## **CHAPTER 3**

# **The Physical and Electrochemical Characterization of Boron-Doped Diamond Thin- Film Electrodes**

### **3.1. Introduction**

Boron-doped diamond thin film can be grown with two different morphologies and microstructures: microcrystalline and nanocrystalline. The distinctions between the two are the surface roughness and the nominal grain size. For example, microcrystalline films have a nominal grain size of  $\sim 2 \mu\text{m}$ , or greater, and nanocrystalline films have a grain size on the order of 15 nm. <sup>1</sup> and references therein

It is important to have a good knowledge of the physical and chemical properties of the film if one is going to understand the electrochemical behavior. Therefore, detailed structural and electrochemical characterization of the films was carried out. The motivation for studying these two types of diamond stems from the fact that the different morphology and microstructure of each could

influence the electrode reaction kinetics, particularly for the electro-oxidation of chlorinated phenols.

Table 3.1 lists the instrumental techniques used to characterize the physical, chemical and electronic properties of diamond thin film along with the information gained from each.<sup>2,3</sup> Results from the characterization by atomic force microscopy, visible Raman spectroscopy, XRD and cyclic voltammetry using  $\text{Fe}(\text{CN})_6^{-3/4}$ ,  $\text{Ru}(\text{NH}_3)^{+2/+3}$ ,  $\text{IrCl}_6^{-2/-3}$ ,  $\text{MV}^{+2/+1/0}$ , 4-*tert*-butylcatechol,  $\text{Fe}^{+2/+3}$  as redox test probes, are presented in this Chapter.

**Table 3.1 Analytical Techniques Used for Film Characterization**

Technique	Information
Scanning Electron Microscopy	Morphology
Atomic Force Microscopy	Morphology
Raman Spectroscopy	Microstructure
X-ray Diffraction	Crystallinity
4-pt Probe Electrical Measurements	Electrical Resistivity
Contact Angle Measurements	Hydrophobicity

## 3.2. Results and Discussion

### 3.2.1. Morphology and Microstructure

Atomic force microscopy (AFM) was used to probe the morphology of the diamond thin film. Figure 3.1 shows typical images of a microcrystalline and nanocrystalline thin film.

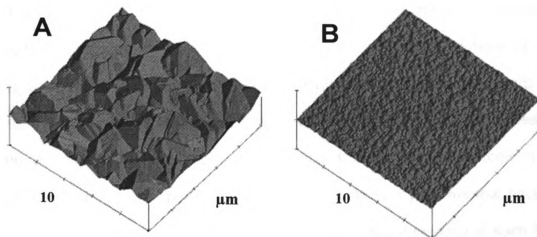


**Figure 3.1** AFM images showing a (A) microcrystalline and (B) nanocrystalline diamond thin film deposited on Si.

Microcrystalline films are polycrystalline and well-faceted with a predominance of octahedral and cubo-octahedral crystallites. The nominal crystallite size (lateral dimension at the base) is 2 μm or greater.<sup>1,4</sup> and references therein The nanocrystalline film is also polycrystalline but with a smoother surface, smaller feature sizes, and a greater fraction of grain boundary, as compared to the microcrystalline film. The nanocrystalline film consists of nodular features ~50 – 100 nm in diameter. The nodular features are actually clusters of individual

diamond crystallites that are 10 – 15 nm in diameter, formed as a result of the high renucleation rate.<sup>5</sup>

The different morphologies result from the growth conditions employed. As mentioned in Chapter 2, the conventional microcrystalline film is grown using 0.5 – 1.5 % CH<sub>4</sub>/H<sub>2</sub> source gas mixtures (i.e., hydrogen rich). It is known that, under such growth conditions, molecular H<sub>2</sub> must be dissociated into atomic hydrogen in order to accomplish a sequence of hydrogen abstraction reactions on the surface and in the gas phase. Methyl radicals (CH<sub>3</sub>·) and or (C<sub>2</sub>H<sub>2</sub>) are the primary growth species in hydrogen rich environments. Heterogenous nucleation of the diamond phase must compete with regasification of the embryonic nuclei by atomic hydrogen.<sup>6-8</sup> The end result is the survival of crystallites that become ever larger as a result of grain coarsening. The surface roughness of such films tends to track the grain size and film thickness.<sup>6-8</sup> A nanocrystalline film can be grown from CH<sub>4</sub>/Ar source gas mixture with little or no added H<sub>2</sub>. The nanocrystalline films, on the other hand, result from a growth and nucleation mechanism involving the insertion of the primary growth species, carbon dimer-C<sub>2</sub>, into surface C-H bonds. The C<sub>2</sub> addition is believed to occur by a two-step growth mechanism.<sup>9</sup> A C<sub>2</sub> molecule approaches the unreconstructed monohydride surface and inserts into a C-H bond. The C<sub>2</sub> then rotates to insert its other carbon into a neighboring C-H on the surface. A C<sub>2</sub> molecule then inserts into an adjacent C-H bond, parallel to the newly inserted C<sub>2</sub> dimer. The original state of the surface is recovered by the formation of a bond between



carbon atoms in the adjacent dimers. Very high renucleation rates are observed, on the order of  $10^{10}\text{cm}^{-2}$ , and the resulting film is morphologically smooth.<sup>8</sup> The smooth nanocrystalline films possess interesting mechanical, tribological, and electrical properties owing to their grain size. For example, the film transitions from an electrically insulating to a conducting material with a reduction in crystallite size from the micrometer to the nanometer level.<sup>10</sup> This is largely due to the presence of high-energy, high-angle grain boundaries that contain  $\pi$ -bonded carbon atoms. The grain boundaries are conducting because of the  $\pi$ -states, and since their number vastly increases with decreasing crystallite size, the entire film becomes electrically conducting and functions as an electrode material.<sup>11</sup>

Figure 3.2 shows visible-Raman spectra that reflect the microstructures for the microcrystalline and nanocrystalline films. Raman spectroscopy has been used extensively to characterize carbonaceous materials, including diamond.<sup>12-15</sup> Raman spectroscopy can be used to discriminate between  $sp^2$  and  $sp^3$ -bonded carbon as well as to probe the local bonding environment of the carbon. A spectrum with a single sharp peak at  $1332\text{ cm}^{-1}$  is seen for microcrystalline diamond. This is the first-order diamond phonon mode that originates from the  $sp^3$ -bonded carbon microstructure. An intense and narrow peak is characteristic of high quality diamond.<sup>16,17</sup> The spectrum shows negligible scattering in the region between  $1500$  and  $1600\text{ cm}^{-1}$ , where intensity is normally observed when significant amounts of  $sp^2$ -bonded carbon are present in several dispersed forms

within the CVD-grown polycrystalline diamond films. These include point defects within the diamond lattice and extended defects, such as twin planes and stacking faults at grain boundaries.<sup>18</sup>

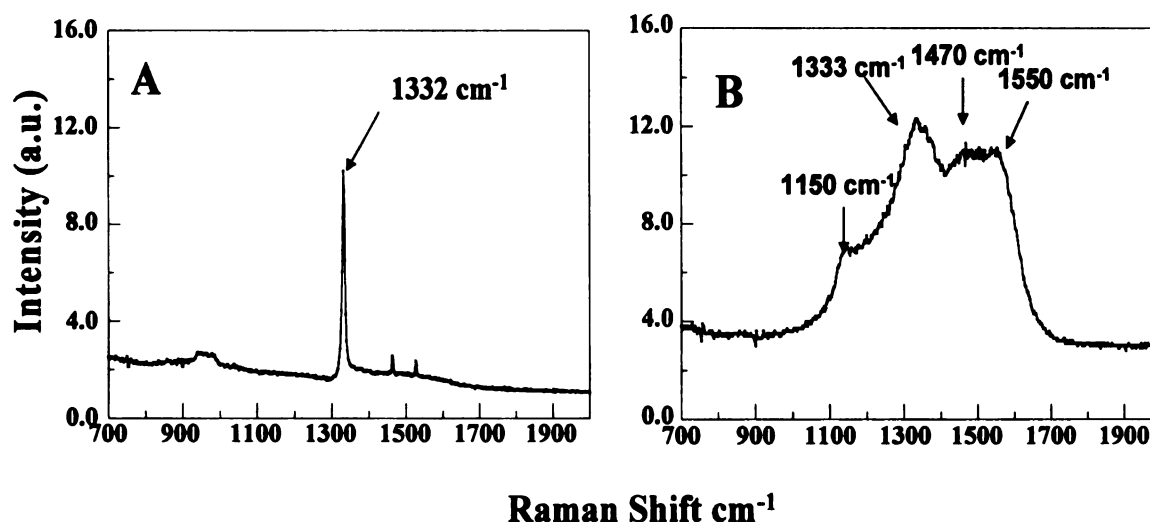


**Figure 3.2** Visible Raman spectra for a (A) microcrystalline and (B) nanocrystalline diamond thin film.

The spectrum for nanocrystalline diamond spectrum is quite different. Broad peaks are seen at 1150, 1333, 1470, and 1550 cm<sup>-1</sup>. The peak at 1333 cm<sup>-1</sup>, sitting atop a large background signal, is probably associated with the first-order phonon mode. Due to resonance effects, the Raman cross-section scattering coefficient for sp<sup>2</sup>-bonded carbon (e.g., graphite) is 50 times larger than that for sp<sup>3</sup>-bonded diamond.<sup>13</sup> The peak width (fwhm) for diamond line is much broader than that for the microcrystalline diamond. This is because of the small grain size.<sup>5</sup> There are two possible explanations for the line broadening. The first is the surface confinement model which states that the smaller the

domain size, the larger the range of phonon modes that are allowed to participate in the Raman process. The broad linewidth is due to the spread in phonon energy.<sup>19</sup> Another explanation is phonon scattering by impurities and defects (i.e., grain boundaries) as, to a first approximation, the phonon lifetime is inversely related to the defect density. The high grain boundary density reduces the phonon lifetime resulting in the increased linewidth.<sup>19</sup> The peak at  $1150\text{ cm}^{-1}$  is often used as a signature for high quality nanocrystalline diamond, but its origin has not yet been confirmed. Ferrari and Robertson assigned this peak to  $\text{sp}^2$ -bonded carbon, specifically transpolyacetylene segments at the grain boundaries.<sup>20</sup> Their assignment of the  $1150\text{ cm}^{-1}$  peak to  $\text{sp}^2$ -rather than  $\text{sp}^3$ -bonded carbon, as is often proposed, is based on the observations that the peak position changes with excitation energy, the peak intensity decreases with increasing excitation energy, and the peak is always accompanied by another peak at  $\sim 1450\text{ cm}^{-1}$ , which behaves similarly with excitation energy. The  $1550\text{ cm}^{-1}$  peak is assigned to disordered  $\text{sp}^2$  bonded carbon primarily in the grain boundaries. It is downshifted from the expected  $1580\text{ cm}^{-1}$  position as in graphite, because the  $\text{sp}^2$ -bonded carbon is amorphous and is mixed with  $\text{sp}^3$ -bonded carbon. In the nanocrystalline film, the  $\text{sp}^2$ -bonded carbon is confined to the abrupt grain boundaries which consist of a network of 3- and 4-fold coordinated carbon atoms.<sup>21</sup>

XRD was employed to characterize the bulk crystallinity of the diamond thin films. Figure 3.3 shows the XRD spectra for the (A) microcrystalline and (B)

nanocrystalline. For both films, three reflections are observed at  $2\theta$  values of  $44^\circ$ ,  $76^\circ$ , and  $92^\circ$ , and are assigned to the (111), (220), and (311) planes of cubic diamond, respectively.<sup>5</sup> The peaks for the nanocrystalline film are broader than those for the microcrystalline film due to the smaller grain size. This result confirms that both film types possess a crystalline diamond structure.

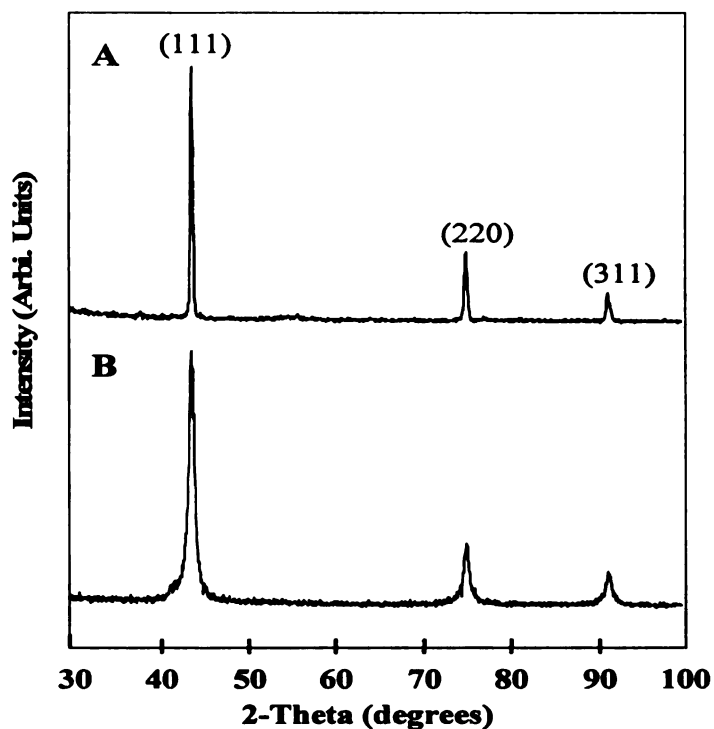


**Figure 3.3** XRD patterns for a (A) microcrystalline and (B) nanocrystalline diamond thin film.

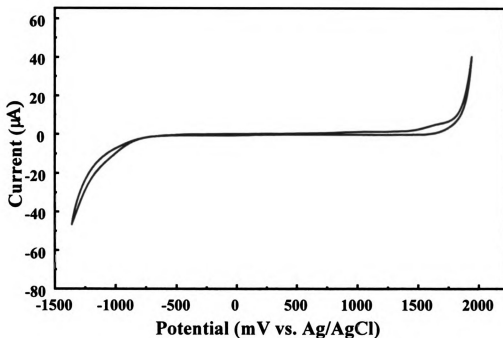
### 3.2.2. Electrochemical Responsiveness

Figure 3.4 shows a background voltammetric  $i$ - $E$  curve in 0.1 M  $\text{HClO}_4$  for a microcrystalline diamond film deposited on Si. The nanocrystalline diamond film exhibits a similar curve shape. Background voltammetric curves are useful for assessing diamond film quality.<sup>4</sup> The magnitude of the background current

and working potential window are highly sensitive to the presence of non-diamond  $sp^2$ -bonded carbon impurity.<sup>22</sup> This impurity, when present at significant levels, is located at the grain boundaries and defects. The  $i$ - $E$  curve is flat and featureless with no peaks present in the 0 – 0.5 V range that are indicative of redox-active surface carbon-oxygen functionalities.<sup>23</sup> The background current is low over the entire potential range between the solvent electrolysis limits. For example, the anodic current at 0.5 V is 1.5  $\mu$ A (8  $\mu$ A/cm<sup>2</sup>), whereas for glassy carbon the current is variable from 7 -10  $\mu$ A (35 - 50  $\mu$ A/cm<sup>2</sup>). The current at positive potentials begins to increase at 1.8 V due to the onset of oxygen evolution. The current at negative potentials begins to increase at -1.5 V due to hydrogen evolution. The scans were unchanged with multiple cycles reflecting the stability of the surface morphology and microstructure. The working potential window, defined as the potential range between current limits of  $\pm$  50  $\mu$ A, is  $\sim$  3.2 V. The wide working potential window permits the electrochemistry of redox systems with large positive or negative standard reduction potentials to be studied, something that would otherwise be impossible due to interference from solvent electrolysis.

The background current for both microcrystalline and nanocrystalline is less than that of a comparably sized glassy carbon electrode (a factor of 5 – 7 higher). A low background current and wide working potential window (3 - 4 V) are characteristic features of high quality boron-doped diamond electrodes.<sup>24</sup>

This leads to improved signal-to-background (SBR) and signal-to-noise (SNR) ratios in electroanalytical measurements.<sup>25</sup>



**Figure 3.4** Background cyclic voltammetric i-E curve in 0.1 M HClO<sub>4</sub> for a microcrystalline diamond film deposited on Si. Scan rate = 0.1 V/s. Electrochemical geometric area = 0.2 cm<sup>2</sup>.

The electrochemical response of both boron-doped microcrystalline and nanocrystalline diamond thin-film electrodes towards different redox systems was also investigated using cyclic voltammetry. The physical, chemical and electronic properties of the diamond influence the electrode kinetics and reaction mechanism for these systems to differing extents.<sup>5,25,26</sup> Ru(NH<sub>3</sub>)<sub>6</sub><sup>+2/+3</sup>, methyl viologen (MV<sup>+2/+1/0</sup>), IrCl<sub>6</sub><sup>-2/-3</sup>, Fe<sup>+2/+3</sup>, Fe(CN)<sub>6</sub><sup>-3/-4</sup>, and *tert*-butylcatechol were

used to probe the reactivity of the electrodes. These redox systems were chosen, in part, based on the fact that their  $E^0$  values span a wide potential range.

Redox reactions are generally of two types. One type is reactions that proceed by simple diffusion of the analyte to the electrode-solution interface, with the electrode serving solely as a source or sink for electrons. In this case, the electrode-reactions are relatively insensitive to factors such as surface chemistry and microstructure, but are very sensitive to the density of electronic states near the formal potential (so-called outer-sphere reaction). The other type includes reactions that occur via some specific interaction with the electrode surface; for example, reactions that proceed through an adsorbed state. In this case, the electrode reaction kinetics are sensitive to surface chemistry and microstructure as well as the density of electronic states near the formal potential (so called inner-sphere reaction). The redox systems  $\text{Ru}(\text{NH}_3)_6^{+2/+3}$ ,  $\text{IrCl}_6^{-2/-3}$ , and methyl viologen ( $\text{MV}^{+2/+1/0}$ ) are all outer-sphere in nature with the electrode kinetics being relatively insensitive to the physicochemical properties of diamond. Apparent heterogeneous electron-transfer rate constants,  $k_{\text{app}}^0$ , between 0.01 and 0.1 cm/s are commonly observed for both microcrystalline and nanocrystalline films without any conventional pretreatment.<sup>4,27-32</sup> Normally, carbon and metal electrodes must be pretreated to achieve such a large rate constant.  $\text{Fe}(\text{CN})_6^{-3/-4}$  proceeds through more of an inner-sphere electron-transfer pathway, as electrode kinetics are highly sensitive to the surface chemistry of diamond.<sup>31</sup> Presumably, the reaction proceeds through a specific surface interaction

available on the hydrogen-terminated surface. Such surface interactions seem to be blocked on the oxygen-terminated surface.  $k_{app}^0$  values ranging from 0.01 to 0.1 cm/s are commonly observed for clean, hydrogen-terminated films, but the rate constants decrease by over two orders of magnitude for oxygen-terminated films.<sup>33</sup> For  $sp^2$ -bonded carbon electrodes, the electrode kinetics are strongly influenced by the fraction of exposed, clean edge plane.<sup>34</sup>

Figure 3.5 and 3.6, respectively, shows cyclic voltammetric  $i$ - $E$  curves on boron-doped diamond microcrystalline and nanocrystalline in the presence of six redox systems (A)  $Fe(CN)_6^{-3/-4}$ , (B)  $Ru(NH_3)_6^{+2/+3}$ , (C)  $IrCl_6^{-2/-3}$ , (D) methyl viologen in 1 M KCl, and (E)  $Fe^{+2/+3}$ , (F) *tert*-butyl catechol in 0.1 M  $HClO_4$ . The potential scan rate was 0.1 V/s. The voltammograms were obtained with hydrogen-terminated electrodes. A summary of the voltammetric data is presented in Table 3.2 and 3.3. The CV data presented are the oxidation potential,  $E_p^{ox}$ , oxidation peak current,  $i_p^{ox}$ , oxidation and reduction peak current ratio,  $i_p^{ox}/i_p^{red}$ , and the peak potential separation,  $\Delta E_p$ . The  $\Delta E_p$  ( $\Delta E_p = E_p^{ox} - E_p^{red}$ ) is of particular importance because it is related to the heterogenous electron transfer rate constant.

The  $E^0$  values for these redox systems range from  $\sim +0.8$  to  $-1.1$  V, so they are useful for probing the film's electronic properties over a wide potential range. A nearly reversible response is observed for  $Fe(CN)_6^{-3/-4}$  with a  $\Delta E_p$  of 61 mV for both diamond film types. The  $i_p^{ox}/i_p^{red}$  was 1.1 and 1.0 for microcrystalline



and

sens

borc

cou

bon

surf

infl

pot

wo

in

nar

sur

65

An

als

nar

nar

red

sp<sup>2</sup>

mai

each

and nanocrystalline diamond thin film, respectively. This redox couple is quite sensitive to the physical and chemical properties of both glassy carbon and boron-doped diamond electrodes.<sup>5,28,32,34</sup> The electrode reaction kinetics for this couple are strongly influenced by the amount of exposed edge plane on  $sp^2$ -bonded carbon, as well as the surface cleanliness.<sup>34</sup> It has been shown that surface carbon-oxygen functionalities on microcrystalline diamond significantly influence  $\Delta E_p$ , with increasing oxygen content causing an increase in the peak potential separation.<sup>33</sup> Such an effect was also observed by Fujishima and co-workers.<sup>35</sup> The effect of surface oxygen is reversed if the film is rehydrogenated in a hydrogen plasma.<sup>25</sup> The small  $\Delta E_p$  seen for both microcrystalline and nanocrystalline boron-doped diamond electrodes is indicative of a high level of surface cleanliness, low oxygen coverage and high electrical conductivity.

A nearly reversible response is seen for  $Ru(NH_3)_6^{+2/+3}$  with  $\Delta E_p$  of 63 and 65 mV, respectively, for microcrystalline and nanocrystalline diamond thin film. An  $i_p^{ox}/i_p^{red}$  of 1.0 was observed for both films. A nearly reversible response is also seen for  $IrCl_6^{-2/-3}$  with a  $\Delta E_p$  of 63 mV on both microcrystalline and nanocrystalline diamond. The  $i_p^{ox}/i_p^{red}$  was 1.0 and 1.1 for microcrystalline and nanocrystalline diamond, respectively. The electrode kinetics for both of these redox systems are much less sensitive to the physicochemical properties of both  $sp^2$ -bonded carbon and  $sp^3$ -bonded diamond electrodes.<sup>28,32,34</sup> The kinetics are mainly influenced by the density of electronic states near the formal potential of each redox system. The relatively low  $\Delta E_p$  (or relatively rapid kinetics) for both

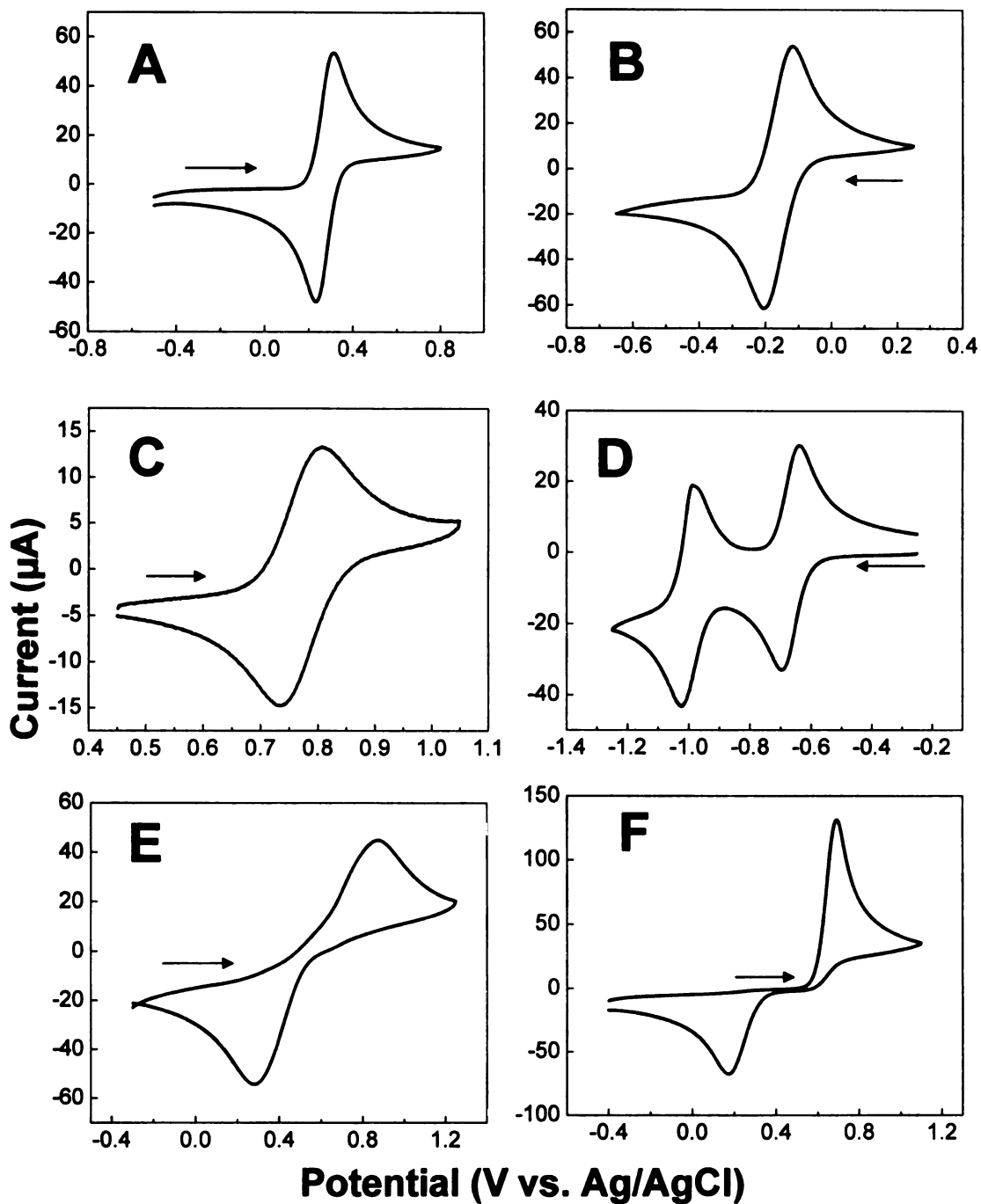


**Figure 3.5** Cyclic voltammetric i-E curves for (A)  $\text{Fe}(\text{CN})_6^{3-/4}$  (B)  $\text{Ru}(\text{NH}_3)_6^{2+/3}$  (C)  $\text{IrCl}_6^{2-/3}$  (D) methyl viologen in 1 M KCl, and (E)  $\text{Fe}^{2+/3}$ , (F) *tert*-butyl catechol in 0.1 M  $\text{HClO}_4$  at a boron-doped microcrystalline diamond thin-film electrode. Scan rate = 0.1 V/s. Electrode geometric area = 0.2  $\text{cm}^2$ .

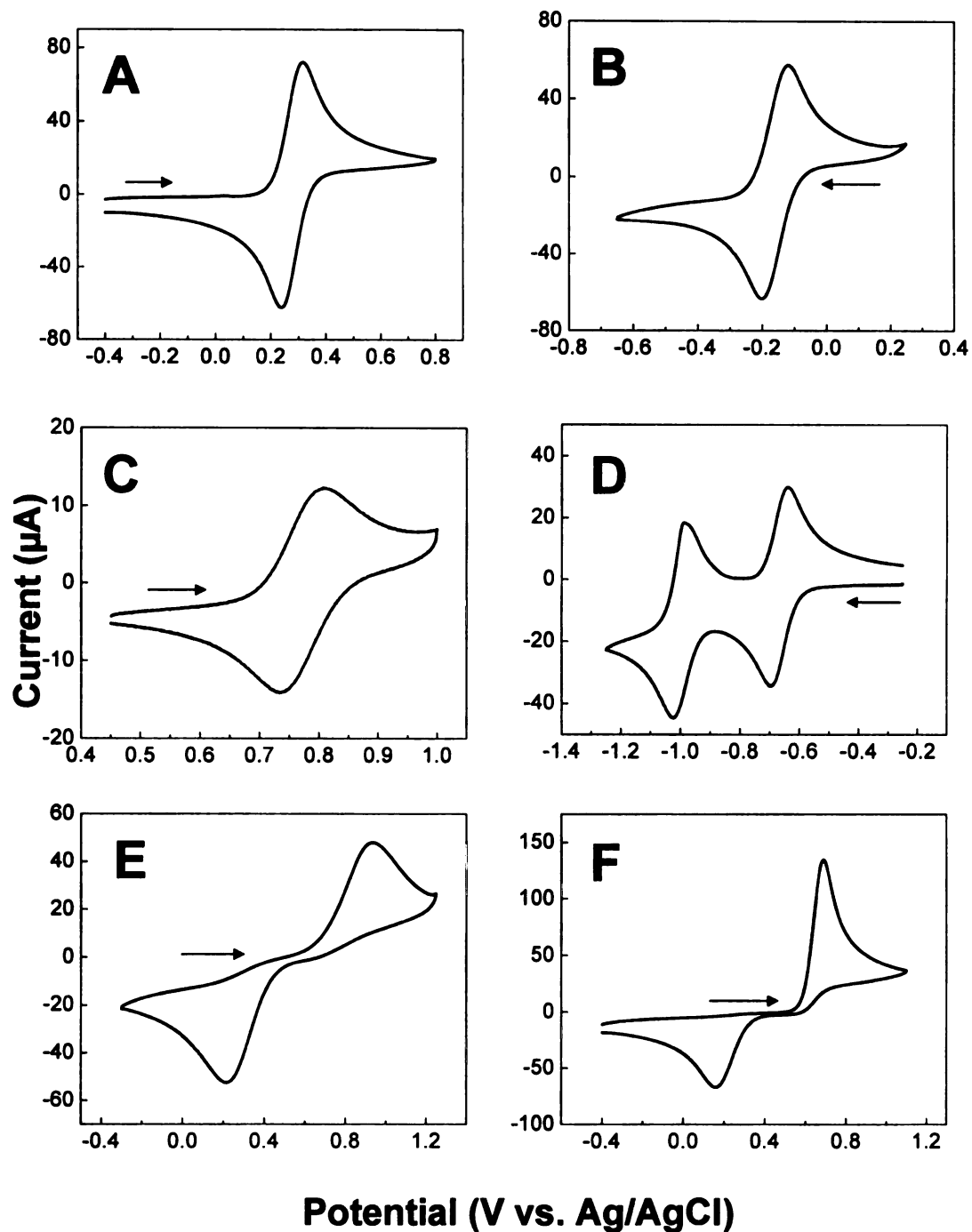


**Figure 3.6** Cyclic voltammetric i-E curves for (A)  $\text{Fe}(\text{CN})_6^{3-/4-}$  (B)  $\text{Ru}(\text{NH}_3)_6^{2+/3+}$  (C)  $\text{IrCl}_6^{2-/3-}$  (D) methyl viologen in 1 M KCl, and (E)  $\text{Fe}^{2+/3+}$ , (F) *tert*-butyl catechol in 0.1 M  $\text{HClO}_4$  at a boron-doped nanocrystalline diamond thin-film electrode. Scan rate = 0.1 V/s. Electrode geometric area = 0.2  $\text{cm}^2$ .

**Table 3.2 Cyclic Voltammetric Data for a Microcrystalline Boron-Doped Diamond Electrode**

Analyte	$\Delta E_p$ (mV)	$E_p^{ox}$	$I_p^{ox}$	$i_p^{ox}/i_p^{red}$
1 mM $Fe(CN)_6^{-3/4}$ in 1 M KCl	$61 \pm 3$	314	60	1.1
1 mM $Ru(NH_3)_6^{+2/+3}$ in 1 M KCl	$63 \pm 4$	-140	63	1.0
0.25 mM $IrCl_6^{-2/-3}$ in 1 M KCl	$63 \pm 4$	807	15	1.0
0.5 mM $MV^{+2/+1}$ in 1 M KCl	$60 \pm 5$	-601	32	1.2
1 mM t-butylcatechol in 0.1 M $HClO_4$	$460 \pm 7$	624	134	2.0
1 mM $Fe^{+2/+3}$ in 0.1 M $HClO_4$	$574 \pm 12$	857	43	0.9

Scan rate = 100 mV/s. Electrode area = 0.2 cm<sup>2</sup>

**Table 3.3 Cyclic Voltammetric Data for a Nanocrystalline Boron-Doped Diamond Electrode**

Analyte	$\Delta E_p$ (mV)	$E_p^{ox}$	$I_p^{ox}$	$i_p^{ox}/i_p^{red}$
1 mM $Fe(CN)_6^{-3/4}$ in 1 M KCl	$61 \pm 2$	311	73	1.0
1 mM $Ru(NH_3)_6^{+2/+3}$ in 1 M KCl	$65 \pm 4$	-137	65	1.0
0.25 mM $IrCl_6^{-2/-3}$ in 1 M KCl	$63 \pm 3$	809	14	1.1
0.5 mM $MV^{+2/+1}$ in 1 M KCl	$60 \pm 4$	-611	31	1.1
1 mM t-butylcatechol in 0.1 M $HClO_4$	$483 \pm 9$	635	134	2.1
1 mM $Fe^{+2/+3}$ in 0.1 M $HClO_4$	$685 \pm 10$	921	45	0.9

Scan rate = 100 mV/s. Electrode area = 0.2 cm<sup>2</sup>

microcrystalline and nanocrystalline diamond indicates that both diamond types possess a high density of electronic states at both -0.2 V over a wide potential range.<sup>36,37</sup>

A reversible response is also seen for  $MV^{+2/+1}$  with an  $\Delta E_p$  of 60 mV for both microcrystalline and nanocrystalline thin film. An  $i_p^{ox}/i_p^{red}$  of 1.2 and 1.1 was observed for microcrystalline and nanocrystalline, respectively. Like  $Ru(NH_3)_6^{+2/+3}$  and  $IrCl_6^{-2/-3}$ , the electrode reaction kinetics for  $MV^{+2/+1}$  are relatively insensitive to the physicochemical properties of both  $sp^2$ -bonded and diamond electrodes.<sup>28,32,38</sup> The kinetics are mainly influenced by the density of electronic states at the formal potentials. MV undergoes two redox reactions ( $MV^{+2/+}$  and  $MV^{+1/0}$ ). Good responsiveness was also observed for the other redox couple,  $MV^{+1/0}$ . The cathodic peak at  $\sim -1.0$  V is associated with the reduction of  $MV^{+1}$  to  $MV^0$ . The peak shape is consisted with diffusion-controlled reaction. The data for these four redox systems indicate that both diamond film types possess a high density of electronic states over a wide potential range.

The cyclic voltammetric  $i$ - $E$  curves for *tert*-butylcatechol (t-BC) and  $Fe^{+2/+3}$  have much larger  $\Delta E_p$  values and more asymmetric peak shapes than do the curves of the other redox couples.  $\Delta E_p$  values of 460 and 574 mV are observed for t-BC and  $Fe^{+2/+3}$ , respectively, for microcrystalline diamond. The large  $\Delta E_p$  values reflect more electrochemical irreversibility (i.e., more sluggish electrode reaction kinetics).<sup>5,28</sup> The  $i_p^{ox}/i_p^{red}$  ratios are 2.0 and 0.9 for t-BC and  $Fe^{+2/+3}$ ,

respectively, for microcrystalline diamond due to the reaction irreversibility. The  $\Delta E_p$  values of 483 and 685 mV are for t-BC and  $\text{Fe}^{+2/+3}$ , for nanocrystalline diamond. The  $i_p^{\text{ox}}/i_p^{\text{red}}$  ratios are 2.1 and 0.90 for t-BC and  $\text{Fe}^{+2/+3}$ , respectively. The catechol redox reaction involves a transfer of both electrons and protons, and the electrode kinetics are highly sensitive to the surface microstructure, the presence of surface carbon-oxygen functionalities, and the surface cleanliness of  $\text{sp}^2$ -bonded carbon electrodes.<sup>34</sup> Surface adsorption catalyzes the reaction rate.<sup>39</sup> It is postulated that the slow kinetics for diamond result from a lack of adsorption on the  $\text{sp}^3$ -bonded hydrogen-terminated diamond surface.<sup>40</sup> The electrode kinetics of  $\text{Fe}^{+2/+3}$  are strongly influenced by the presence of carbon-oxygen functionalities, specifically carbonyl groups, which catalyze the reaction rate at  $\text{sp}^2$ -bonded carbon electrodes.<sup>40</sup> The hydrogen-terminated diamond surface is void of such functionalities, so this is the postulated reason for the sluggish kinetics. Increasing the surface oxygen content on diamond has been observed to slightly decrease the  $\Delta E_p$ .<sup>35</sup> More research is needed to fully understand why the kinetics of this redox system are so sluggish on diamond.

Plots of  $i_p^{\text{ox}}$  versus scan rate<sup>1/2</sup> ( $v^{1/2}$ ) were constructed for  $\text{Fe}(\text{CN})_6^{-3/-4}$ ,  $\text{Ru}(\text{NH}_3)_6^{+2/+3}$ ,  $\text{IrCl}_6^{-2/-3}$ , methyl viologen,  $\text{Fe}^{+2/+3}$ , tert-butyl catechol redox systems at various scan rates (100 – 500 mV/s). Figure 3.7A presents plots of  $i_p^{\text{ox}}$  versus  $v^{1/2}$  for the different redox analytes at a boron-doped microcrystalline diamond electrode. It was observed that the oxidation peak current for each redox system varied with the scan rate<sup>1/2</sup> with a near- zero y-axis intercept, indicative of

reactions limited by semi-infinite linear diffusion of the reactant to the electrode surface. A similar trend was observed on the nanocrystalline diamond. Figure 3.7B shows a comparison for the experimental plot and theoretical prediction for the  $\text{Fe}(\text{CN})_6^{-3/4}$  for a microcrystalline diamond. The two curves are more or less comparable. The quasi-reversible to reversible voltammetry for these couples indicates that the boron-doped microcrystalline and nanocrystalline films have sufficient density of electronic states over a wide potential range to support rapid rates of electron-transfer.

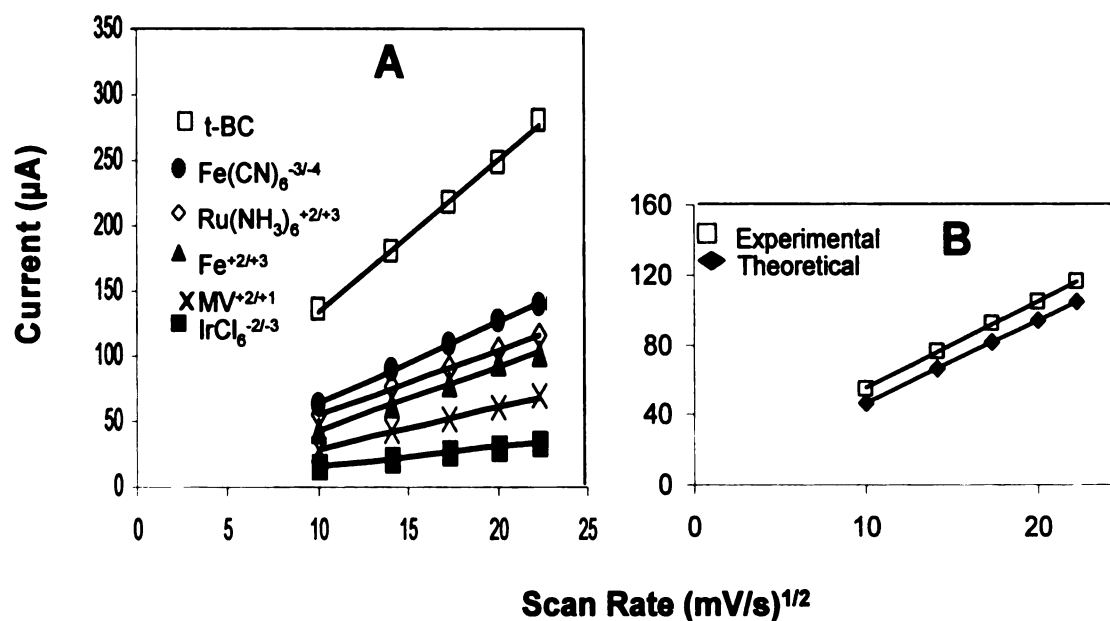


**Figure 3.7** (A) Plots of  $i_p^{\text{ox}}$  vs. scan rate<sup>1/2</sup> for  $\text{Fe}(\text{CN})_6^{-3/4}$ ,  $\text{Ru}(\text{NH}_3)_6^{+3/+2}$ ,  $\text{IrCl}_6^{-2/-3}$ , methyl viologen,  $\text{Fe}^{+2/+3}$ , tert-butyl catechol at a boron-doped microcrystalline diamond thin-film electrode. (B) Experimental and theoretical curves for  $\text{Fe}(\text{CN})_6^{-3/4}$ . Scan rate = 0.1 V/s. Electrode geometric area = 0.2 cm<sup>2</sup>. The scan rate was varied from 100 to 500 mV/s.



### 3.3. Conclusions

The physical characterization and electrochemical properties of boron-doped diamond thin film were discussed. Two types of conducting diamond, microcrystalline and nanocrystalline, with different morphologies and microstructures were investigated and compared. Both film types exhibited a wide working potential window, a low voltammetric background current and good responsiveness for  $\text{Fe}(\text{CN})_6^{-3/4}$ ,  $\text{Ru}(\text{NH}_3)_6^{+2/+3}$ , methyl viologen ( $\text{MV}^{+2/+1/0}$ ), and  $\text{IrCl}_6^{-2/-3}$  without any conventional pretreatment. The nearly reversible voltammetry (at 100 mV/s) for all four of these redox systems indicates that boron-doped microcrystalline and nanocrystalline diamond have a sufficient charge carrier concentration and carrier mobility over a wide potential range to support relatively rapid rates of electron-transfer for these analytes. More sluggish kinetics were found for *tert*-butylcatechol and  $\text{Fe}^{+2/+3}$  at both diamond types. The results were reproducible from electrode-to-electrode. The sluggish kinetics have been attributed to weak adsorption for the former, and to the absence of catalyzing surface carbonyl groups for the latter.

### 3.4. References

1. Swain, G.M.; Anderson, A.B.; Angus, J.C.; *MRS Bull.* **1998**, *23*, 56.
2. Xu, J.; Granger, M.C.; Chen, Q.; Strojek, J.W.; Lister, T.E.; Swain, G.M. *Anal. Chem.*; **1997**, *69*, 591 A.
3. Hupert, M.; Muck, A.; Wang, J.; Stotter, J.; Cvackova, Z.; Haymond, S.; Show, Y.; Swain, G.M.; *Diamond and Rel. Mater.* **2003**, *12*, 1940.
4. Granger, M.C.; Witek, M.; Xu, J.; Wang, J.; Hupert, M.; Hanks, A.; Koppang, M.D.; Butler, J.E.; Lucazeau, G.; Mermoux, M.; Strojek, J.W.; Swain, G.M.; *Anal. Chem.* **2000**, *72*, 3793.
5. Show, Y.; Witek, W.A.; Sonthalia, P.; Swain, G.M.; *Chem. Mater.*, **2003**, *15*, 879.
6. Butler, J.E.; Windischmann, H.; *MRS Bull.* **1998**, *23*, 22.
7. Gruen, D.M.; *MRS Bull.* **1998**, *23*, 32.
8. Gruen, D.M. *Annu. Rev. Mater. Sci.* **1999**, *29*, 211.
9. McCauley, T.G.; Gruen, D.M.; Krauss, A.R. *Appl. Phys. Lett.* **1998**, *73*, 1646.
10. Bhattacharyya, S.; Auciello, O.; Birrello, J.; Carlisle, J.A.; Curtiss, L.A.; Goyette, A.N.; Gruen, D.M.; Krauss, A.R.; Schlueter, J.; Sumant, A.; Zapol, P. *Appl. Phys. Lett.* **2001**, *79*, 1.
11. Chen, Q.; Gruen, D.M.; Krauss, A.R.; Corrigan, T.D.; Witek, M.; Swain, G.M. *J. Electrochem. Soc.* **2001**, *148*, 44.
12. Dennison, J.R.; Holtz, M.W.; Swain, G.M.; *Spectroscopy* **1996**, *10*, 1.
13. Knight, D.S.; White, W.B.; *J. Mater. Res.* **1989**, *4*, 385.
14. Nemanich, R.J.; Solin, S.A.; *Phys. Rev B* **1979**, *20*, 392.
15. McCreey, R.L.; Packard, R.T.; *Anal. Chem.* **1989**, *61*, 775A.
16. Keblinski, P.; Wolf, D.; Phillpot, S.R.; Gleiter, H.; *J. Mater. Res.* **1998**, *13*, 2077.

17. Nemanich, R.J.; Glass, J.T.; Lucovsky, G.; Shroder, R.E.; *J. Vac. Sci. Technol.* **1988**, *A6*, 1783.
18. Robins, L.H.; Farabaugh, E.N.; Feldman, A.J.; *J. Mater. Res.* **1990**, *5*, 2456.
19. Bergman, L.; Nemanich, R.J. *J. Appl. Phys.* **1995**, *78*, 6709.
20. Ferrari, A.C.; Robertson, J.; *Phys. Rev. B* **2001**, *63*, 121405.
21. Gruen, D.M.; Krauss, A.R.; Zuiker, C.D.; Csencsits, R.; Terminello, L.T.; Carlisle, J.A.; Jimenez, I.; Sutherland, D.G.J.; Shu, D.K.; Tong, W.; Himpshel, F.; *J. Appl. Phys. Lett.* **1996**, *68*, 1640.
22. Bennett, J.A.; Wang, J.; Show, Y.; Swain, G.M.; *J. Electrochem. Soc.* **2004**, *151*, E306.
23. Chen, Q.; Swain, G.M.; *Langmuir* **1998**, *14*, 7017.
24. Swain, G.M.; Anderson, A.B.; Angus, J.C.; *MRS Bull.* **1998**, *23*, 56.
25. Strojek, J.W.; Granger, M.C.; Swain, G.M.; Dallas, T.; Holtz, M.W.; *Anal. Chem.* **1996**, *68*, 2031.
26. Witek, M.; Wang, J.; Stotter, J.; Hupert, M.; Haymond, S.; Sonthalia, P.; Swain, G.M.; Zak, J.K.; Chen, Q.; Gruen, D.M.; Butler, J.E.; Kobashi, K.; Tachibana, T.; *J. WideGap Mater.* **2002**, *8*, 171.
27. Chen, Q.; Gruen, D. M. ; Krauss, A. R.; Corrigan, T. D.; Witek, M.; Swain, G.M.; *J. Electrochem. Soc.* **2001**, *148*, E44.
28. Wang, J.; Swain, G.M.; Mermoux, M.; Lucazeau, G.; Zak, J.; Strojek, J.W.; *New Diamond and Frontier technology* **1999**, *9*, 317.
29. Haymond, S.; Babcock, G. T.; Swain, G. M.; *Electroanalysis*, **2003**, *15*, 249.
30. Xu, J.; Granger, M.C.; Chen, Q.; Strojek, J.W.; Lister, T.E.; Swain, G.M.; *Anal. Chem.* **1997**, *69*, 591A.

31. Granger, M.C.; Xu, J.; Strojek, J.W.; Swain, G.M.; *Anal. Chim. Acta.* **1999**, *397*, 145.
32. Granger, M.C.; Witek, M.; Xu, J.; Wang, J.; Hupert, M.; Hanks, A.; Koppang, M.D.; Butler, J.E.; Lucazeau, G.; Mermoux, M.; Strojek, J.W.; Swain, G.M.; *Anal. Chem.* **2000**, *72*, 3793.
33. Granger, M.C.; Swain, G.M.; *J. Electrochem. Soc.* **1999**, *146*, 4551.
34. Chen, P.; McCreeey, R.L.; *Anal. Chem.* **1996**, *68*, 3958.
35. Yagi, I.N.H.; Kondo, T.; Tryk, D.A.; Fujishima, A.; *J. Electroanal. Chem.* **1999**, *173*, 473.
36. Alehashem, S.; Chambers, F.; Strojek, J.W.; Swain, G.M.; Ramesham, R.; *Anal. Chem.* **1995**, *67*, 2812.
37. Pleskov, Y.V.; Mazin, V.M.; Evstefeeva, Y.E.; Varnin, V.P.; Teremeskaya, I.G.; Laptev, V.A.; *Electrochem. Solid, State Lett.* **2000**, *3*, 141.
38. Qui, F.; Compton, R.G.; Marken, F.; Wilkins, S.J.; Goeting, C.H.; Foord, J.S.; *Anal. Chem.* **2000**, *72*, 2362.
39. Vall, S.D.; Yang, H.-H.; McCreery, R.L.; *Proceedings-Electrochemical Society* **1999**, *99-5*, 33.
40. McDermott, C. A.; Kneten, K. R.; McCreery, R. L. *J. Electrochem. Soc.* **1993**, *140*, 2593.

## CHAPTER 4

# Cyclic Voltammetric Studies of the Electro-oxidation of Chlorinated Phenols at Boron-Doped Diamond Thin-Film Electrodes

### 4.1. Introduction

The phenol oxidation reaction mechanism is complex with multiple pathways possible. The first is the formation of a phenoxy radical due to the loss of 1 proton and 1 electron (Figure 4.1).

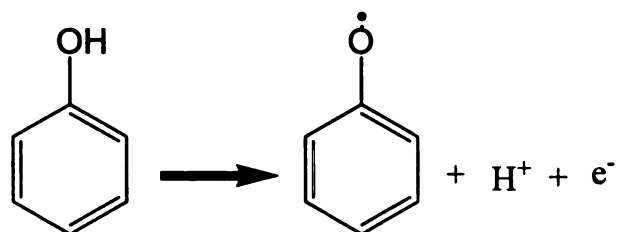


**Figure 4.1** Phenoxy radical formation during the initial stage of the electro-oxidation of phenol.

This species then undergoes further oxidation to form soluble products (e.g., quinones and hydroquinones) and/or anion-radical or radical-radical coupling

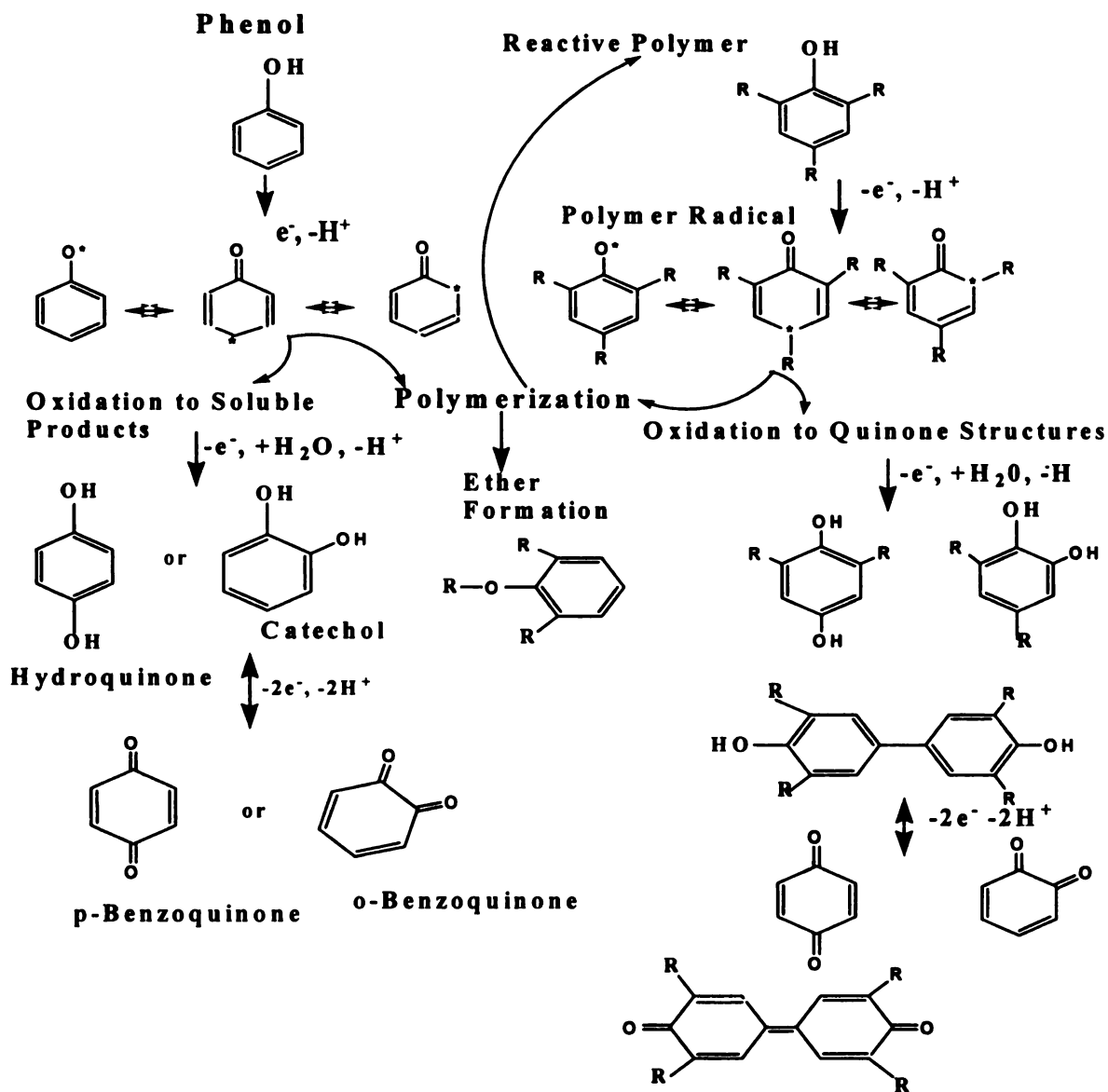


**Figure 4.2** The different possible reaction pathways for phenol oxidation (where R = hydrogen or an adjacent ring in the polymer structure).<sup>5</sup>

to form oligomeric and polymeric products.<sup>1-7</sup> Some coupling reactions may produce ether type linkages, resulting in structures less reactive than phenol. The

oligomeric and polymeric radical, like the phenol radical, can be further oxidized to form hydroquinone and catechol species.<sup>7</sup> Further oxidation to benzoquinone moieties are also possible. Figure 4.2 depicts the possible electro-oxidation pathways for a phenol molecule. The polymeric products are characterized by low permeability, low solubility in aqueous media, and a tendency to strongly adsorb on electrode surfaces.<sup>1</sup> The tendency of the polymeric products (e.g., polyphenol) to deposit on the electrode surface is the main reason for electrode deactivation during the electro-oxidation of phenols. The adsorption passivates the electrode for further electron transfer.

Most electrodes (e.g., Fe, Cu, Ni, Cr, Ti, Zn, Au, Pt, and Ag) are rapidly deactivated and fouled during the early stages of phenol oxidation.<sup>2,4,9-12</sup> The extent of passivation/fouling, however, depends on several parameters including the phenol concentration, surface chemistry of the electrode, solution pH, solvent additives, electrode potential, and current density.<sup>2,5</sup> For example, in alkaline solution, the formation of the C-O-C bonds prevails over the C-C coupling, while in acidic solution, the C-C coupling is more favored compared to formation of ether linkage.<sup>8,12</sup> The anodic oxidation of phenols bearing halogen substituents proceeds with some halogenide elimination in addition to the carbon-oxygen coupling mechanisms.<sup>6</sup> In general, elimination of the halogen during oxidation of halophenols proceeds following a substitution radical-nucleophilic mechanism.<sup>13</sup>

Various approaches have been used to minimize the deactivation and fouling problem. One is to optimize the electro-oxidation conditions as fouling can be minimized at low phenol concentrations, elevated temperatures, and large values of applied overpotential. The latter increases the rate of anodic discharge of  $\text{H}_2\text{O}$  to generate  $\text{OH}\bullet$ .<sup>4,7</sup> The  $\text{OH}\bullet$  oxidatively degrades the adsorbed oligomeric and/or polymeric reaction products, thereby removing them from the surface. Another approach is to chemically modify the electrode surface. For example, electrode surfaces have been modified with enzymes to enhance the oxidative reactivity.<sup>14</sup> However, this approach has the drawbacks of complexity and maintenance of the enzyme activity overtime.

Boron-doped diamond thin film is an advanced electrode material that shows less tendency to deactivate and foul during phenol oxidation. There have been several reports on the phenol and chlorinated phenols at conductive diamond.<sup>15,16,17,18,19</sup> Fujishima and co-workers discussed the electrochemical oxidation and detection of chlorinated phenols at anodically pretreated diamond (i.e., oxidized). The oxidized electrodes exhibited good response stability and reproducibility with low detection limits for several chlorinated phenols. They reported that some fouling occurred at high phenolic compound concentrations (5 mM), but the electrodes could effectively be reactivated by anodic treatment at 2.6 V vs. SCE for 4 min.<sup>15</sup> The authors postulated that the treatment generates  $\text{OH}\bullet$ , which oxidatively degrades the passivating polymer layer. In another report, Comninellis and co-workers investigated the electrochemical oxidation of 4-



chlorophenol at a boron-doped diamond thin-film electrode.<sup>16</sup> Under their conditions, the formation of phenoxy radicals, 1,4-benzoquinone, and polymeric products were observed. O'Grady and co-workers demonstrated that phenol can be oxidatively degraded to CO<sub>2</sub> at boron-doped diamond stably over time without electrode fouling.<sup>17</sup> Several other workers have addressed the electro-oxidation reaction mechanism in acidic media at diamond electrodes.<sup>18,20-22</sup> For example, Zhi et al. reported evidence for the direct electrochemical oxidation pathway for phenol at diamond electrodes.<sup>18</sup>

In this Chapter, a comparison of the electrochemical performance of boron-doped, hydrogen-terminated microcrystalline and nanocrystalline diamond thin-film electrodes for the electro-oxidation of chlorinated phenols is described. Cyclic voltammetry (CV) was used to study the oxidation of several chlorinated phenols. The technique involves linearly scanning the potential applied to an electrode from an initial value to a switching potential and then back to the initial value. A potentiostat controls the potential applied to the working electrode with respect to a reference electrode and measures the current that flows between the working and counter electrodes. The resulting data is a plot of current versus potential called a cyclic voltammogram. CV is a versatile technique useful for studying the thermodynamics of redox processes, evaluating the effects of various parameters and conditions on the redox reaction kinetics and mechanisms, and investigating coupled chemical reactions and adsorption processes. The technique is also useful for determining the redox potentials of

the electroactive species.<sup>23,24,25</sup> The goal for this work was to learn how the physicochemical properties of the diamond electrode affect the oxidation reaction kinetics and mechanism of the chlorinated phenols. The analytes studied were phenol, 2-chlorophenol, 3-chlorophenol, 4-chlorophenol, and pentachlorophenol in acidic medium.

## **4.2. Results and Discussion**

Cyclic voltammetric measurements using both microcrystalline and nanocrystalline diamond thin film were conducted. The first task was to compare the background voltammetric responses of both film types with that of glassy carbon (GC), a commonly used carbon electrode material. Background cyclic voltammetric *i*-*E* curves for GC, and microcrystalline and nanocrystalline diamond thin film in 0.05 M phosphate buffer, pH 3.5, are presented in Figure 4.3. The cyclic voltammetric *i*-*E* curves for both diamond types are featureless with no evidence for any surface redox chemistry. It can also be seen that the two types of diamond have a larger overpotential for oxygen evolution than does GC. The background current for GC is larger than for either diamond type. For example, the anodic background current at 0.45 V for GC is a factor of 5 larger than that for microcrystalline diamond and a factor of 3 larger than that for nanocrystalline diamond. The magnitude of the background current showed some variability from GC sample-to-sample but, in all cases, was larger than either diamond type. As a result, the oxidation current for the chlorophenols at

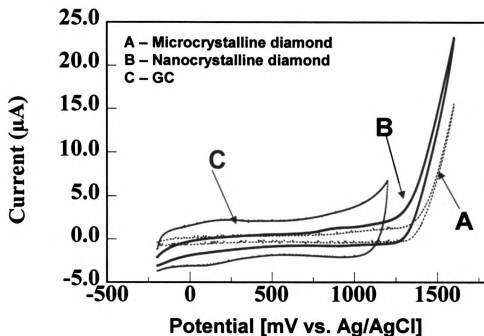


**Figure 4.3** Cyclic voltammetric i-E curves for a (A) microcrystalline, (B) nanocrystalline diamond thin-film electrodes, and (C) GC in 0.05 M phosphate buffer, pH 3.5. Scan rate = 100 mV/s. Electrode geometric area = 0.2 cm<sup>2</sup>.

GC is superimposed on a large and sometimes changing background signal, while the oxidation current at either type of diamond is recorded against a low and unchanging background. The broad oxidation and reduction peaks present near 0.2 V, are possibly associated with redox-active surface carbon-oxygen functionalities (e.g., quinone and hydroquinone couple) formed at the exposed edge planes.<sup>26</sup> During the surface pretreatment of GC, carbon-carbon bonds are broken, leaving dangling bonds on the surface. Upon air exposure, atmospheric oxygen and/or water will react with the dangling bonds to form carbon-oxygen functional groups.<sup>26</sup> Some of the resulting functional groups are electroactive.

The low and stable background current, as well as the large overpotential for oxygen evolution are characteristic features of the diamond electrodes. Improved S/B and signal-to-noise (S/N) ratios are often observed in measurements with this electrode material because of the low background current. There are three factors responsible for the low background current. First, a reduced pseudocapacitance due to the absence of redox-active and/or ionizable carbon-oxygen functional groups on the surface. The increased background current of GC is, in part, due to surface carboxylic acid functional groups that deprotonate at pH values above the  $pK_a$  of ca. 4.5.<sup>27</sup> The excess surface charge increases when these functional groups are deprotonated and this leads to an increased double layer charging current. Second, the semimetal-semiconductor nature of the diamond electrode leads to a slightly lower density of surface electronic states near the Fermi level. The lower surface charge density results in a reduced accumulation of counterbalancing ionic charge on the solution side of the interface during double-layer charging. This results in a lower background current. Third, the diamond film appears to consist of regions of high electrical conductivity separated by zones of less conductivity, as recently been observed by conductivity-probe AFM. This means that the effective electrode area is less than the geometric area; the latter is the value used to normalize currents.

The background current for nanocrystalline diamond is slightly larger than that for microcrystalline diamond presumably due to the increased fraction of

grain boundaries and  $\pi$ -bonded carbon that resides there. The  $\pi$ -bonded carbon is a source of charge carriers, which can increase the capacitive component of the background current. Some of these carbons may also contain electrochemically-active surface carbon-oxygen functionalities that would give rise to a faradaic component in the background current.<sup>28</sup>

Cyclic voltammetric *i*-*E* curves for phenol, 2-chlorophenol (2-CP), 3-chlorophenol (3-CP), 4-chlorophenol (4-CP), and pentachlorophenol (PCP), all in 50 mM phosphate buffer, pH 3.5, were recorded for both diamond types. The cyclic voltammetric responses for phenol, 2-CP, and 4-CP are similar in shape for both diamond types (Figure 4.4). The electrochemical response of 2-CP is used herein to exemplify the voltammetric behavior for all the three. The first forward scan exhibits a single, well-defined oxidation peak at ca. 1.1 V (peak a). The relatively stable peak charge after five scans ranged from 23 to 30  $\mu\text{C}$  for all three analytes. This current is due to the oxidation (via loss of 1  $e^-$  and 1  $\text{H}^+$ ) to form 2-chlorophenoxy radical. This oxidation peak occurs near the onset of oxygen evolution so that oxidant,  $\text{OH}\cdot$ , is also being generated. This oxidant can attack the 2-chlorophenoxy radical and oxidize it via an anodic oxygen transfer reaction. Of particular importance is the addition of OH groups to the aromatic ring.<sup>15-17</sup> Oxidation products, such as hydroquinone and catechol, are initially formed.<sup>15</sup> However, at these anodic potentials, the hydroxylated products can undergo further oxidation (via electron and proton loss) to form quinone-like species. It is these quinone-like oxidation products that are reduced during the

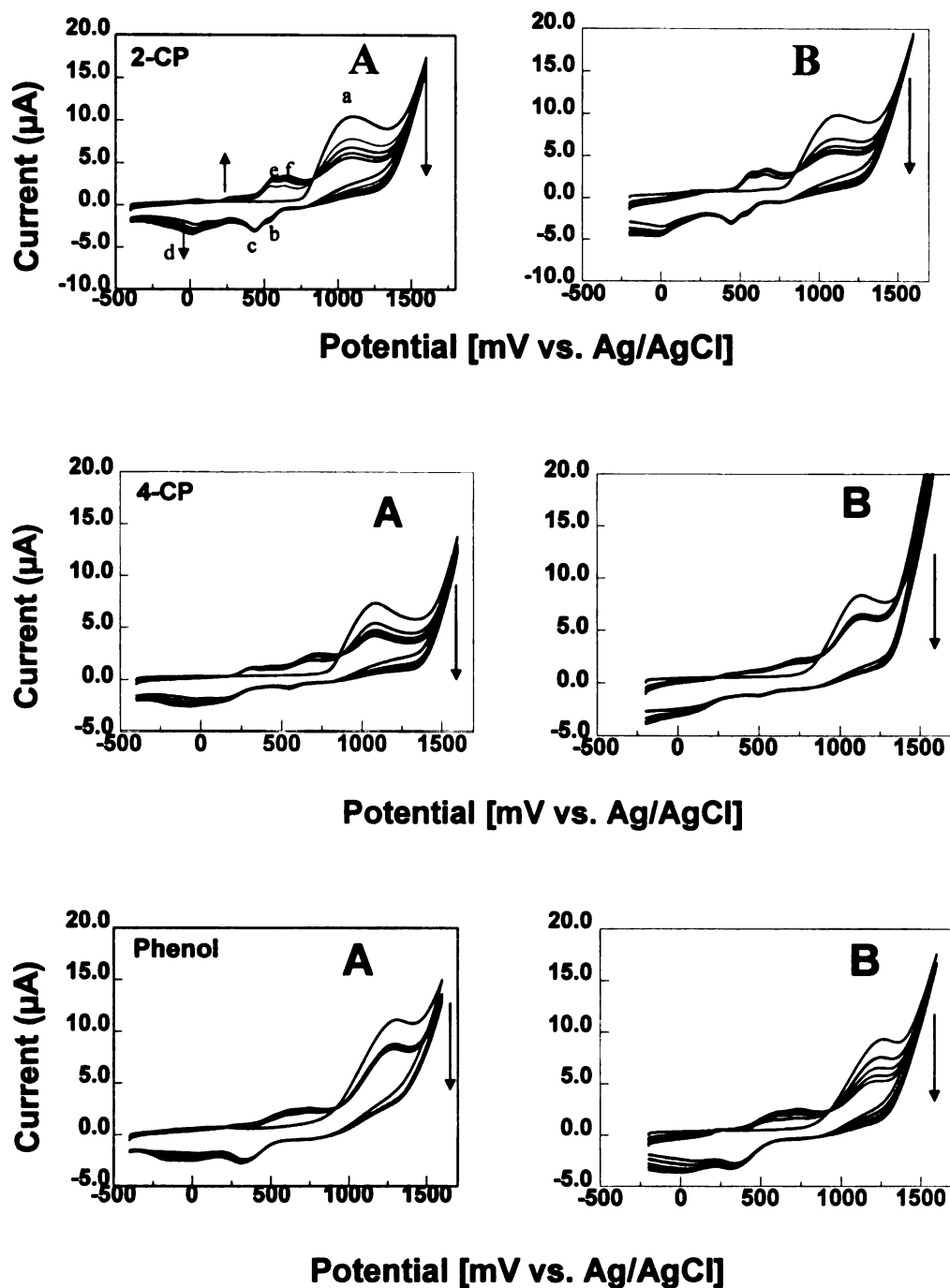


**Figure 4.4** Cyclic voltammetric  $i$ - $E$  curves for 2-CP, 4-CP, and phenol at a (A) microcrystalline and, (B) nanocrystalline diamond thin-film electrode in 0.05 M phosphate buffer, pH 3.5. Scan rate = 100 mV/s. Electrode geometric area = 0.2 cm<sup>2</sup>.

first negative-going sweep, as evidenced by the two reduction peaks at 0.55 and 0.48 V (peaks b and c). There is also a broad reduction wave at 0.05 V (peak d). The reduced species at 0.55 and 0.48 V can be reoxidized at 0.55 and 0.60 V (peaks e and f) during the positive-going scan. The peak currents for these reactions grew with cycle number, stabilizing after the fifth scan. Reduction peaks b and c are associated with the oxidation products of peaks e and f, as all were present when the forward scan was reversed at 0.8 V. The peak currents for a,  $i_p^{ox}$ , and d,  $i_p^{red}$ , at both electrode types varied linearly with  $v^{1/2}$  between 0.05 to 0.25 V/s ( $r^2 > 0.990$ ) indicating that the reaction rates for the initial oxidation of 2-CP and the reduction of the product(s) formed are controlled by semi-infinite linear diffusion of the reactant to the electrode surface. This means that soluble rather than surface-confined reactants and products are involved in the redox reactions. Rodrigo et al. observed similar voltammetric features for 4-CP and reported that the peak currents, a and d, increased with the addition of hydroquinone to the solution.<sup>16</sup> Therefore, we suppose that peak d is associated with the reduction of a dissolved quinone-like product formed at 1.1 V.

The currents for peaks b and c, and e and f, on the other hand, increased linearly with scan rate ( $r^2 > 0.990$ ), consistent with surface-confined redox processes. Further evidence that these redox reactions involve adsorbed species is the fact that the peak currents were, for most part, unaffected by electrolyte stirring. In these measurements, five cyclic voltammetric scans were recorded between -0.5 and 1.5 V to form the adsorbed oxidation reaction products. The

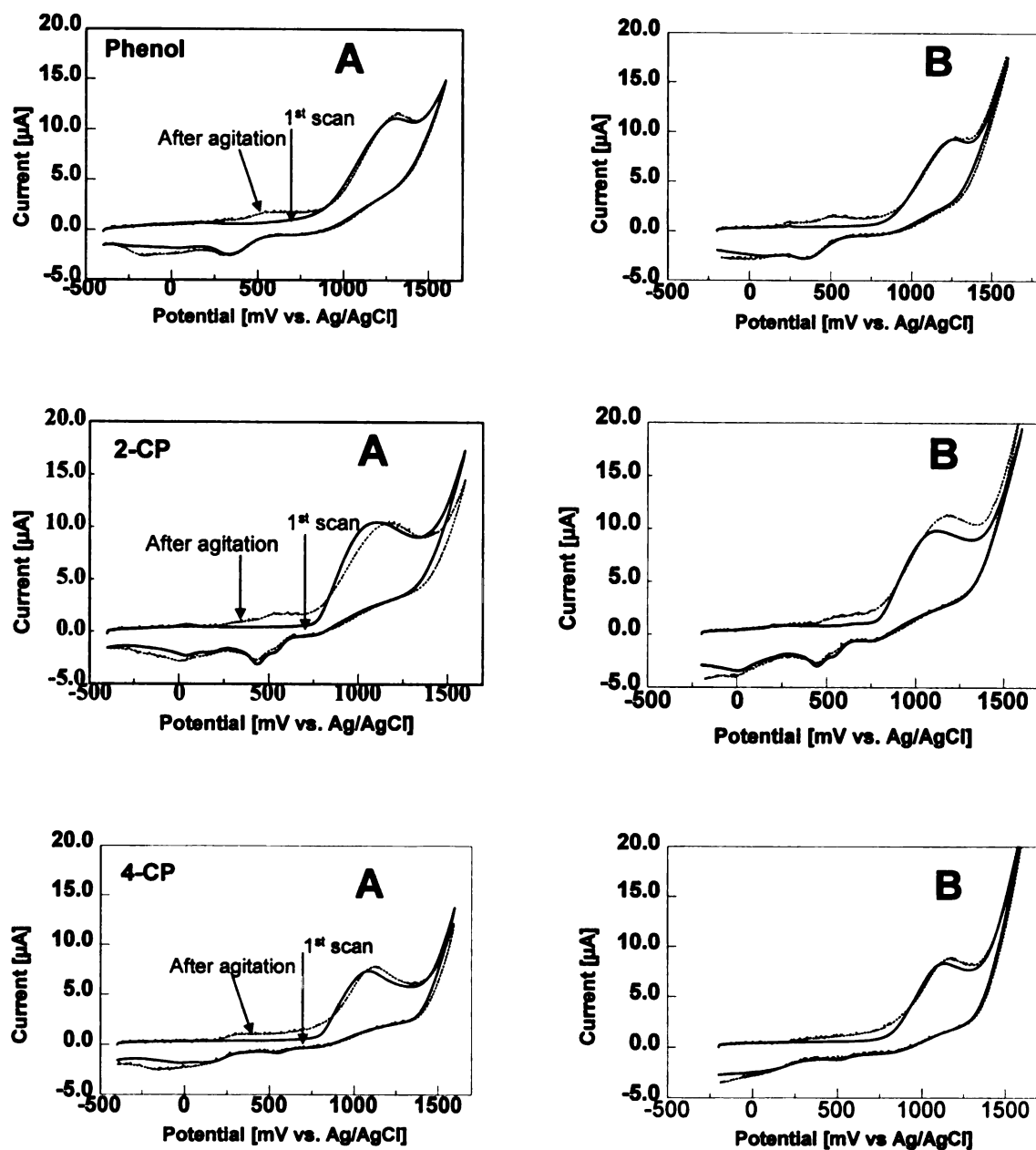


**Figure 4.5** Cyclic voltammetric i-E curves for phenol, 2-CP, and 4-CP at (A) microcrystalline and (B) nanocrystalline diamond thin-film electrode in 0.05 M phosphate buffer, pH 3.5. Scan rate = 100 mV/s. Electrode geometric area = 0.2 cm<sup>2</sup>.



analyte containing solution was then vigorously agitated for several minutes by bubbling with nitrogen gas. Figure 4.5 shows voltammetric responses for 0.1 mM solutions of phenol, 2-CP, and 4-CP for (A) microcrystalline and (B) nanocrystalline diamond electrodes before and after agitation. Oxidation peaks, e and f, and reduction peaks, b and c, were still present after the bubbling, although with minor current attenuation. However, if the analyte-containing solution was removed from the cell, the electrode copiously rinsed with ultrapure water, and the cell filled with fresh electrolyte, then the background voltammetric i-E curves were devoid of these redox peaks. This indicates that these oxidation reaction products are weakly adsorbed to the diamond surface. We suppose that these surface confined oxidation reaction products are either individual molecules adsorbed on the diamond surface, perhaps at localized sites where some oligomeric quinone structures has formed. For 2-CP and 4-CP, the corresponding chlorinated or non-chlorinated hydroquinone/benzoquinone is expected.<sup>22</sup> The fact that the primary oxidation peak current at 1.1 V is not significantly attenuated with prolonged potential cycling indicates that a blocking polyphenol layer does not form on the surface. In other words, some polymer may form on the electrode surface, but large uncoated areas of the electrode exist for the primary oxidation reaction to occur.

We suppose that the oxidation current at 1.1 V is due to a direct one-electron, one- proton oxidation of the phenol to form 2-chlorophenoxy radical.<sup>2,5</sup> It has been reported that the  $E_p^{ox}$  for the oxidation of 2,4-dichlorophenol at “as

deposited" (i.e., presumably hydrogen-terminated) diamond shifts less positive potentials with increasing pH up to the  $pK_a$  value of ca. 8. A change of -59 mV/dec was found.<sup>16</sup> This trend is consistent with an equal number of protons and electrons being transferred during the redox reaction. Rodrigo et al. have reported that this oxidation peak results from the one-electron/one-proton oxidation to phenoxy radical or from an additional one-electron oxidation to form phenoxy cation.<sup>17</sup> The seminal mechanistic work by Gattrell and Kirk indicates that the phenol oxidation reaction (and presumably for chlorinated phenols as well) proceeds initially through the formation of the phenoxy radical.<sup>1,2,5,7</sup> Once formed the radicals can react via two pathways: (i) radical-radical coupling to form oligomeric and polymeric species or (ii) subsequent direct or indirect oxidation to produce soluble or surface confined oxidation products, like benzoquinone and catechol.

The voltammetric responses for 3-CP and PCP were similar in shape at both electrode types, but quite different from the responses for the other three phenols. Figure 4.6 shows five consecutively recorded cyclic voltammograms for 0.1 mM PCP at a (A) microcrystalline and (B) nanocrystalline diamond thin-film electrode. The first forward scan for both electrodes shows a well-defined oxidation peak at ca. 0.90 V with a corresponding reduction peak at ca. -0.20 V during the reverse scan. The oxidation peak occurs at a potential less positive than the peak for phenol, 2-CP and 4-CP by approximately 200 mV. This is because the  $pK_a$  for PCP is 4.74, as compared to values of 8 to 10 for phenol

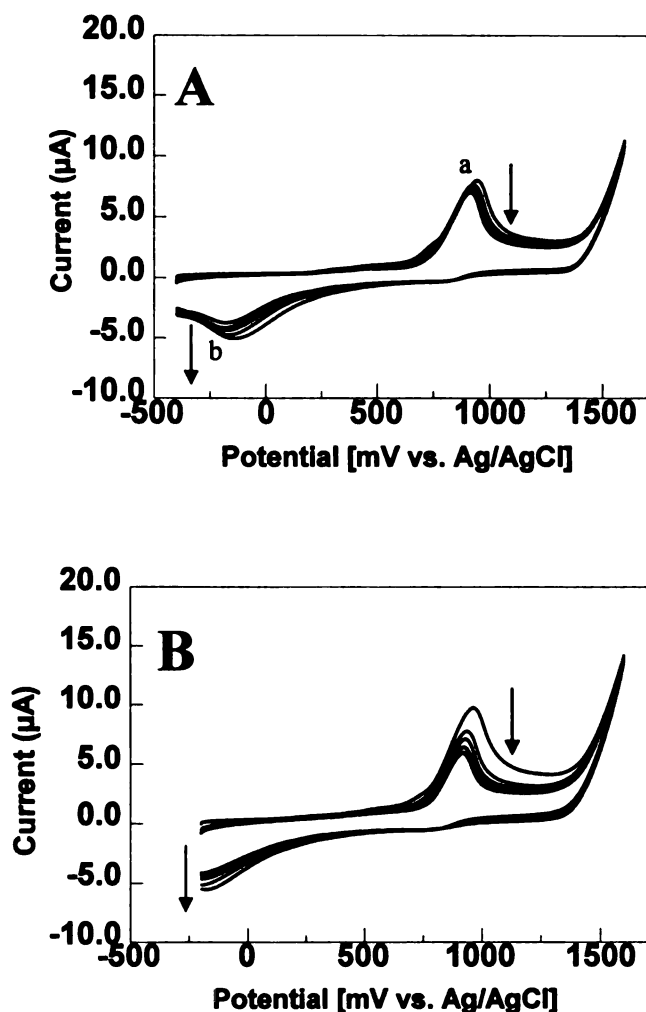


**Figure 4.6** Cyclic voltammetric i-E curves for 0.1 mM PCP at a (A) microcrystalline and (B) nanocrystalline diamond thin-film electrode in 0.05 M phosphate buffer, pH 3.5. Scan rate = 100 mV/s. Electrode geometric area = 0.2 cm<sup>2</sup>.

and the other chlorinated phenols. The lower value reflects a greater ease of deprotonating the phenolic hydrogen. The oxidation peak charge, after stabilization, was nominally 18 µC. The 0.90 V peak is presumed to be

associated with the formation of the dimer 2,3,4,6-pentachlorophenoxy-2,5-cyclohexadienone.<sup>11</sup> Gattrell and MacDougall studied the electrochemical oxidation of PCP and concluded that the reaction involves the loss of one electron and one proton to form pentachlorophenoxy radical. The radical then undergoes radical-radical coupling to form a dimer.<sup>11</sup> A slight decrease in the oxidation current and a slight increase in the reduction current are observed for the second and all subsequent scans. It is unclear at this point what reaction is associated with the reduction current. The pentachlorophenoxy radical most likely dimerizes to form a water insoluble species through C-O rather than C-C coupling due to steric limitations. The dimers formed could be 2,3,4,5,6-pentachloro-4-pentachlorophenoxy-2,5-cyclohexadienone and/or 2,3,4,5,6-pentachloro-2-pentachlorophenoxy-3,5-cyclohexadienone.<sup>11</sup> Figure 4.7 shows preliminary AFM images of a microcrystalline diamond electrode after 25 voltammetric scans in 0.1 mM PCP. The image reveals the presence of deposits on the surface, as indicated by the arrows. The deposits are formed all over the surface, but large clusters are found to be localized along grain boundaries. The deposits are water insoluble species mentioned above.

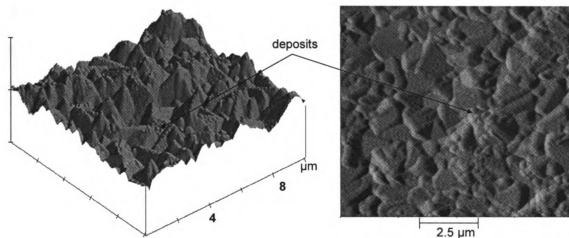


**Figure 4.7** AFM images of a microcrystalline diamond thin-film electrode after 25 cycles in 0.1 mM PCP in 0.05 M phosphate buffer, pH 3.5. Experimental conditions as in Figure 4.6.

Figure 4.8 shows five consecutive cyclic voltammograms for 0.1 mM 3-CP recorded at a microcrystalline (A) and nanocrystalline (B) diamond thin-film electrode. An oxidation peak is observed during the forward scan at ca. 1.2 V, with only a weak corresponding reduction wave at ca.  $-0.20$  V. The anodic peak charge, after stabilization, was nominally  $26 \mu\text{C}$ . This oxidation peak is believed to be due to the 3-chlorophenoxy radical. Unlike the other four solutes, the oxidation peak currents decreases more rapidly with cycle number moreso for the nanocrystalline film, before reaching a pseudo-steady-state value. Contrary to the behavior of phenol, 2-CP, and 4-CP, no new oxidation or reduction peaks

develop at lower potentials. Apparently, the surface-confined electroactive quinones are not by-products of the oxidation reaction. For both 3-CP and PCP at microcrystalline and nanocrystalline diamond, the oxidation peak current (1.2 and 0.9 V, respectively) varied linearly with  $\nu$  from 0.05 to 0.25 V/s ( $r^2 > 0.990$ ) consistent with a surface-confined redox reaction.

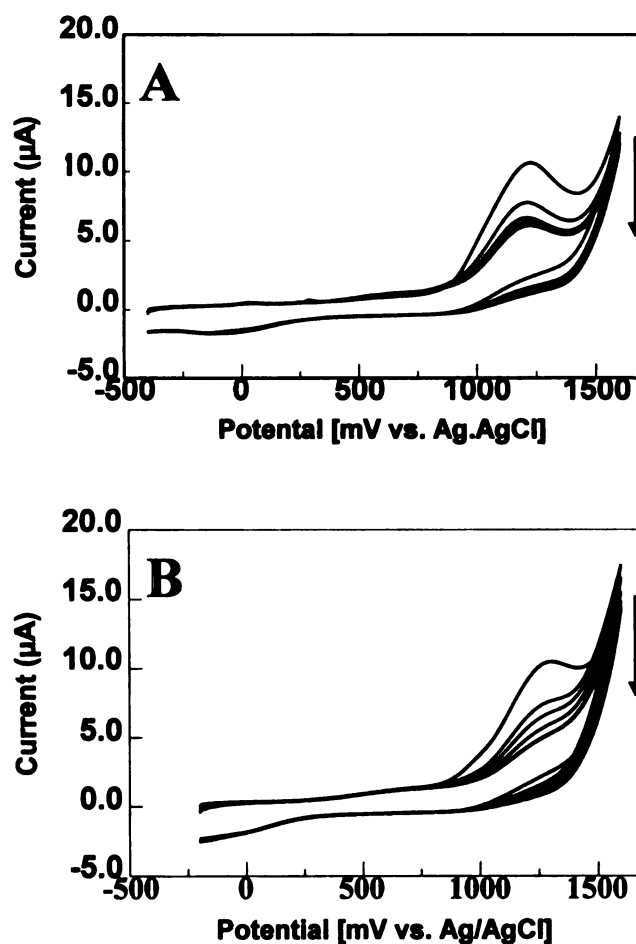


**Figure 4.8** Cyclic voltammetric i-E curves for 0.1 mM 3-CP at (A) microcrystalline and (B) nanocrystalline diamond electrodes in 0.05 M phosphate buffer, pH 3.5. Scan rate = 100 mV/s. Electrode geometric area = 0.2 cm<sup>2</sup>.

The 3-CP and PCP and/or their products adsorb on the electrode strongly than do other phenolic compounds studied as featureless background voltammogram was only observed if the passivated electrode was first cycled (ca. 10 scans) well into the oxygen evolution regime and then exposed to a fresh electrolyte solution. This suggests that the adsorbed products need to be oxidatively degraded by  $\text{OH}^\cdot$  in order to be removed from the surface.

The same cannot be said for GC, as similar agitation did not restore the original current. The trends in the shapes of the cyclic voltammograms for each of the phenolic compound with cycle number were the same for both GC and diamond. Figure 4.9 A shows five consecutive cyclic voltammograms for 0.1 mM 2-CP at freshly polished GC. A difference from diamond was the ca. 100 mV less positive oxidation peak for GC. The oxidation reaction products adsorb very strongly to the GC surface resulting in significant response deactivation. For example, GC was irreversibly fouled after five consecutive cycles in 2-CP and 3-CP. The oxidation peak current at 1.0 V decreased with cycle number and the original value could not be regained even with vigorous solution agitation or replacement with fresh electrolyte (see Figure 4.9 B). The current decreased by 36 %, and the oxidation peak was significantly shifted to the positive potentials. Polishing was the only means to remove all traces of the phenols.

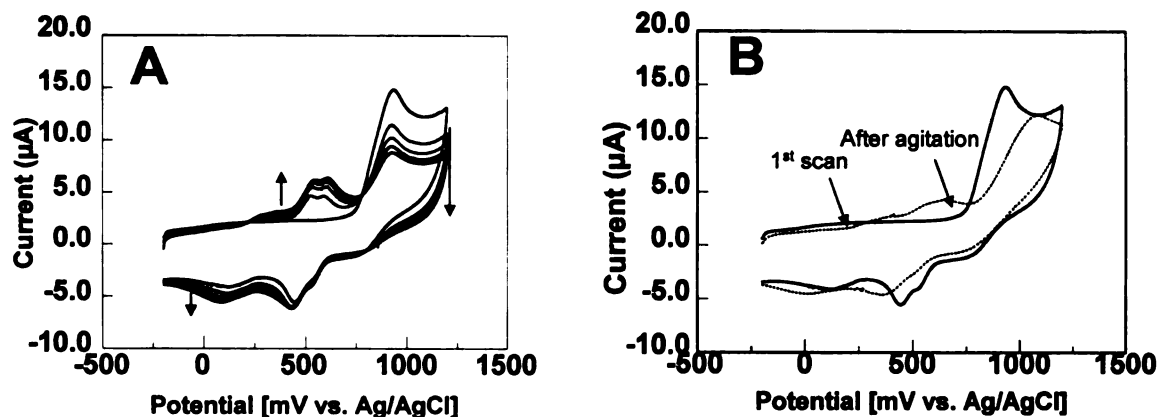


**Figure 4.9** Cyclic voltammetric  $i$ -E curves for 0.1 mM 2-CP at GC in 0.05 M phosphate buffer, pH 3.5, (A) and after solution agitation (B). Scan rate = 100 mV/s. Electrode geometric area = 0.2 cm<sup>2</sup>.

### 4.3. Conclusions

Cyclic voltammetric studies of phenol and chlorinated phenol oxidation were conducted using two types of diamond. The surface morphology and microstructure of each were different. The results revealed that (i) all five phenolic compounds can be electro-oxidized at both diamond types without electrode deactivation and fouling, as is the case for other electrodes like GC, (ii) the electro-oxidation reaction mechanism proceeds in a similar manner at both diamond types regardless of the differences in film morphology and microstructure, with phenol, 2-CP, and 4-CP yielding similar responses, (iii) the oxidation of phenol, 2-CP, and 4-CP leads to the formation of surface confined quinone/hydroquinone moieties, whereas the oxidation of 3-CP and PCP do not, and (iv) adsorbed reaction products were easily removed from the diamond surface by copiously rinsing with ultrapure water and exposure to fresh



electrolyte. In some cases, such as that for PCP, limited potential cycling was necessary to remove all traces of the reaction products.

#### 4.4. References

1. Gattrell, M.; Kirk, D.W.; *J. Electrochem. Soc.*, **1992**, *139*, 2736.
2. Gattrell, M.; Kirk, D.W.; *J. Electrochem. Soc.*, **1993**, *140*, 1534.
3. Belhadj Tahar, N.; Savall, A.; *J. Electrochem. Soc.*, **1998**, *145*, 3427.
4. Rodgers, J.D.; Jedral, W.; Bunce, N.; *J. Environ. Sci. Technol.*, **1999**, *33*, 1453.
5. Gattrell, M.; Kirk, D.W.; *J. Electrochem. Soc.*, **1993**, *140*, 903.
6. Mengoli, G.; Daolio, S.; Musiani, M.M.; *J. Appl. Electrochem* **1980**, *10*, 459.
7. Gattrell, M.; Kirk, D.W.; *Can. J. Chem. Eng.*, **1990**, *68*, 997.
8. Mengoli, G.; Musian, M.; *J. Electrochem. Soc.* **1987**, *134*, 643C.
9. Bruno, F.; Pham, M.C.; Dubois, J.E.; *Electrochim. Acta.*, **1977**, *22*, 451.
10. Fleischmann, M.; Hill, I.R. Mengoli, G.; Musian, M.M. *Electrochim. Acta.*, **1983**, *28*, 1545.
11. Gattrell, M.; MacDougall, B.; *J. Electrochem. Soc.* **1999**, *146*, 3335.
12. Iotov, P.I.; Kalcheva, S.V.; *J. Electrochem. Soc.* **1998**, *442*, 19.
13. Ezerskis, Z.; Jusys, Z.; *J. Appl. Electrochem.* **2002**, *32*, 543.
14. Lu, W.; Wallace, G.G.; Imisides, M.D.; *Electroanalysis*, **2002**, *14*, 325.
15. Terashima, C.; Rao, T.N.; Sarada, B.V.; Tryk, D.A.; Fujishima, A.; *Anal. Chem.* **2002**, *74*, 895.
16. Rondriego, M.A.; Michaud, P.A.; Duo, I.; Panizza, M.; Cerisola, G.; Ch. Comninellis, G.; *J. Electrochem. Soc.* **2001**, *148*, D60.
17. Hagans, P.L.; Natishan, P.M.; Stoner, B.R.; O'Grady, W.E. *J. Electrochem. Soc.* **2001**, *148*, E298.
18. Zhi, J.-F.; Wang, H.-B.; Nakashima, T.; Rao, T.N.; Fujishima, A.; *J. Phys. Chem.B* **2003**, *107*, 13389.
19. Prado, C.; Murcott, G.G.; Marken, F.; Foord, J.S.; Compton, R.G.; *Electroanalysis*, **2002**, *14*, 975.

20. Polcaro, A.M.; Vacca, A.; Palmas, S.; Mascia, M.J.; *J. Appl. Electrochem.* **2003**, *33*, 885.
21. Codognoto, L.; Machado, S.A.S.; Avaca, L.A.; *J. Appl. Electrochem.* **2003**, *33*, 951.
22. Canizares, P.; Garcia-Gomez, J.; Saez, C.; Rodrigo, M.A.; *J. Appl. Electrochem.* **2003**, *33*, 917.
23. Pletcher, D.; *A First Course in Electrode Processes*; Alresford Press: England, **1991**.
24. Kissinger, P.T.; Heineman, W.R.; *J. Chem. Ed.* **1983**, *60*, 702.
25. Wang, J.; *Analytical Electrochemistry*, 2nd ed.; Wiley: New York, 2000.
26. Runnels, P.L.; Joseph, J.D.; Logman, M.J.; Wightman, R.M. *Anal. Chem.* **1999**, *71*, 2782.
27. Duvall, S.H.; McCreery, R.L.; *J. Am. Chem. Soc.* **2000**, *122*, 6759.
28. Show, Y.; Witek, M.A.; Sonthalia, P.; Swain, G.M. *Chem. Mater.* **2003**, *15*, 879.

## **CHAPTER 5**

# **Detection of Chlorinated Phenols by Flow Injection Analysis and High Performance Liquid Chromatography with Amperometric Detection using a Boron-Doped Diamond Thin-Film Electrode**

### **5.1. Introduction**

Results presented in the previous Chapter showed that chlorinated phenols can be oxidized at boron-doped microcrystalline and nanocrystalline diamond thin film electrodes without significant deactivation or fouling.<sup>1-5</sup> The results presented vide infra further demonstrate the capability of this new electrode for the sensitive, reproducible and stable amperometric detection of these priority pollutants, when coupled with either flow injection analysis (FIA) and high performance liquid chromatography (HPLC).

In FIA, a liquid analyte sample is injected into the nonsegmented flowing carrier solution, propelled by a constant flow pump. The injected sample forms a

well-defined zone that is transported to the detector. The analyte concentration profile entering the detection cell depends upon the mode of the sample introduction, longitudinal diffusion, the flow parameters, and the geometry of the FIA channel situated between the sampling point and the detection site.<sup>6</sup> In one mode of operation, a detector continuously records a physical parameter, such as absorbance (fixed wavelength) or electrode current (fixed potential), and its change due to passage of an analyte zone. The output is a detector signal that varies with time and is used for quantitative analysis (peak height or area).<sup>7,8</sup> In FIA, the primary cause of zone (i.e., peak) broadening is longitudinal diffusion. The benefits of FIA include automated sample processing, high repeatability, short analysis time, adaptability to miniaturization, containment of chemicals, and waste reduction.<sup>9,10</sup> Liquid chromatography (LC) is a separation technique in which the solute is injected into a mobile phase and is transported through a column and to a detector. In HPLC (with a packed column), zone broadening arises from (i) eddy diffusion, (ii) longitudinal diffusion, and (iii) mass transfer within the stationary phase.

Several detection methods are normally coupled to FIA and HPLC, with electrochemical detection being one of the most common.<sup>7</sup> Electrochemical detection relies on a compound undergoing oxidation or reduction at an electrode to which a potential has been applied. The amperometric detection mode provides the advantage of minimizing the charging current by operating at a fixed potential, as opposed to voltammetric techniques in which the potential is

scanned with time. Several types of electrochemical cell designs have been used in FIA and HPLC with the most common being a thin-layer or cross flow type. In this design, the working electrode is positioned in a thin channel through which the carrier solution or mobile phase flows.<sup>11</sup> A schematic of the cell used in these studies was presented in Chapter 2. The cell design must give rise to a high S/N ratio, have low dead volume and well-defined hydrodynamic flow, minimal contribution to ohmic resistance, and be easy to construct and maintain.<sup>12</sup> With electrochemical detection, the mobile phase or carrier solution contain a supporting electrolyte. Oxidation or reduction reactions occur when a small volume of the solute flows past an electrode in the detection cell. Mass-transfer of the analyte to the electrode occurs by diffusion and also by convection due to the fluid flow. Therefore electrochemistry, in a flowing stream is referred to as a hydrodynamic technique. The enhanced rate of mass-transfer yields higher currents and higher S/N ratios.<sup>11,12</sup> The conversion efficiency, which is defined as the fraction of solute molecules entering the cell that are electrolyzed, is typically less than 5% in a thin-layer cell with a crossflow geometry.<sup>13</sup> The limiting current for a thin-layer flow cell is described by the equation,<sup>12</sup>

$$i_{lim} = 1.47nFC(DA/b)^{2/3}U^{1/3}$$

where  $i_{lim}$  is the limiting current (A),  $n$  is electron stoichiometry,  $F$  is the Faraday constant,  $C$  is concentration (mol/cm<sup>3</sup>),  $D$  is diffusion coefficient (cm<sup>2</sup>/s),  $A$  is electrode area (cm<sup>2</sup>),  $b$  is channel height (cm), and  $U$  is average volume flow rate (cm<sup>3</sup>/s).

FIA and HPLC coupled with amperometric detection (FIA-EC and HPLC-EC) were used to analyze for chlorinated phenols. Both microcrystalline and nanocrystalline electrodes were used for the oxidative detection of these pollutants. The objectives of the work were (i) to compare the performance of both diamond thin film types, (ii) to comprehensively evaluate the analytical detection figures of merit for both electrode types, and (iii) to demonstrate the capability of the method for the analysis of chlorinated phenols in a real sample. The electrode performance was evaluated in terms of the linear dynamic range, sensitivity, limit of quantitation, and response precision.

## **5.2. Results and Discussion**

### **5.2.1. Flow Injection Analysis with Electrochemical Detection**

Hydrodynamic voltammetric background *i*-*E* curves for microcrystalline diamond, nanocrystalline diamond, and freshly polished glassy carbon (GC) in 0.05 M phosphate buffer, pH 3.5, are shown in Figure 5.1. The mobile phase flow rate was 0.6 mL/min. The current was measured after 20 min at each potential and recorded. The curves were obtained by changing the applied potential in 50 mV increments beginning at 600 mV. The current magnitude and the peak-to-peak noise were recorded at the end of this period. The current for both diamond types is low and about the same magnitude over the entire potential range. The GC response, on the other hand, is much larger (factor of 5-10) at all potentials, especially positive of 1.2 V. As previously discussed in

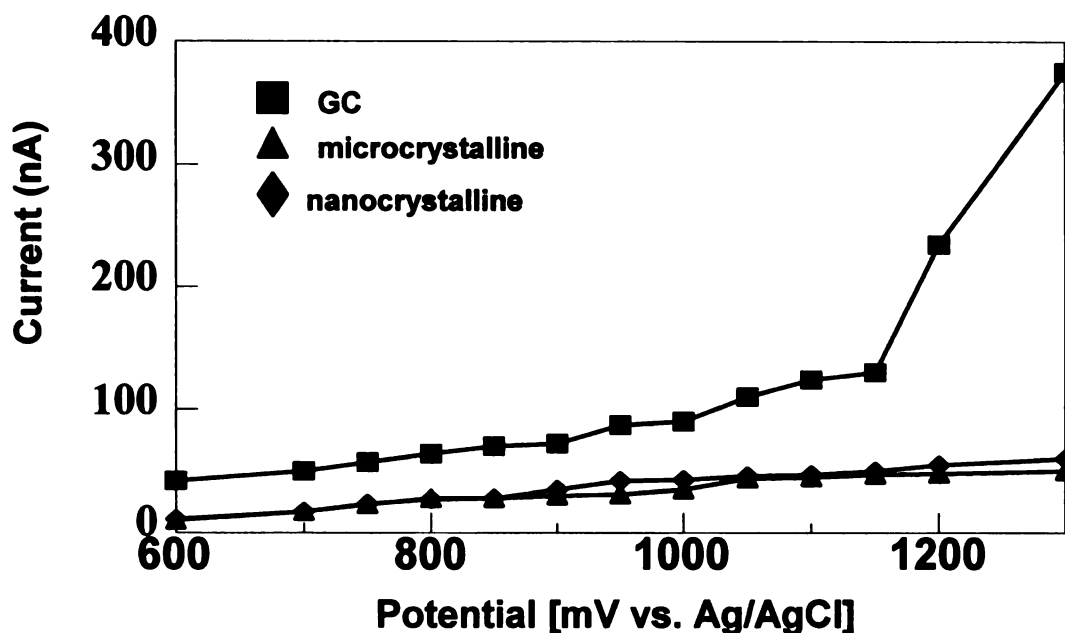


**Figure 5.1** FIA-EC hydrodynamic voltammetric background i-E curves for microcrystalline and nanocrystalline diamond, and GC in 0.05 M phosphate buffer, pH 3.5. Flow rate = 0.6 mL/min. Electrode geometric area = 0.11 cm<sup>2</sup>.

Chapter 4, the larger background for GC is due to the microstructural changes associated with the oxidation (i.e., formation of surface carbon-oxygen functionalities) at the edge plane and defect sites, which occurs over a wide potential range, as well as the onset of oxygen evolution.<sup>14</sup> One of the advantages of using diamond in amperometric detection is the low and stable background current and the large overpotential for oxygen evolution. Diamond is much more resistant to morphological and microstructural degradation than is GC. Therefore, the background current is much more stable over time at a given potential, particularly positive values. The background current for GC is also dynamic, progressively increasing with time due to the dynamic morphological

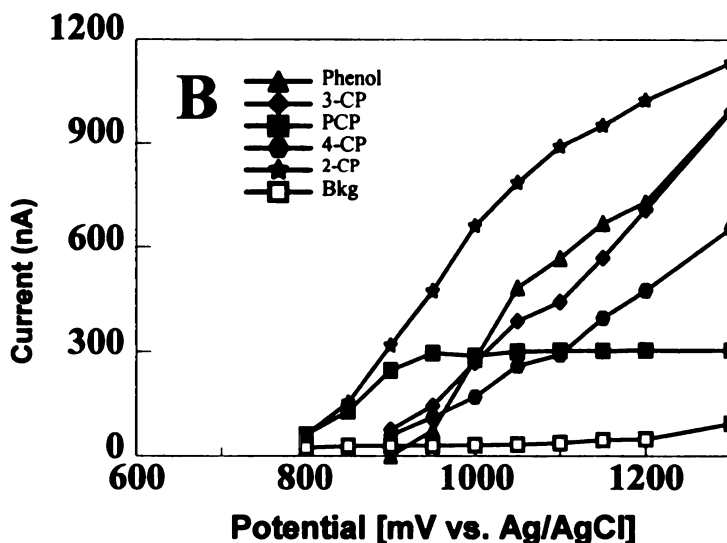
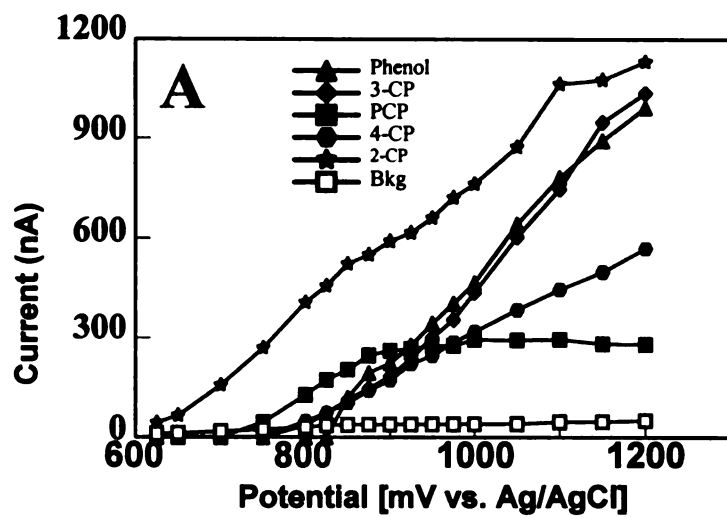


changes that occur at positive potentials. The oxidation causes an increase in the true electrode surface area, which consequently leads to an increase in current. On the other hand, the background current for diamond was very stable over time and reached a constant value soon after detector turn-on ( $E_{\text{appl}} = 1.1 \text{ V}$ ) within 5-10 min. The diamond surface is morphologically and microstructurally stable at anodic potentials so no dynamic oxidation processes or changes in surface structure. Surface oxidation does occur on diamond but is confined to a simple functional group exchange on the surface.<sup>15</sup> In contrast, the background current for GC often took 45-60 min to stabilize. A similar observation was reported by Terashima et al.<sup>2</sup> The rapid stabilization time is an advantageous property of diamond because it leads to a shorter overall analysis time.

Figure 5.2 shows hydrodynamic *i*-*E* curves for microcrystalline and nanocrystalline diamond thin-film electrodes during 20- $\mu\text{L}$  injections of 40  $\mu\text{M}$  phenolic solutions in 50 mM phosphate buffer, pH 3.5. The mobile phase flow rate was 0.6 mL/min. Each datum corresponds to the average response for 5 injections. The error bars were within the size of the marker and are not shown. The responses for phenol, 2-CP, 3-CP, and 4-CP do not exhibit a well-defined sigmoidal shape (i.e., limiting current) - a shape expected if the reaction rates is limited exclusively by mass transfer at an electrode with well-defined area. The only sigmoidally-shaped curve is the one for PCP. These observations are different from those of Terashima et al. as they reported sigmoidally-shaped hydrodynamic voltammograms for several di- and trichlorophenols.<sup>2</sup> It is

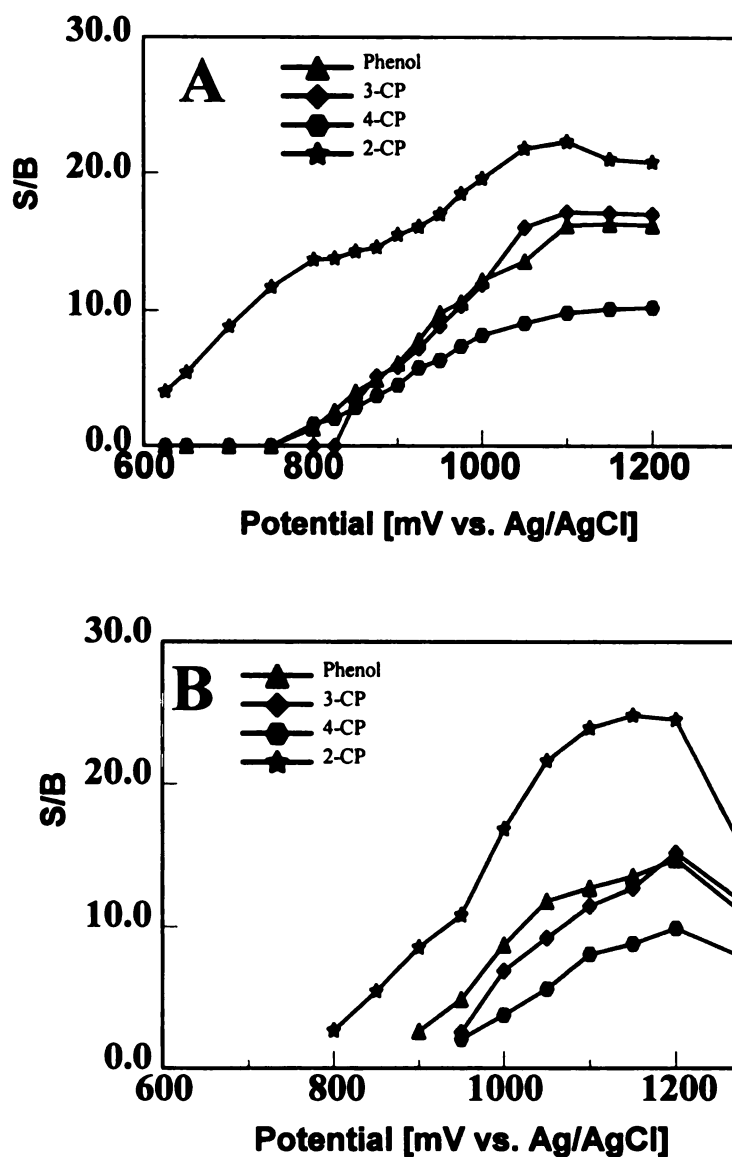
supposed that the maximum oxidation current for phenol, 2-CP, 3-CP, and 4-CP in the potential region positive of 800 mV is under mixed control by direct and indirect electro-oxidation reaction rates as well as mass transfer. As mentioned in Chapter 4, the electro-oxidation of these phenols involves the initial formation of a phenoxy radical species. This is followed by either radical-radical coupling to form polymeric products, or direct and indirect ( $\text{OH}\cdot$  generation) oxidation reactions to form quinone-like products.<sup>1-4,16-21</sup> The maximum current in the hydrodynamic curves varied depending on the phenolic compound with the largest magnitude observed for 2-CP at both electrodes.

Figure 5.3 show plots of the signal-to-background  $(S/B)(I_{\text{tot}} - I_{\text{bkg}}/I_{\text{bkg}})$  ratio as a function of the applied potential for the phenol, 2-chlorophenol, 3-chlorophenol and 4-chlorophenol. Such plots are useful for determining the optimum detection potential when sigmoidal hydrodynamic voltammograms are not observed. The optimum detection potential for the analytes is in the 1100-1200 mV range for both diamond types. A sharp decrease in S/B for the nanocrystalline diamond is observed at potentials positive of 1200 mV. This is due to the onset of oxygen evolution, which occurs at a slightly less positive potential than for microcrystalline diamond. The most negative onset potential for the oxidation and the largest current response is observed for 2-CP. Irrespective of the order of injection, the largest S/B is seen for 2-CP at both electrode types. S/B plot for the PCP is not presented because it exhibited a well-defined sigmoidal current response.



**Figure 5.2** Hydrodynamic voltammetric i-E curves for 40  $\mu\text{M}$  concentrations of each phenolic compound in 50 mM phosphate buffer, pH 3.5, at a (A) microcrystalline and (B) nanocrystalline diamond thin-film electrode. Flow rate = 0.6 mL/min. Each datum represents the average of 5 injections.

In order to evaluate the effectiveness of diamond for phenol and chlorinated phenols analysis, the analytical detection figures of merit (e.g., linear dynamic range, sensitivity, limit of quantitation (LOQ), and response precision)



**Figure 5.3** S/B vs potential plots for 40  $\mu\text{M}$  concentrations of each phenolic compound in 50 mM phosphate buffer, pH 3.5, at a (A) microcrystalline and (B) nanocrystalline diamond thin-film electrode. Flow rate = 0.6 mL/min. Injected volume = 20  $\mu\text{L}$ . Each datum represents the average of 5 injections.

were determined for both diamond thin film types. GC was also used for comparison. A calibration curve for each analyte was obtained in 50 mM phosphate buffer, pH 3.5, as a function of the injected concentration. Plots of the peak height versus the concentration are shown in Figure 5.4 for microcrystalline diamond. Similar calibration curves were obtained for nanocrystalline diamond (not shown). The injected volume was 20  $\mu$ L and the flow rate was 0.6 mL/min. The data presented are average for at least three electrodes. Detection was made at 1.1 V for microcrystalline and 1.2 V for nanocrystalline diamond. The linear dynamic range, LOQ, and the sensitivity for the phenol and chlorinated phenols both electrode types are summarized in Tables 5.1 and 5.2. The linear dynamic range for all the analytes at both diamond types is 4 – 5 orders of magnitude ( $r^2 > 0.990$ ) from the nanomolar to micromolar range. Overall, slightly higher sensitivities were observed for nanocrystalline diamond by a factor of 1.3 – 1.5 at least for some analytes. The sensitivities for all analytes, except for PCP, are approximately the same for a given diamond type with the value for PCP being about a factor of 3 lower. The lower sensitivity for PCP, as compared to other analytes, could be due to a lower number of electrons transferred in the overall electrochemical reaction. The data for only one electrode type, shown in Figure 5.3, reveal a sizable difference in the maximum response for each of the compounds. However, we observed this to be the exception rather than the rule. The more common observation is reflected in the sensitivity data in Tables 5.1 and 5.2. The minimum concentration detected (LOQ) for each analyte is also similar for both diamond types. The mass limit of quantitation is in the high pg to

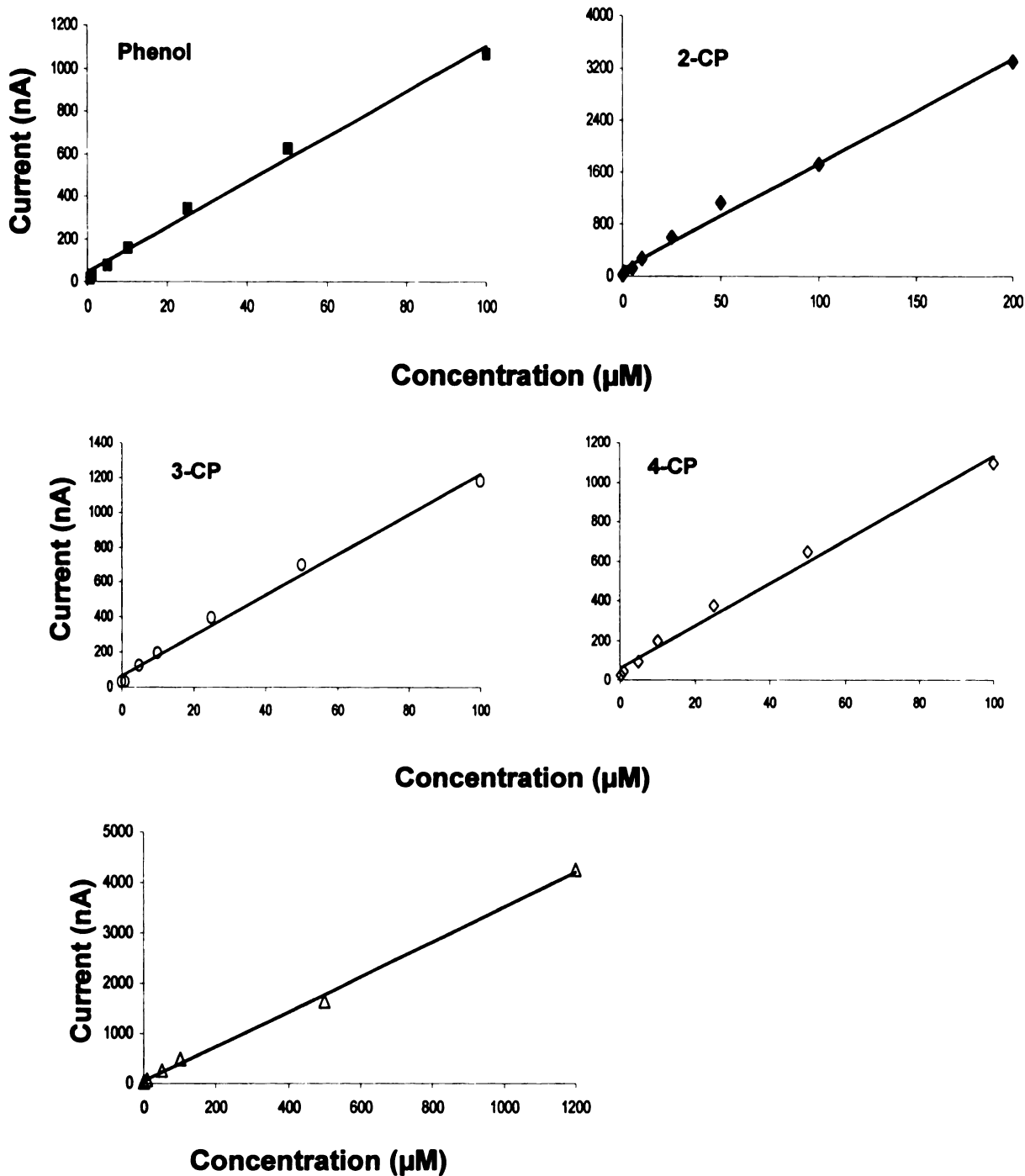


**Figure 5.4** Calibration curves for the phenol and chlorinated phenols obtained for microcrystalline diamond. The carrier solution was 50 mM phosphate buffer, pH 3.5. Flow rate = 0.6 mL/min. Injected volume = 20 μL. Electrode geometric area = 0.11 cm<sup>2</sup>. Detection potential = 1.1 V.

**Table 5.1 FIA-EC Data for Phenol and Chlorinated Phenols at Microcrystalline Diamond Thin-Film Electrode**

Analyte	Linear Dynamic Range ( $\mu\text{M}$ )	Sensitivity ( $\text{nA}/\mu\text{M}$ )	LOQ <sup>a</sup> ( $\mu\text{M}$ )	LOQ (ng)
phenol	0.3 – 100 $r^2 = 0.9903$	$9.9 \pm 1.2$	0.3 (S/N =7) (28 ppb)	0.77
2-CP	0.05 - 200 $r^2 = 0.9923$	$14.2 \pm 0.5$	0.05 (S/N = 6) (6 ppb)	0.13
3-CP	0.1 – 100 $r^2 = 0.9902$	$10.0 \pm 2.2$	0.1 (S/N =7) (13 ppb)	0.26
4-CP	0.5 – 100 $r^2 = 0.9928$	$11.0 \pm 1.3$	0.5 (S/N = 4) (64 ppb)	1.28
PCP	0.6 – 1200 $r^2 = 0.9980$	$3.4 \pm 0.1$	0.6 (S/N = 6) (160 ppb)	3.19

**Table 5.2 FIA-EC Data for Phenol and Chlorinated Phenols at Nanocrystalline Diamond Thin-Film Electrode**

Analyte	Linear Dynamic Range ( $\mu\text{M}$ )	Sensitivity ( $\text{nA}/\mu\text{M}$ )	LOQ <sup>a</sup> ( $\mu\text{M}$ )	LOQ (ng)
phenol	0.3 – 100 $r^2 = 0.9958$	$18.4 \pm 1.3$	0.3 (S/N =8) (28 ppb)	0.77
2-CP	0.05 - 200 $r^2 = 0.9946$	$17.9 \pm 1.8$	0.05 (S/N = 7) (6 ppb)	0.13
3-CP	0.1 – 100 $r^2 = 0.9977$	$18.8 \pm 1.4$	0.1 (S/N =7) (13 ppb)	0.26
4-CP	0.5 – 100 $r^2 = 0.9964$	$16.4 \pm 1.5$	0.5 (S/N = 6) (64 ppb)	1.28
PCP	0.6 – 1200 $r^2 = 0.9979$	$6.9 \pm 1.9$	0.6 (S/N = 6) (160 ppb)	3.19

<sup>a</sup> limit of quantitation = lowest concentration injected and detected.

Note: The data are reported for 3 electrodes for each diamond type. Carrier solution = 50 mM phosphate buffer, pH 3.5. Injection volume = 20  $\mu\text{L}$ . Flow rate = 0.6 mL/min. Electrode geometric area = 0.11  $\text{cm}^2$ . The detection potential was 1.1 and 1.2 for microcrystalline and nanocrystalline diamond, respectively.

low ng range ( $S/N \geq 3$ ). By way of comparison, a reduced linear dynamic range, a higher limit of detection, and greater response variability were observed for GC.

The response precision was evaluated over twenty consecutive 20- $\mu$ L injections of 40  $\mu$ M analyte at 1-min intervals. Both diamond types exhibit good response precision for these analytes without significant electrode deactivation. For example, Figure 5.5 shows the response for multiple injections of 2-CP at a microcrystalline film. A summary of the response precision for all the analytes at both diamond types and GC is presented in Table 5.3. The data represents an average of three runs on each electrode type. The RSD values range from 1.9 to 5.7% for microcrystalline diamond, 1.4 to 3.9% for nanocrystalline diamond, and 4.6 to 20.7% for GC. The good response precision for diamond is due to the excellent morphological and microstructural stability of the material. In contrast, the response precision was poor for GC due to the morphological and microstructural instability and deactivation by reaction intermediates and products. Figure 5.6 shows multiple injections of phenol, 2-CP, 3-CP, 4-CP and PCP on GC. The current response for the analytes decreases with time more so for phenol and 3-CP. On GC, the edge plane carbon atoms are terminated by oxygen functionalities, making the surface polar and hydrophilic. Strong adsorption occurs near these sites probably due to  $\pi$ - $\pi$ , dipole-dipole and/or ion-dipole interactions between the polar surface and the solute.



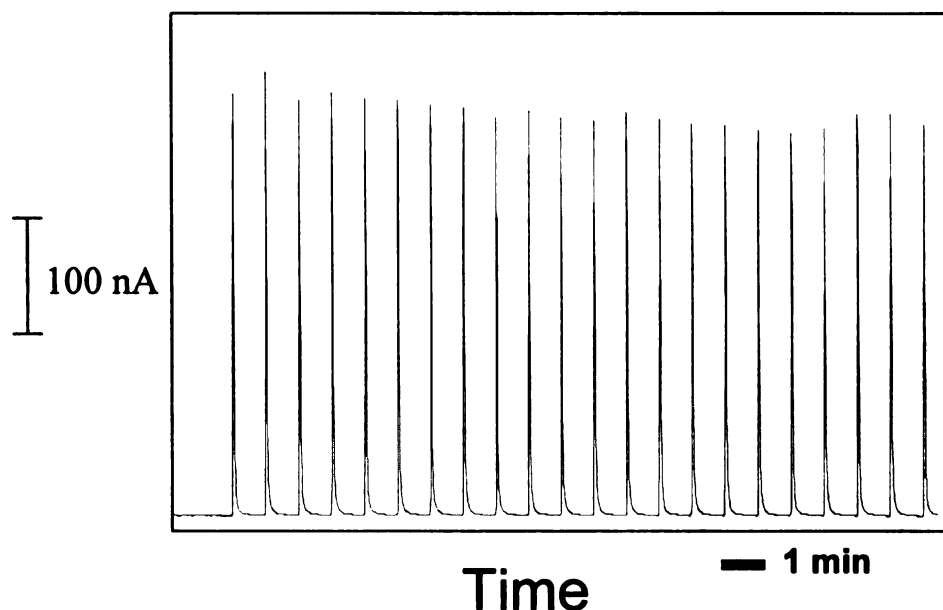


**Figure 5.5** FIA-EC response for multiple injections of 40  $\mu\text{M}$  2-CP. The carrier solution was 50 mM phosphate buffer, pH 3.5. Detection potential = 1.2 V. Injection volume = 20  $\mu\text{L}$ . Flow rate = 0.6 mL/min.

**Table 5.3 Response Precision Data for Phenol and Chlorinated Phenols for Microcrystalline and Nanocrystalline diamond, and GC.**

Analyte	Microcrystalline RSD%	Nanocrystalline RSD%	GC RSD%
Phenol	4.1	3.9	7.7
2-chlorophenol	1.9	1.4	4.6
3-chlorophenol	5.6	2.2	20.7
4-chlorophenol	1.7	2.2	6.1
Pentachlorophenol	1.6	2.6	6.5

Note: The response precision was evaluated from 20 consecutive injections at 1-min intervals. The data are reported as a mean for 3 measurements. Carrier solution = 50 mM phosphate buffer, pH 3.5. Analyte concentration = 40  $\mu\text{M}$ . Injection volume = 20  $\mu\text{L}$ . Flow rate = 0.6 mL/min. Electrode geometric area = 0.11  $\text{cm}^2$ . The detection potential was 1.1, 1.2 and 1.0 V for microcrystalline diamond, nanocrystalline diamond, and GC, respectively.

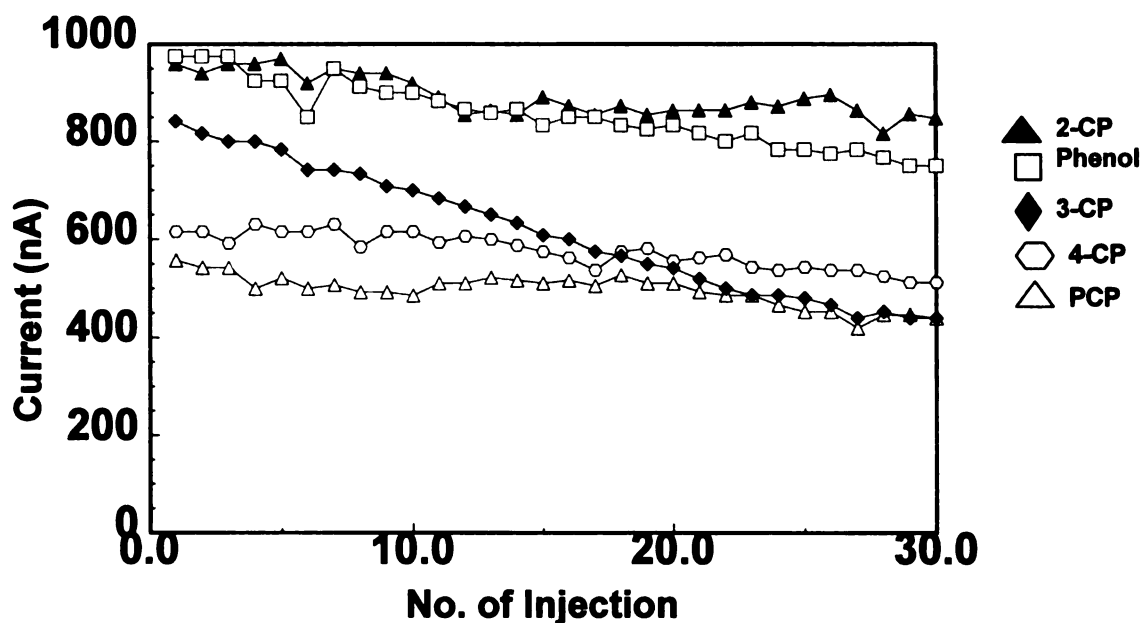


**Figure 5.6** FIA-EC responses for multiple injections of 40  $\mu\text{M}$  phenol, 2-CP, 3-CP, 4-CP, and PCP on GC. The carrier solution was 50 mM phosphate buffer, pH 3.5. Detection potential = 1.0 V. Injection volume = 20  $\mu\text{L}$ . Flow rate = 0.6 mL/min.

### 5.2.2. High Performance Liquid Chromatography with Electrochemical Detection

Reversed-phase HPLC separation with electrochemical detection was used to analyze solutions containing phenol and chlorinated phenols. Significant optimization was performed initially to develop a satisfactory isocratic separation of these solutes with maximum efficiency. In the isocratic elution, the retention time of the least polar solute (PCP) was quite long (> 30 min), therefore a step was employed in the elution procedure. A 50 mM phosphate buffer/acetonitrile, pH 3.5, 65:35 (v/v) mobile phase was used to separate phenol, 2-CP, 3-CP, and

4-CP. The mobile phase was then switched to a 20:80 (v/v) composition in order to elute the last analyte (PCP). Peak assignments were made based on retention time matching of the individually injected solutes.

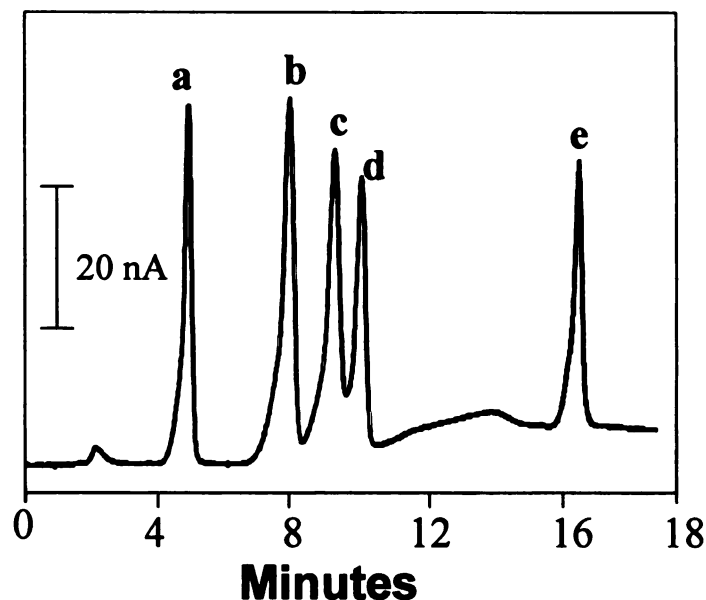
Isocratic elution is usually the separation method of choice with electrochemical detection because gradient elution or often causes drifting baseline currents and long stabilization times for many electrode materials. Both diamond types exhibited low and stable background currents in the mixed mobile phase system, even at high positive potentials. The background current for diamond at 1.1 or 1.2 V was low at about 5 - 8 nA and increased only slightly with an increase in the organic modifier content. The peak-to-peak noise was ca. 200 pA. Rapid stabilization was observed for both diamond types after detector turn on in this mobile phase.

Figure 5.7 shows a typical chromatogram for the five phenols detected amperometrically using a microcrystalline diamond electrode. A similar chromatogram was observed for a nanocrystalline diamond. The expected reversed-phase elution order, based on the solute polarity, was observed. Phenol, being the most polar solute elutes first, whereas PCP, being the least polar molecule, elutes last. The separation is complete in about 16 min and the peaks are fronting slightly. The fronting worsened with prolonged column use. Typically, no fronting was seen with a new column. This is presumably because

of stationary phase degradation which creates exposed silanol sites that can interact strongly with the phenols leading to a secondary retention mechanism.

A comprehensive set of detection figures of merit for phenol and the chlorinated phenols was obtained for both nanocrystalline and microcrystalline diamond. Calibration curves for all the solutes are shown in Figure 5.8 for (A) microcrystalline and (B) nanocrystalline thin film. The detection figures of merit are summarized in Table 5.5 and 5.6. The linear dynamic range for all the solutes is at least 2-3 orders of magnitude ( $r^2 > 0.99$ ). It should be emphasized that the maximum concentration of 80  $\mu\text{M}$  does not represent the upper limit of the dynamic range but just simply the maximum solute concentration used in this work. The response sensitivity is approximately the same for both electrode types, but lower in the mixed aqueous/organic solution than they are in the pure aqueous medium. Both diamond types exhibited good run-to-run response reproducibility with no evidence of electrode deactivation or fouling. The response precision (2 - 6%) is identical for both electrode types and was determined from repetitive injections of a 20  $\mu\text{M}$  analyte concentration. The concentration limit of quantitation was in the low to mid ppb range and corresponds to a mass limit of quantitation ranging from 0.1 to 0.5 ng ( $S/N \geq 3$ ). In general, the detection figures of merit for the microcrystalline and nanocrystalline diamond films compare favorably with those previously reported for an oxygen-terminated diamond electrode<sup>2,22</sup> and are somewhat improved over those reported for other electrodes.<sup>23-25</sup> In addition, the limits of quantitation for

the phenolic solutes in our HPLC-EC method are comparable to those reported for EPA Method 1625.<sup>26</sup>



**Figure 5.7** Reversed-phase chromatogram for phenol and the chlorinated phenols detected with amperometric detection using a microcrystalline diamond thin-film electrode. The concentration of each solute was 20  $\mu\text{M}$ . Injection volume = 20  $\mu\text{L}$ . Detection potential = 1150 mV vs. Ag/AgCl. Flow rate = 0.6 mL/min.  $\text{C}_{18}$  column (X-Terra, 5  $\mu\text{m}$  particle size, 4.6 mm x 150 mm). The compounds are (a) phenol, (b) 2-CP, (c) 3-CP, (d) 4-CP, and (e) PCP. A two-step gradient elution was used. Initially, a 50 mM phosphate buffer, pH 3.5/acetonitrile (65:35, v/v) was used and was switched to a 20:80 mixture after 10 min. Electrode geometric area = 0.11  $\text{cm}^2$ .

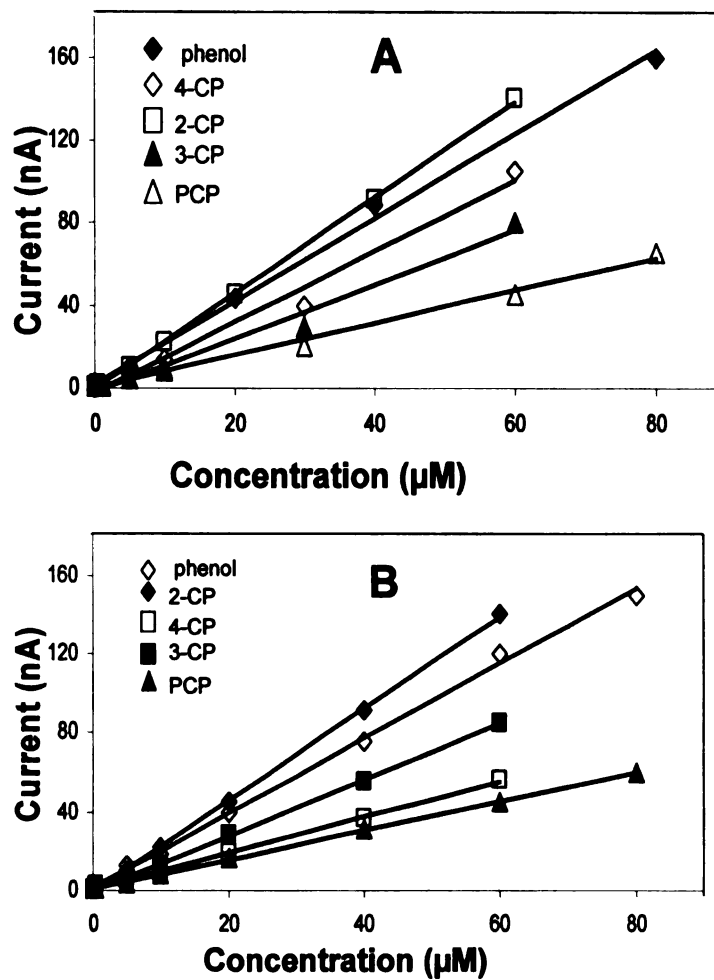


**Figure 5.8** Calibration curves for phenol and chlorinated phenols at a (A) microcrystalline and (B) nanocrystalline diamond thin-film electrode. The separation was performed using the same conditions as in Figure 5.6. The detection potentials used were 1100 and 1200 mV vs. Ag/AgCl for A and B, respectively. Injection volume = 20 µL. Electrode geometric area = 0.11 cm<sup>2</sup>.

**Table 5.4 HPLC-EC Detection Figures of Merit for Phenol and the Chlorinated Phenols at a Microcrystalline Diamond Thin-Film Electrode**

Analyte	Linear Dynamic Range ( $\mu\text{M}$ )	Sensitivity ( $\text{nA}/\mu\text{M}$ )	Response Precision ( $n = 7$ )	LOQ <sup>a</sup> ( $\mu\text{M}$ )	LOQ (ng)
phenol	0.1 – 80 $r^2 = 0.9983$	$1.9 \pm 0.1$	3.8	0.1 (S/N = 4) (9 ppb)	0.19
2-CP	0.1 - 60 $r^2 = 0.9994$	$2.0 \pm 0.4$	3.2	0.1 (S/N = 9) (13 ppb)	0.26
3-CP	0.1 – 60 $r^2 = 0.9991$	$1.0 \pm 0.2$	2.9	0.1 (S/N = 4) (13 ppb)	0.26
4-CP	0.1 – 60 $r^2 = 0.9984$	$1.4 \pm 0.3$	4.4	0.1(S/N = 4) (13 ppb)	0.26
PCP	0.1 – 80 $r^2 = 0.9902$	$0.9 \pm 0.1$	3.8	0.1(S/N = 6) (27 ppb)	0.53

**Table 5.5 HPLC-EC Detection Figures of Merit for Phenol and the Chlorinated Phenols at a Nanocrystalline Diamond Thin-Film Electrode**

Analyte	Linear Dynamic Range ( $\mu\text{M}$ )	Sensitivity ( $\text{nA}/\mu\text{M}$ )	Response Precision ( $n = 7$ )	LOQ <sup>a</sup> ( $\mu\text{M}$ )	LOQ (ng)
phenol	0.1 – 80 $r^2 = 0.9974$	$2.0 \pm 0.5$	5.2	0.1(S/N = 4) (9 ppb)	0.19
2-CP	0.1 - 60 $r^2 = 0.9946$	$2.3 \pm 0.4$	4.1	0.1(S/N = 10) (13 ppb)	0.26
3-CP	0.1 – 60 $r^2 = 0.9930$	$1.0 \pm 0.2$	3.2	0.1(S/N = 4) (13 ppb)	0.26
4-CP	0.1 – 60 $r^2 = 0.9990$	$1.4 \pm 0.3$	5.1	0.1(S/N = 5) (13 ppb)	0.26
PCP	0.1 – 80 $r^2 = 0.9984$	$1.0 \pm 0.1$	5.6	0.1(S/N = 6) (27 ppb)	0.53

<sup>a</sup>limit of quantitation = lowest concentration injected and detected.

Note: The data are reported for 3 electrodes. Experimental conditions as in Figure 5.6. The detection potential was 1.1 and 1.2 V for microcrystalline and nanocrystalline films, respectively.

### **5.2.3. Soil Sample Analysis**

The utility of the HPLC-EC method for the analysis of chlorinated phenols in a soil sample was demonstrated. A 10 g soil sample containing at least 60 different organic pollutants was obtained from Absolute Standards, Inc (Hamden, CT). The sample was prepared according to principles outlined in the "National Standard for Water Proficiency Testing Studies, Criteria Document" – EPA 12/30/98. The sample came with a list of concentration ranges for each pollutant present. No information was provided about the mineralogy of the soil or how the sample was prepared. 2-chlorophenol (2-CP) was one of the electroactive contaminants present and, therefore, the soil was analyzed for it. The sample was prepared for analysis in the following manner. First, all 10 g of the soil sample was added to 40.0 mL of acetonitrile and ultrasonically mixed for 30 min. This served to extract 2-CP into the liquid phase. Second, the sonicated sample was then centrifuged for 30 min, and the liquid phase was carefully decanted into a 250 mL round bottom flask. Third, the solvent was evaporated on a rotatory flash evaporator down to a volume of 8 – 10 mL. The sample was again centrifuged and the extract designated as the crude sample. Fourth, solid phase extraction was carried out using a 3 mL SuperClean LC-18 cartridges (Supelco, 491 m<sup>2</sup>/g). The C-18 cartridges were conditioned with 6.0 mL of methanol followed by 6.0 mL of ultrapure water. After conditioning, 2.0 mL of the crude sample was mixed with 4.0 mL of ultrapure water in a clean vial. The sample was passed through the solid phase (vacuum-assisted) - a process that took approximately 10 min. The sample was finally eluted off the solid phase with 6.0



mL of a solvent mixture containing dichloromethane, hexane, and acetonitrile (50:47:3 v/v). The solvent was evaporated by passing N<sub>2</sub> down to a final volume of ca. 1.0 mL. The concentrated sample was then adjusted to 4.0 mL with the addition of the mobile phase solution (65:35 (v/v), 50 mM phosphate buffer, pH 3.5/acetonitrile). This sample was then injected onto the HPLC column for separation and detection.

Figure 5.9 shows a chromatogram for the sample extract. Amperometric detection was accomplished at 1.1 V using a microcrystalline diamond electrode. Elution was performed using the two-step gradient. A 65:35 50 mM phosphate buffer, pH 3.5/acetonitrile mobile phase was used initially to elute the more polar analytes, and this composition was adjusted to 20:80 at ca. 10 min mark to elute the more nonpolar solutes. The chromatogram reveals the presence of 21 different peaks, each of which corresponds presumably to an electroactive solute. No efforts were made to identify the solutes. Most importantly for this work, 2-CP elutes at 6.2 min and is labeled on the chromatogram. Peak identification was performed by retention time matching. The peak represents the raw signal for the unknown concentration of 2-CP in the soil sample. A standard calibration curve was generated between 0.1 to 80  $\mu$ M for quantitation of 2-CP. A linear response was observed with a regression correlation coefficient of 0.9963. Standard addition is the method of choice for quantifying 2-CP in this complex matrix, but we did not have enough of the soil to conduct this type of calibration. Based on the calibration curves generated from a series of standard solutions,

the concentration of 2-CP in the soil was determined to be 2650  $\mu\text{g}$  (2-CP)/kg (soil). The supplier of the contaminated soil sample specified a low and high acceptance value of 2643 and 5983  $\mu\text{g}/\text{kg}$ , and an assigned value of 4313  $\mu\text{g}/\text{kg}$  for 2-CP. The experimentally determined value is lower than assigned value and is on the low end of the acceptance range. However, given that specific details regarding the sample preparation and the length of time the sample was stored were not readily available and the presumption that 100% recovery was achieved, we suppose the experimentally determined value reflects the true value of the 2-CP present.

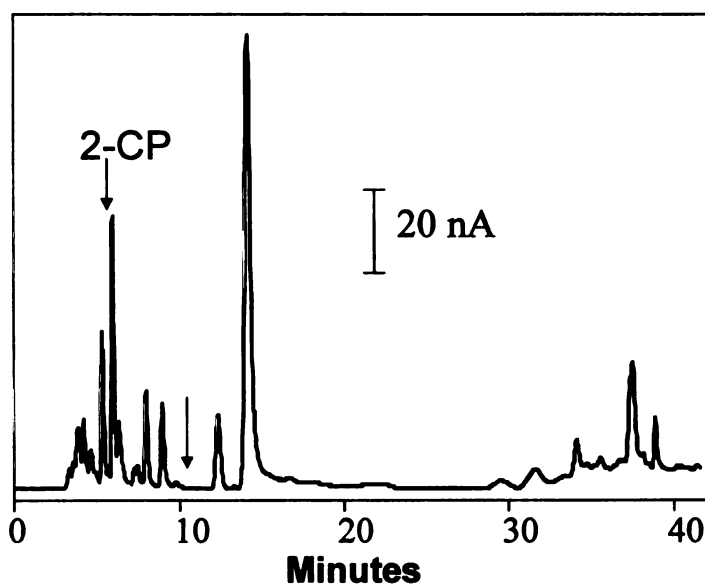


**Figure 5.9** Reversed-phase chromatogram for the separation and amperometric detection of 2-CP in a contaminated soil sample at a microcrystalline diamond thin-film electrode. Injection volume = 20  $\mu\text{L}$ . Detection potential = 1150 mV vs. Ag/AgCl. Flow rate = 0.6 mL/min.  $\text{C}_{18}$  column (X-Terra, 5  $\mu\text{m}$  particle size, 4.6 mm x 150 mm). A two-step elution was used. Initially, a 65:35 (v/v) 50 mM phosphate buffer, pH 3.5/acetonitrile was used and was switched to a 20:80 mixture at the 10 min mark. Electrode geometric area = 0.11  $\text{cm}^2$ .

### **5.3. Conclusions**

Electrically conducting microcrystalline and nanocrystalline diamond thin-film electrodes show promise for the amperometric detection of chlorinated phenols, in either flow injection analysis (FIA) or high performance liquid chromatography (HPLC). Their low background current, good performance for phenol oxidation, and low susceptibility to fouling make them useful for phenol and chlorinated phenol analysis in water samples. Both types of diamond outperformed GC, which exhibited short-lived activity as a consequence of electrode deactivation. For example, the relative standard deviation of the peak height for 20 injections of 3-CP was 2.2% for nanocrystalline diamond and 20.7% for glassy carbon. Low limits of quantitation were observed for both diamond types for all the phenols. For example, a limit of quantitation of 50 nM or 6 ppb (20- $\mu$ L inj.) was achieved for 2-chlorophenol with both diamond types in FIA-EC. When coupled to HPLC, both diamond types gave good detection figures of merit for all the chlorinated phenols. For example, the limit of quantitation for all the analytes was 0.1  $\mu$ M. The preliminary result for the soil sample illustrates the potential for using this method to monitor phenol and chlorinated phenols in real samples.

## 5.4. References

1. Muna, G.W.; Tasheva, N.; Swain, G.M.; *Environ. Sci. Technol.* **2004**, *38*, 3674.
2. Terashima, C.; Rao, T.N.; Sarada, B.V.; Tryk, D.A.; Fujishima, A.; *Anal. Chem.* **2002**, *74*, 895.
3. Rondrigo, M.A.; Michaud, P.A.; Duo, I.; Panizza, M.; Cerisola, G.; Ch. Comninellis, G.; *J. Electrochem. Soc.* **2001**, *148*, D60.
4. Hagans, P.L.; Natishan, P.M.; Stoner, B.R.; O'Grady, W.E. *J. Electrochem. Soc.* **2001**, *148*, E298.
5. Zhi, J.-F.; Wang, H.-B.; Nakashima, T.; Rao, T.N.; Fujishima, A.; *J. Phys. Chem.B* **2003**, *107*, 13389.
6. Toth, K.; Stulik, K.; Wlodzimierz, K.; Zsofia, F.; Erno, L.; *Pure Appl. Chem.* **2004**, *76*, 1119.
7. Ruzicka, J.; Hansen, E.H. *Flow Injection Analysis*, 2nd ed.; J. Wiley: New York, 1988.
8. Hansen, E.H.; Ruzicka, J. *J. Chem. Ed.* **1979**, *56*, 677.
9. Ruzicka, J.; Hansen, E.H. *Anal. Chem.* **2000**, *72*, 212A.
10. In <http://www.lachatstruments.com/products/qcfia/FIAPrimer.asp>., accessed April **2005**.
11. LaCourse, W.R.; *Pulsed Electrochemical Detection in High Performance Liquid Chromatography*, **1997**.
12. Wang, J.; *Analytical Electrochemistry*, 2nd ed.; Wiley: New York, **2000**.
13. Dryhurst, G.; *NATO ASI Ser., Ser. A* **1994**, *267*, 171.
14. Jolley, S.; Koppang, M.; Jackson, T.; Swain, G.M. *Anal. Chem.* **1997**, *69*, 4099.
15. Granger, M.C.; Witek, M.; Xu, J.; Wang, J.; Hupert, M.; Hanks, A.; Koppang, M.D.; Butler, J.E.; Lucazeau, G.; Mermoux, M.; Strojek, J.W.; Swain, G.M. *Anal. Chem.* **2000**, *72*, 3793.

16. Gattrell, M.; Kirk, D.W.; *J. Electrochem. Soc.*, **1993**, *140*, 1534.
17. Gattrell, M.; Kirk, D.W.; *J. Electrochem. Soc.*, **1993**, *140*, 903.
18. Polcaro, A.M.; Vacca, A.; Palmas, S.; Mascia, M.; *J. Appl. Electrochem.* **2003**, *33*, 885.
19. Codognoto, L.; Machado, S.A.S.; Avaca, L.A.; *J. Appl. Electrochem.* **2003**, *33*, 951.
20. Canizares, P.; Garcia-Gomez, J.; Saez, C.; Rodrigo, M.A. *J. Appl. Electrochem*, **2003**, *33*, 917.
21. Zhi, J.-F.; Wang, H.-B.; Nakashima, T.; Rao, T.N.; Fujishima, A.; *J. Phys. Chem.B* **2003**, *107*, 13389.
22. Prado, C.; Murcott, G.G.; Marken, F.; Foord, J.S.; Compton, R.; *Electroanalysis* **2002**, *14*, 975.
23. Agui, L.; Serra, B.; Yanez-Sedeno, P.; Reviejo, A.; Pingarron, J.M.; *Electroanalysis* **2001**, *13*, 1231.
24. Liu, X.; Frank, H.; *J. High Resol. Chromatogr.* **1998**, *21*, 309.
25. Dressman, S.F.; Simeone, A.M.; Michael, A.C.; *Anal. Chem.* **1996**, *68*, 3121.
26. **Standard Methods for the Examination of Water and Wastewater, 18<sup>th</sup> Edition, US Environmental Protection Agency, 1992**

## **CHAPTER 6**

# **Chlorinated Phenol Analysis by Capillary Zone Electrophoresis with Amperometric Detection using a Diamond Microelectrode**

### **6.1. Introduction**

Capillary zone electrophoresis (CZE) is a powerful separation method for a variety of analytes, offering the advantages of high separation efficiency, short analysis time, and low reagent consumption.<sup>1,2</sup> Separation is based on the differential rates of migration of charged solutes in an applied electric field. Small inorganic ions and organic species, as well as large biomolecules such as DNA and proteins, can be separated by this method. During the past two decades, great attention has been given to different electrophoretic methods in which the separation occurs in a small bore capillary. In capillary zone electrophoresis (CZE), separation is performed in a solvent-filled glass or fused-silica capillary tube across which a high voltage (e.g., 20 kV) is applied. Solute are transported across the column by two mechanisms. The first is electroosmosis, which refers to the movement of solution due to an applied potential gradient.<sup>3</sup> The second is

electromigration, which involves the movement of a charged species in an electric field. When charged solutes are introduced into the capillary, they migrate at rate that depends on their charge-to-size ratio.

Adaptation of a detection method to a small volume separation method, like CZE, is a challenge. The detection method must not introduce additional band broadening while providing high sensitivity, high spatial resolution, and rapid response time.<sup>4</sup> Several detection methods have been used in conjunction with CZE including absorption and fluorescence spectrometry, electrochemistry with a microelectrode, and mass spectrometry.<sup>2,4-12</sup> Reviews covering various detection methods have appeared in the literature.<sup>8-10</sup> Electrochemical detection (EC) is often coupled with CZE and is attractive for a number of reasons. Some advantages of electrochemical detection are high sensitivity, which is not compromised by miniaturization, and rather simple and inexpensive instrumentation.<sup>9-12</sup> Two technical challenges with electrochemical detection are (i) decoupling the separation voltage from the electrode response (ii) reproducible positioning of the working electrode at the end of the separation capillary in end-column detection. Inadequate decoupling gives rise to noise at the electrochemical detector, which leads to decreased sensitivity.<sup>10-12</sup> Another important issue with electrochemical detection is the working electrode and its electrochemical properties. Due to the very small sample volume injected, a microelectrode must be used to achieve high detection sensitivity. Several different electrode materials and geometries have been used with metal (Pt) and

carbon fiber microelectrodes being the most popular.<sup>4</sup> A major issue, as discussed previously, is electrode deactivation and fouling due to the irreversible adsorption of reaction products and intermediates, and the resulting need for electrode pretreatment to reactivate the surface. Carbon fiber microelectrodes, in particular, are susceptible to strong adsorption of polar aromatic molecules, such as chlorophenols, in part, because of the presence of carbon-oxygen functionalities that make the surface polar and hydrophilic in nature and the extended  $\pi$ -electron system.

Boron-doped diamond microelectrodes have recently been employed in CZE, specifically for the amperometric detection of nitroaromatics, organophosphate agents, phenols and catecholamines.<sup>13,14,15</sup> Diamond exhibits a reproducible and stable oxidation response for these analytes without any surface pretreatment. The application of a diamond microelectrode for the direct and indirect amperometric detection of chlorinated phenols in CZE is reported herein. The objectives of this work were (i) to verify that the boron-doped diamond microelectrode can be used to detect these priority pollutants in CZE, (ii) to demonstrate that the microelectrode is resistant to fouling and provides a sensitive, reproducible and stable oxidation response for the chlorinated phenols, and (iii) to compare the detection figures of merit obtained by direct and indirect amperometric detection.



## 6.2. Results and Discussion

### 6.2.1. Surface Morphology and Microstructure of the Diamond Microelectrodes

Figure 6.1 a and b show SEM images of a sharpened Pt wire coated with a thin layer of diamond. The SEM image reveals a diamond overlayer consisting of randomly oriented, well-faceted diamond crystallites with base diameters from 1 to 3  $\mu\text{m}$ . A wide crystallite size distribution exists.<sup>13</sup> Films grown on Pt exhibit more morphological defects than do films deposited on Si substrates under similar conditions.<sup>13</sup>

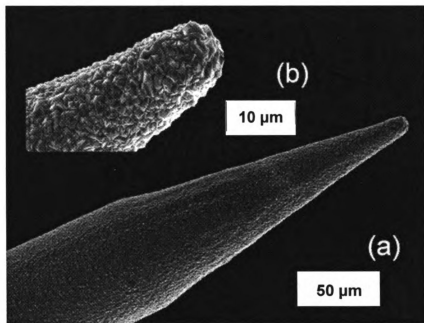


**Figure 6.1** SEM images of an electrochemically etched 76- $\mu\text{m}$  sharpened platinum wire coated with a polycrystalline diamond film. Images a and b show the film at different magnifications.

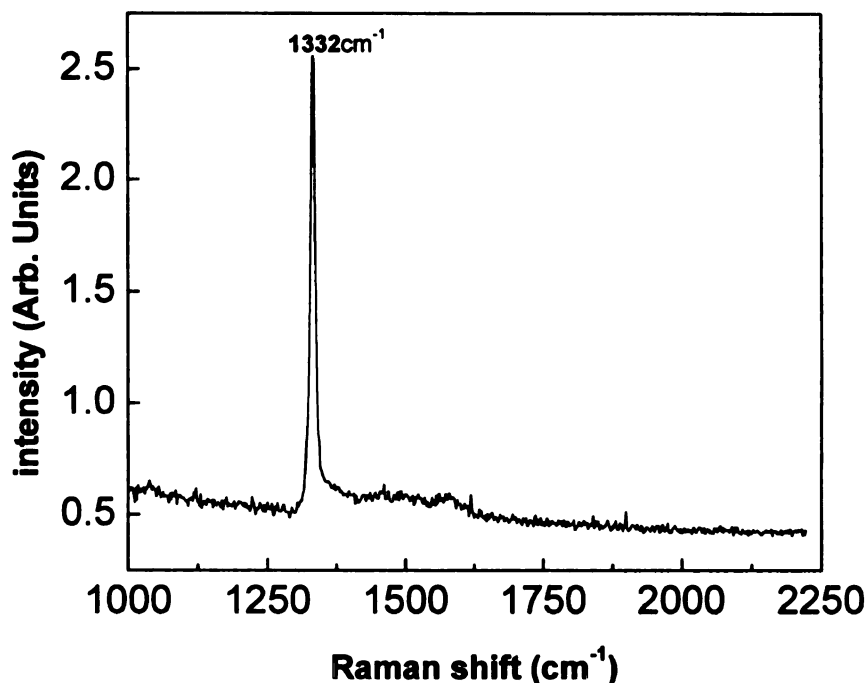


**Figure 6.2** Raman spectrum for a microcrystalline boron-doped diamond thin film deposited on a 76- $\mu\text{m}$  platinum wire. Integration time = 10 s.  $\lambda_{\text{ex}} = 532 \text{ nm}$ .

Figure 6.2 shows a Raman spectrum for a diamond film grown on a sharpened 76- $\mu\text{m}$  diameter Pt wire. The spectrum has an intense one-phonon diamond line at  $1332 \text{ cm}^{-1}$ . The full width at half-maxima (fwhm) is  $\sim 12 \text{ cm}^{-1}$ . By comparison, the linewidth for single-crystal diamond in the same spectrograph is  $2 \text{ cm}^{-1}$ . The larger fwhm for the polycrystalline film is indicative of a higher defect density as, to a first approximation, the peak width is inversely related to the phonon lifetime. This lifetime is reduced because of phonon scattering at the grain boundaries and defects.<sup>13</sup> There is minimal scattering intensity in the region near  $1500 \text{ cm}^{-1}$ , indicating that the film contains little nondiamond,  $\text{sp}^2$ -bonded carbon impurity.

## 6.2.2. Basic Voltammetric Response

The diamond microelectrode was initially characterized by cyclic voltammetry. A background voltammetric  $i$ - $E$  curve in 1 M KCl at 0.1 V/s, is shown in Figure 6.3A. Voltammetric features characteristic of Pt are not observed which is exemplified by the large overpotential for hydrogen evolution. The absence of these features indicates that cracks and pinholes are absent in the diamond overlayer. The increase in anodic current at ca. 1500 mV is due to the onset of chlorine evolution, which occurs on diamond with relatively low overpotential as compared to oxygen evolution. The potential region between -1000 and 1500 mV is featureless and characterized by a low and stable current. Figure 6.3 B shows a cyclic voltammetric  $i$ - $E$  curve for 1 mM  $\text{Fe}(\text{CN})_6^{-3/4}$  in 1M KCl at 10 mV/s. A sigmoidally shaped  $i$ - $E$  curve is seen with an  $E_{1/2}$  of 285 mV and a limiting current,  $i_{\text{lim}}$ , of ca. 40 nA. The curve shape remained unchanged with repeated cycling. The size of the electrode was such that a sigmoidal response was only observed at low scan rates. The exposed area was determined from the limiting current,  $i_{\text{lim}}$ , at the conically-shaped diamond microelectrode, which is described by a cylindrical and a conical term according to the equation<sup>16,17</sup>

$$i_{\text{lim}} = i_{qss}^{\text{cylinder}} + i_{ss}^{\text{cone}} \quad (1)$$

For a quasi-steady-state current (long times), it holds that the cylindrical term,

$i_{qss}^{\text{cylinder}}$ , is given by<sup>16,17</sup>

$$i_{qss}^{cylinder} = \frac{2nFADC}{r \ln \tau} \quad (2)$$

and the conical term,  $i_{ss}^{cone}$ , by<sup>16</sup>

$$i_{ss}^{cone} = 4nFDCr(1 + qH^p) \quad (3)$$

where  $n$  is the number of electrons transferred per equivalent,  $F$  is the Faraday constant,  $D$  is the diffusion coefficient ( $\text{cm}^2/\text{s}$ ),  $C$  is the bulk concentration of the analyte ( $\text{mol}/\text{cm}^3$ ),  $r$  is the cone radius ( $\text{cm}$ ),  $\tau = 4Dt/r^2$ ,  $q = 0.30661$ ,  $p = 1.14466$  and,  $H$  is the aspect ratio  $h/r$  where  $h$  is the height of the cone ( $\text{cm}$ ). The measurement period,  $t$  (s), is the time of the forward voltammetric scan. The cone dimensions were determined from the SEM image. The surface area of a cone is related to its aspect ratio according to the equation,

$$A = \pi r^2 (H+1)^{1/2}$$

For all the calculations, diffusion coefficients of  $6.7 \times 10^{-6} \text{ cm}^2/\text{s}$  for  $\text{Fe}(\text{CN})_6^{-3/4}$ , aspect ratio of 4.0, and a time  $t$  (s) of 30 s were used.<sup>13</sup> The theoretical current calculated from just the cone dimensions (equation 3) was calculated to be 30 nA. This is slightly lower than the experimental value of 40 nA (see Figure 6.3B). This difference is due to the fact that some length of the cylindrical portion is also exposed to the solution. Due to the manner in which the polypropylene insulation layer is applied to the microelectrode, it is difficult to reproducibly control the overall electrode length and, therefore, the amount of cylinder exposed. When the measured current exceeded the theoretical value, a portion of the cylindrical part was assumed exposed. In this case, the length of the cylindrical part was

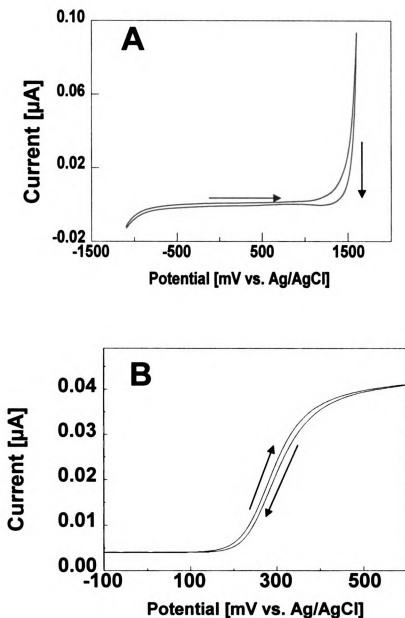


**Figure 6.3** (A) Background cyclic voltammetric i-E curve for a boron-doped diamond microelectrode in 1 M KCl. Scan rate = 100 mV/s. (B) Cyclic voltammetric i-E curve for 1 mM  $\text{Fe}(\text{CN})_6^{3-/4-}$  in 1 M KCl at a boron-doped diamond microelectrode. Scan rate = 10 mV/s.

calculated using equations 1 and 2, in which  $A = 2\pi rl$ . Nominally, the diamond microelectrode had a calculated surface area (cone + cylinder) of  $2.2 (\pm 0.7) \times 10^{-4} \text{ cm}^2$ .

A cyclic voltammetric *i*-*E* curve for 50  $\mu\text{M}$  2-chlorophenol in 10/20 mM borate/phosphate buffer, pH 8.4, at a diamond microelectrode is shown in Figure 6.4. The potential sweep rate was 100 mV/s. The faradaic current for the phenol oxidation commences at ca. 0.6 V and reaches a pseudo-steady state value of ca. 10 nA at potentials between 0.8 and 1.2 V. Beyond 1.2 V, the current increases due to the onset of oxygen evolution. The phenol oxidation occurs near the onset of oxygen evolution; therefore, both direct and indirect (via  $\text{OH}\cdot$ ) oxidation reactions are believed to occur.<sup>18</sup> No other redox peaks develop in the voltammogram during subsequent scans between -0.4 and 1.6 V. This is different from what was observed for a planar diamond thin-film electrode when mounted at the bottom of an electrochemical cell (see Chapter 4).<sup>18</sup> Presumably, the quasi-steady state diffusional flux at the diamond microelectrode transports the oxidation reaction products away from the surface before adsorption can occur and they are not detected.

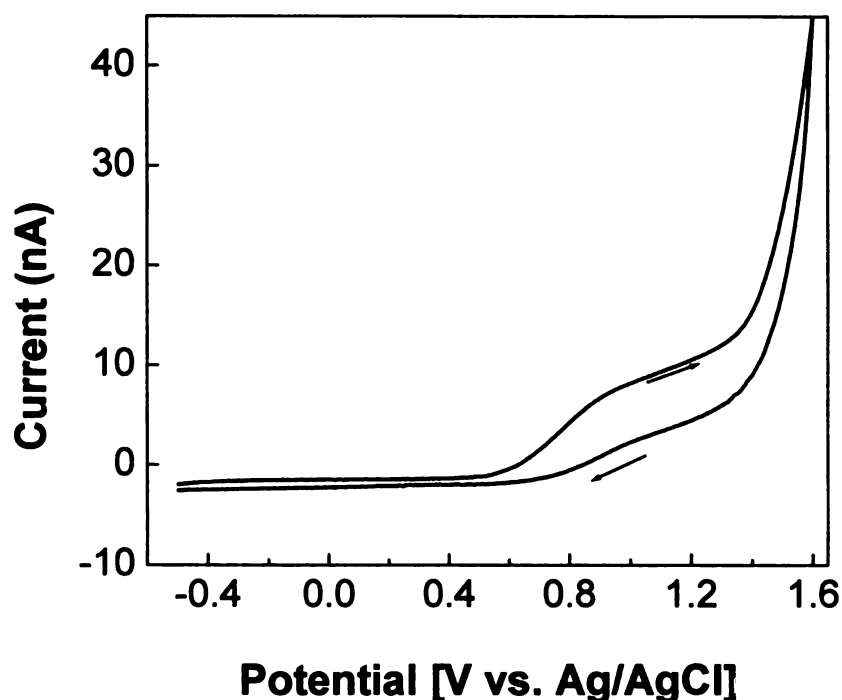


**Figure 6.4** Cyclic voltammetric i-E curve for 50  $\mu\text{M}$  2-chlorophenol in a 10/20 mM mixed-borate/phosphate run buffer, pH 8.4, at a boron-doped diamond microelectrode. Scan rate = 100 mV/s.

### 6.2.3. Direct Amperometric Detection of Chlorinated Phenols

Decoupling the separation voltage from the detection electrode signal is a key issue for CE-EC. Decoupling refers to the prevention of the electrophoretic current from returning to ground via the detection electrode. Increased background current and noise, greater response instability and potential shifts are observed when there is incomplete decoupling.<sup>19</sup> Two approaches are routinely used to isolate the detection electrode from the separation voltage: end-column and off-column detection. In end-column detection, the electrode is placed just outside the separation capillary. In this arrangement, the electrode is positioned

outside of the separation electric field. In off-column detection the electrode is isolated from the separation voltage by means of a “decoupler”.<sup>19-24</sup> We isolated the diamond microelectrode by positioning it just outside the end of the capillary column (so called end-column detection). The distance between the capillary and the microelectrode was adjusted by positioning the capillary, which was mounted in the detection cell normal to the working electrode. The distance between the end of the capillary and the microelectrode was kept as short as possible (by eyesight) in order to minimize dilution effects and band broadening.<sup>25</sup> We estimated that the separation distance was on the order of 20 – 30  $\mu\text{m}$ . If this distance is too great then the solute zone gets diluted leading to reduced peak heights, broader peaks, and higher detection limits results. The capillary-electrode spacing also influences the separation efficiency. By maintaining a low separation current and an adequate distance between the microelectrode and capillary, the electrode response was relatively unaffected by the separation voltage and acceptable signal-to-noise ratios and minimal potential shifts were obtained.

CE-EC experiments were performed using a mixed 10/20 mM borate/phosphate run buffer at pH 8.4, a 76-cm-long fused silica capillary (27  $\mu\text{m}$  i.d.), and a separation voltage of 20 kV (263 V/cm). This run buffer was selected based upon results from numerous optimization runs in which the buffer pH and composition were varied. Solutes were injected electrokinetically for 3 s at 8 kV. The injected volume of an electroosmotic flow marker, methanol, was calculated



to be 1.1 nL. Based on the migration time and column length, the EOF was calculated to be  $6.2 \times 10^{-4} \text{ cm}^2/\text{Vs}$ . After application of the detector potential, the separation voltage across the column was applied. The electrode current was allowed to stabilize before making an injection. In general, the background current stabilized within 3 - 4 minutes after detector turn-on. This is a useful material property.

Hydrodynamic voltammetric i-E curves were recorded for each of the chlorinated phenols in order to determine the optimum detection potential. Figure 6.4 shows i-E curves for 20  $\mu\text{M}$  concentrations of each pollutant. A potential increment of 50 mV was used. Each datum shown is the average current value for at least three injections. The oxidation current for each solute commences around 800 mV and reaches a near limiting value at ca. 1050 mV. A more or less sigmoidally-shaped response is observed for each solute. This suggests that the oxidation current is limited by the flux of analyte to the electrode surface. The limiting current at the diamond microelectrode in this cross-flow geometry is given, at least approximately, by the following expression<sup>26</sup>

$$i_l = nFCK_mAU^\alpha$$

in which  $i_l$  is the mass-transfer limited current,  $n$  is the number of electrons transferred per equivalent,  $C$  is the solute concentration,  $A$  is the electrode area,  $K_m$  is the mass transfer coefficient, and  $U$  is the average volume flow rate.  $\alpha$  is a constant that ranges from 0.33 to 1.0. The limiting current for each of the chlorinated phenols differs by a maximum of a factor of three even though the

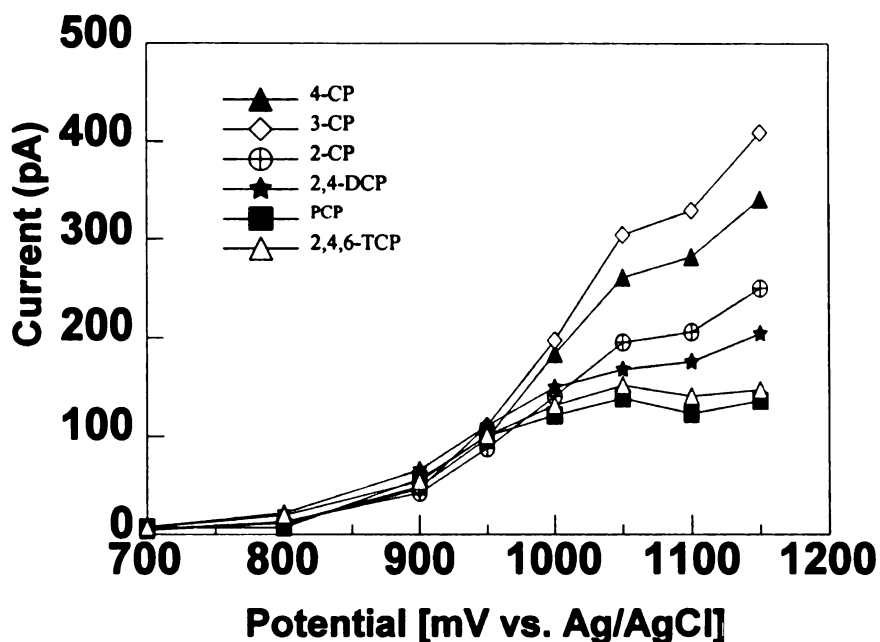


**Figure 6.5** Hydrodynamic voltammetric i-E curves for the six chlorinated phenols at a boron-doped diamond microelectrode recorded in a 10/20 mM borate/phosphate run buffer, pH 8.4. Separation voltage = 20 kV. Capillary = 27  $\mu\text{m}$  i.d. x 76 cm long. Injection = 8 kV for 3s. Solute concentration = 20  $\mu\text{M}$ .

**Table 6.1**  $\text{pK}_a$  Values and the Elution Order for Phenol and Different Chlorinated Phenols.

Compound	$\text{pK}_a^{26}$	Elution order
Phenol	10.0	1
4-chlorophenol	9.43	2
3-chlorophenol	8.97	3
2-chlorophenol	8.52	4
2,4-dichlorophenol	7.89	5
2,4,6-trichlorophenol	6.1	6
Pentachlorophenol	4.74	7

solution concentration, the number of electrons transferred (assumed to be 1 for oxidation to phenoxy radical), and the hydrodynamic flow conditions were the same for all the solutes. There are two factors that lead to the differences in limiting current. One is the diffusion coefficient for each, which we did not measure nor did we find values for in the literature. The other, and the one most influential, is the different mass of each solute (i.e. concentration) loaded onto the column during the electrokinetic injection. The mass loading depends on the electrokinetic injection conditions, the solution concentration, and the electrophoretic mobility of the solute. In the present case, all the solutes possessed some degree of negative charge because the run buffer pH was 8.4 and the  $pK_a$  values for each range from 4.74 to 10. Since the solutes are negatively charged, the direction of their electrophoretic movement opposes the electroosmotic flow. Therefore, the solute with the lowest loading should be the one with the most negative charge/size ratio, that is the one with the lowest  $pK_a$ , and the solute with the highest loading should be the one with the least negative charge/size ratio, that is the one with the highest  $pK_a$ . The limiting currents do in fact follow this trend with the magnitude decreasing in order of decreasing  $pK_a$ : 3-CP ( $pK_a = 8.97$ ) > 4-CP ( $pK_a = 9.43$ ) > 2-CP ( $pK_a = 8.52$ ) > 2,4-DCP ( $pK_a = 7.89$ ) > 2,4,6-TCP ( $pK_a = 6.1$ ) > PCP ( $pK_a = 4.74$ ).<sup>27</sup> The observance of sigmoidally-shaped hydrodynamic i-E curves at the microelectrode is different from our previously reported work on the electrooxidation of chlorinated phenols at boron-doped microcrystalline and nanocrystalline diamond thin-film electrodes.<sup>18</sup> In that work, sigmoidally-shaped hydrodynamic i-E curves were not observed for all the

pollutants (e.g., phenol, 2-chlorophenol, 3-chlorophenol, and 4-chlorophenol) in FIA-EC, with exception of PCP, and we concluded that the maximum oxidation current was under mixed control by direct and indirect (anodic oxygen transfer reactions) electrooxidation reactions and mass transport. The i-E curves for 2-chlorophenol, 3-chlorophenol, and 4-chlorophenol in Figure 6.5 also show a current increase at 1150 mV. This is due to the onset of oxygen evolution which begins above 1100 mV (background hydrodynamic i-E curves not shown). Based on the hydrodynamic voltammograms, the optimum detection potential for all the pollutants was determined to be 1050 mV. The normal background current at this potential was ~ 15 pA and the peak-to-peak noise was 2 to 3 pA. The background noise was unaffected by the separation voltage provided there was sufficient distance between the electrode and the end of the capillary (i.e., adequate decoupling).

Figure 6.6 shows a typical electropherogram for an equimolar mixture (20  $\mu$ M) of all seven pollutants. All peaks are well resolved from one another but each has an asymmetric shape (tailing). Separation of all seven solutes is accomplished in less than 14 min and all migration times were very reproducible during an 8-h run period. The run buffer pH influences an electrophoretic separation by affecting the analyte charge, thus, its electrophoretic mobility and the electroosmotic flow (EOF). Furthermore, selectivity, resolution, and peak shape are also all pH-sensitive. Small differences in solute  $pK_a$  (e.g., 2-chlorophenol, 3-chlorophenol, and 4-chlorophenol) are enough to enable

separation by CE. In the present case, separation was performed at an optimum pH of 8.4. Below this pH, significant peak overlap was observed for phenol, 4-chlorophenol, and 3-chlorophenol. Above this pH, 2,4-dichlorophenol, 2,4,6-trichlorophenol, and pentachlorophenol were poorly resolved from one another. The electrophoretic mobility of a solute is governed by its charge/size ratio as well the concentration and viscosity of the buffer. At pH 8.4, all the chlorophenols possess some negative charge (deprotonated) and the elution order exhibits a correspondence with the  $pK_a$  (see Table 6.1), as expected. Phenol, having the least negative charge (highest  $pK_a$ ), elutes first and pentachlorophenol, having most negative charge (lowest  $pK_a$ ), elutes last. The direction of electrophoretic movement of each solute is against the electroosmotic flow direction. The differences in peak height are partly attributed to differences in the solute loading during the electrokinetic injection. The peak tailing appears to be related to the solute flow across the diamond microelectrode during migration, and not to on-column effects. The migrating solute first encounters the end of the electrode as it migrates off the column. This is followed by flow and diffusional spreading across the length of the exposed electrode. Dilution of the solute occurs as it travels across the fiber length so the current goes down. This influence was confirmed by using diamond microelectrodes of differing lengths. The extent of tailing increased with increasing electrode length. Shin et al. also observed some peak tailing when using a diamond microelectrode for the detection of catecholamines.<sup>14</sup> Table 6.2 presents a summary of the detection figures of merit for the chlorinated phenols. The data are reported at the 95% confidence level.

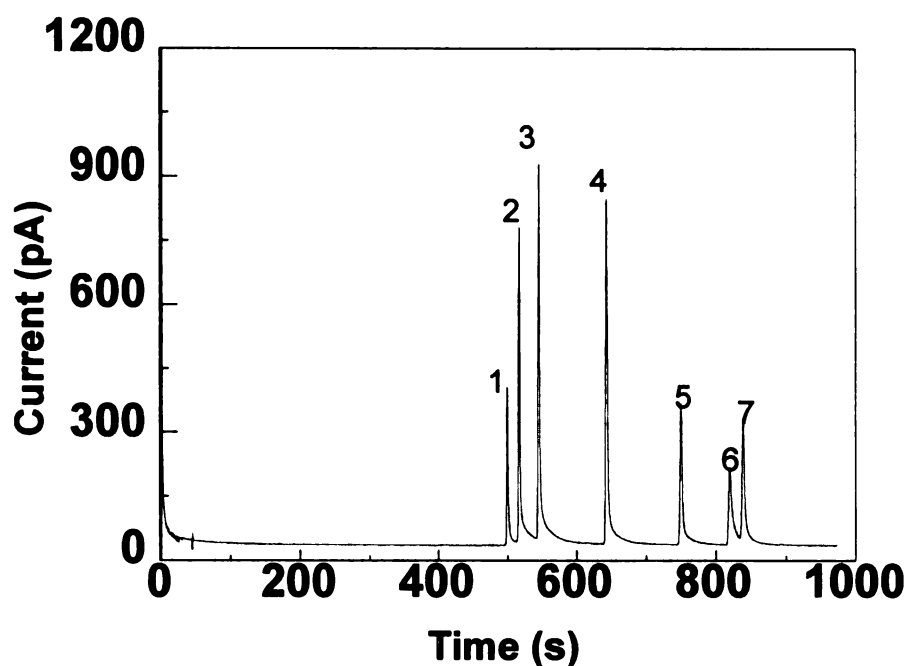


**Figure 6.6** A typical electropherogram for phenol and six chlorinated phenols using direct amperometry recorded in a 10/20 mM borate/phosphate run buffer, pH 8.4. Separation voltage = 20 kV. Capillary = 27  $\mu\text{m}$  i.d. x 76 cm long. Detection potential = +1050 mV (vs. Ag/AgCl). Injection = 8 kV for 3s. Solute concentration = 20  $\mu\text{M}$ .

The reproducibility of the electrode response was determined from 9 injections of a solution containing all seven pollutants (20  $\mu\text{M}$  each) prepared in the run buffer.

The separation efficiency ranged from 85,000 to 302,000 plates/m

$(N = \frac{41.7(t_m / w_{0.1})^2}{b/a + 1.25})$  where  $w_{0.1}$  is the width of the peak at 10% from the base,

$b/a$  is the asymmetry factor). The linear dynamic range for each was at least 3

orders of magnitude with correlation coefficients greater than 0.993. The

sensitivity for all the pollutants ranged from 6 to 16 pA/ $\mu\text{M}$ . The minimum

**Table 6.2 Detection Figures of Merit for Phenol and the Chlorinated Phenols in Direct Amperometry Coupled with Capillary Electrophoresis.<sup>a</sup>**

Analyte	LDR ( $\mu\text{M}$ )	Sensitivity ( $\text{pA}/\mu\text{M}$ )	LOQ ( $\text{nmol/L}$ )	Estimated mass LOQ (fg)	Response precision (n = 9) RSD%	Efficiency (plates/m)
Phenol	0.5 – 100 $r^2 = 0.994$	$10.7 \pm 7.3$	500 (S/N = 3) (47 ppb)	10	$5.6 \pm 0.2$	302,000
2-CP	0.1 – 100 $r^2 = 0.999$	$14.7 \pm 4.2$	100 (S/N = 3) (13 ppb)	14	$4.7 \pm 0.5$	133,000
3-CP	0.1 – 100 $r^2 = 0.998$	$16.3 \pm 4.1$	100 (S/N = 4) (13 ppb)	14	$5.2 \pm 0.2$	121,000
4-CP	0.1 – 100 $r^2 = 0.993$	$15.0 \pm 4.8$	100 (S/N = 4) (13 ppb)	14	$4.5 \pm 1.2$	116,000
2,4-DCP	0.5 - 100 $r^2 = 0.999$	$9.9 \pm 3.1$	500 (S/N = 3) (82 ppb)	90	$5.0 \pm 0.2$	129,000
2,4,6-TCP	0.5 – 100 $r^2 = 0.998$	$5.9 \pm 3.9$	500 (S/N = 3) (99 ppb)	107	$5.4 \pm 0.7$	85,000
PCP	0.5 – 100 $r^2 = 0.997$	$6.2 \pm 2.4$	500 (S/N = 3) (133 ppb)	146	$5.6 \pm 0.5$	187,000

<sup>a</sup> CE-EC parameters:  $E_{inj} = 8 \text{ kV}$ ;  $t_{inj} = 3 \text{ s}$ ; capillary dimensions =  $27 \mu\text{m}$  i.d. x  $76 \text{ cm}$  long;  $E_{sep} = 20 \text{ kV}$ ; and  $E_{det} = 1.05 \text{ V}$ . The data are based on the response of 3 microelectrodes and are reported at the 95% confidence level. LDR = linear dynamic range. LOQ = limit of quantitation (the minimum concentration of analyte injected and measured). The mass limit of quantitation was estimated from the calculated injection volume for methanol,  $1.1 \text{ nL}$ . This was calculated using the expression:

$$V_{inj} = (E_{inj} \times t_{inj} \times V_{capillary}) / E_{sep} \times t_{mig}$$

concentration measured ( $S/N \geq 3$ ) was  $100 \text{ nM}$  ( $13 \text{ ppb}$ ) for 2-chlorophenol, 3-chlorophenol and 4-chlorophenol, and  $500 \text{ nM}$  ( $47\text{-}133 \text{ ppb}$ ) for phenol, 2,4-dichlorophenol, 2,4,6-trichlorophenol, and pentachlorophenol. The estimated

mass limits of quantitation were in the femtogram (fg) range, calculated using the injected volume for methanol, 1.1 nL. Good peak height reproducibility was observed for all analytes with a nominal value of  $5.6 \pm 0.5\%$ , or less. In summary, the diamond microelectrode exhibited good electroanalytical performance with a low peak-to-peak noise (2 to 3 pA); low and stable background current under the electrophoretic conditions imposed; and sensitive, reproducible and stable responses for all the chlorinated phenols without electrode deactivation (fouling) during extended use. Additionally, no pretreatment was required for electrode activation. The low and stable background current and noise allowed for relatively low mass limits of detection to be achieved. These results are consistent with two previous reports that diamond thin-film electrodes are useful for the detection of chlorinated phenols with relatively high resistance to surface fouling.<sup>18,28</sup>

The detection figures of merit obtained for the diamond microelectrode appear superior to other data reported in the literature, such as for UV detection.<sup>29-32</sup> As far as electrochemical detection is concerned, there have been relatively few reports of chlorinated phenol analysis presumably because of the electrode deactivation and fouling. Several approaches have been employed to try and minimize electrode fouling. Hilmi and co-workers used a Pt electrode modified with electrodeposited Sn to detect chlorinated phenols. The modified Pt electrode exhibited enhanced sensitivity as well as reduced electrode fouling by phenol oxidation reaction products, as compared to bare Pt.<sup>33</sup> The limits of detection



achieved were in the low micromolar range and the separation efficiencies ranged from 88,000 to 145,000 plates/m. The response precision was 4%, or less. In another report, the authors reported improved detection figures of merit for chlorinated phenols using nonaqueous capillary electrophoresis with end-column detection.<sup>34</sup> The nonaqueous medium offered high sensitivity and alleviated the electrode fouling problem. Concentration limits of detection were in the nanomolar range with a response precision of 4%, or less. Wang and co-workers utilized electrochemical detection with a thick screen-printed carbon electrode in combination with microchip electrophoresis to analyze chlorinated phenol solutions. The concentration limits of detection were in the 1 to 2  $\mu\text{M}$  range. The response precision was 6.6%, or less, for the chlorinated phenols.<sup>35</sup> The group also reported on the use of a boron-doped diamond electrode with microchip electrophoresis for the detection of nitroaromatics, organophosphate agents as well as chlorinated phenols.<sup>15</sup> No detection figures of merit were reported for the chlorinated phenols, but diamond did provide higher sensitivity, lower noise and better resistance to fouling for the nitroaromatics than did a screen-printed carbon electrode. Gaitonde and co-workers used an on-column electrochemical detection with a modified carbon fiber for the analysis of chlorinated phenols extracted from industrial effluents.<sup>36</sup> The limits of detection reported were in the low ppb range.

As mentioned before, amperometric detection of phenols is commonly plagued by surface deactivation and fouling due to the formation of a polymeric

film on the electrode surface.<sup>37,38</sup> The mechanistic work by Gattrell and Kirk reveals that the phenol oxidation reaction proceeds initially through the formation of a phenoxy radical species, which can subsequently undergo radical-radical coupling to form polymeric and oligomeric species. Follow-up direct and indirect oxidation reactions, producing soluble products such as hydroquinone and catechol, are also possible.<sup>18,28,37,38</sup> No passivation of the diamond microelectrode was observed, as it could be used in multiple measurements for several weeks with little deactivation. *This is a major attribute of diamond for monitoring this important class of pollutants.*

#### **6.2.4. Indirect Amperometric Detection of Chlorinated Phenols**

The general applicability of CE-EC can be expanded if indirect detection methods are employed. Therefore, we also conducted a study of the indirect amperometric detection of the same chlorinated phenols. Although direct amperometry is a sensitive and stable means for solute monitoring, many solutes are not electroactive and, therefore, cannot be detected. Indirect amperometric detection circumvents this limitation and is based on the displacement of an electroactive molecule added to the run buffer (electrophore) by the electroinactive solute.<sup>39</sup> Due to the need to preserve charge neutrality, the electrophore in the buffer is displaced by the analytes zones. For analytes with the same charge as the electrophore, displacement of the detectable ions results in a lower level of the electrophore and a negative peak for the analyte results.<sup>39</sup> Quantitation is made by measuring a negative peak current or charge. The extent

of electrophore displacement by the solute is known as the transfer ratio (TR). It is defined as the number of moles of electrophore displaced by one mole of the analyte.<sup>39</sup> Indirect UV/Vis detection has often been utilized with CE, however, there are only a few reports of indirect electrochemical detection in aqueous or non-aqueous media.<sup>40-42</sup> Olefirowicz and Ewing were one of the first to demonstrate the practicality of coupling indirect amperometric detection with CE as they applied this method for the analysis of electroinactive cationic amino acids and dipeptides. The authors used dihydroxybenzylamine (DHBA) as the cationic electrophore. A stable background signal during its continuous oxidation at the detection potential of 700 mV vs. SCE was observed. Zones of electroinactive cations displaced the DHBA during the electrophoretic separation and were detected as negative peaks. Mass detection limits were in the femtogram (fg) range, or lower.<sup>40</sup>

In the present work, we tested the diamond microelectrode for the indirect amperometric detection of chlorinated phenols and compared the detection figures of merit with those obtained by the direct method. Several criteria must be met by an ion or molecule to function as a suitable electrophore. For example, the electrophore must have well-defined electrochemical behavior at the detector electrode, the electrode must exhibit good electrochemical response stability for the electrophore's redox reaction, and the electrophore must have a charge and electrophoretic mobility similar to that of the solutes being separated. In our studies, ferrocene carboxylic acid was chosen as the anionic electrophore.

Figure 6.7 shows a cyclic voltammetric i-E curve for 0.8 mM ferrocene carboxylic acid in 0.01 M phosphate buffer, pH 8.1, at a diamond microelectrode. A well-defined sigmoidal curve is observed at this slow scan rate with an  $E_{1/2}$  of 340 mV (vs. Ag/AgCl) and a steady state oxidation current of 35 nA. Based on the curve shape, a detection potential of 450 mV was selected.

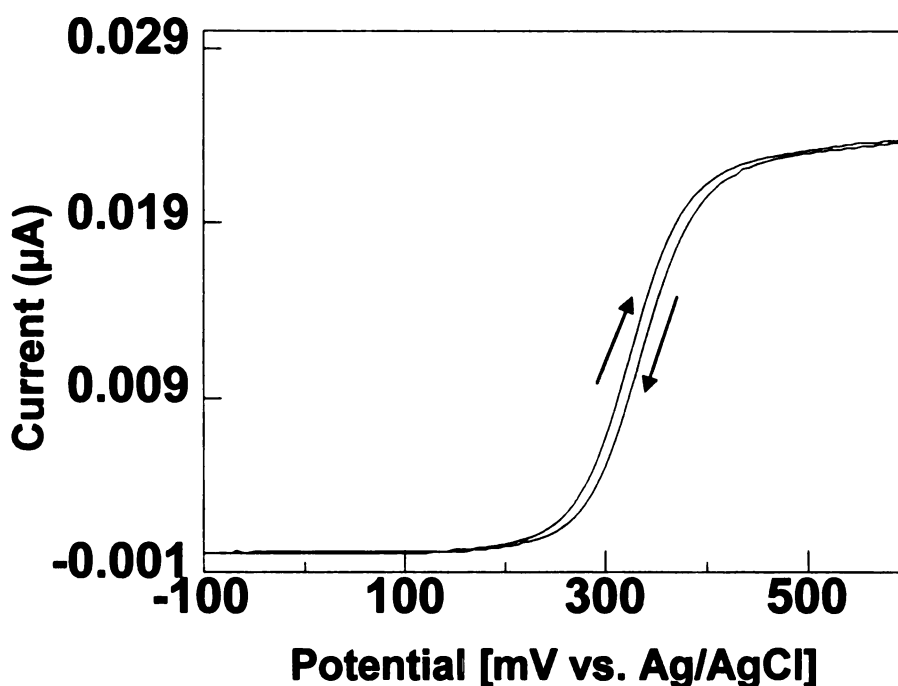


**Figure 6.7** Cyclic voltammetric i-E curve for 0.8 mM ferrocene carboxylic acid in 10 mM phosphate buffer, pH 8.1, at a boron-doped diamond microelectrode. Scan rate = 5 mV/s.

A series of experiments was first conducted to determine the appropriate run buffer composition, ionic strength, and pH for the separation and indirect detection of the chlorinated phenols. After much optimization, a run buffer

composition of 0.01 M phosphate buffer at pH 8.1 was found to be appropriate. A typical electropherogram for three of these pollutants is shown in Figure 6.8. The electropherogram shows the separation of 2-chlorophenol, 3-chlorophenol, and 2,4-dichlorophenol obtained using a 30  $\mu\text{m}$  i.d. x 76 cm fused silica capillary. The large background current, due to the oxidation of ferrocene carboxylic acid in the run buffer, decreases when each chlorinated phenol migrates through the column and reaches the electrode. The analytes were identified by injecting the individual solutes and matching the migration times. It should be noted that all seven solutes can be separated and detected, even though the electropherogram shows for only three. The first peak, A, in the electropherogram is the system peak observed at a migration time corresponding to the rate of electroosmotic flow.<sup>40</sup> The origin of this system peak is unclear, but it is related in some manner to the electrophore as the peak magnitude (anodic current) increased with increasing electrophore concentration. The peak marked B represents a zone in which the ferrocene carboxylic acid is virtually absent (i.e., vacancy zone). If a species present in the run buffer is also contained in the sample at a different concentration, then a vacancy will be created. The signal magnitude for this vacancy will depend on the ratio of its concentration in the sample and the run buffer.<sup>43,44</sup> Thus, if a component is absent in the injected sample but present in the run buffer, then the sample plug represents a vacancy and during application of a separation voltage, this vacancy migrates as an individual zone and is detected.<sup>43</sup> This vacancy (negative peak) is present because all solute samples were prepared in the run buffer without adding the electrophore.<sup>40</sup> Proof that this

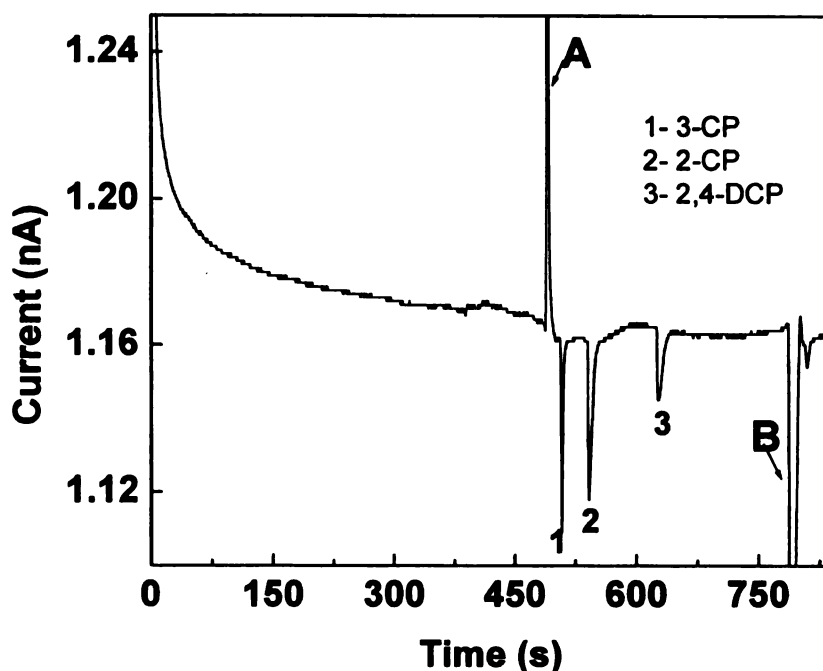


**Figure 6.8** An electropherogram for 3-chlorophenol, 2-chlorophenol, and 2,4-dichlorophenol using indirect amperometry recorded in a 10 mM phosphate run buffer, pH 8.1. The electrophore was 0.8 mM ferrocene carboxylic acid. Detection was accomplished with a boron-doped diamond microelectrode. Separation voltage = 20 kV. Capillary 30  $\mu\text{m}$  i.d. x 76 cm long. Detection potential = 450 mV (vs. Ag/AgCl). Injection = 8 kV for 3 s. Solute concentrations = 200  $\mu\text{M}$ .

peak is associated with the electrophore vacancy is the fact that the peak magnitude increased with increased concentration of ferrocene carboxylic acid in the run buffer. The peak shapes for the solutes are sharp and narrow with no evidence of tailing or fronting. This is consistent with the electrophore having a mobility similar to those of the solute.<sup>45,46</sup> Peak fronting or tailing can occur when the electrophoretic mobilities of the analyte and electrophore are significantly different.<sup>47</sup> Ferrocene carboxylic acid was found to have an electrophoretic

mobility that is similar to the mobilities of the chlorinated phenols under the electrophoretic conditions used. This is important in order to maximize sensitivity and minimize dispersion effects.<sup>45,47</sup> Electromigration dispersion effects are related to the relative mobility differences between a solute and the added electrophore. Tailing results when the conductivity within the zone is lower than in the electrolyte, and peak fronting results when the reverse happens.<sup>46</sup> Proper choice of the electrophore provides the best peak shapes, maximizes the transfer ratio, and minimizes competitive displacement.<sup>45</sup> The lack of tailing due to the shape of the microelectrode as observed in direct measurements, could be possibly due to the fact that detection here is not due to the direct oxidation of the analyte but rather a displacement reaction.

A key parameter in indirect amperometric detection is the dynamic reserve (DR), which is a dimensionless parameter defined as the ratio of the background signal magnitude to the noise in that signal. The DR is one factor controlling the minimum concentration ( $C_{lim}$ ) theoretically detectable for a given set of conditions.  $C_{lim}$  is defined as

$$C_{lim} = \frac{C_m}{(DR)(TR)}$$

in which  $C_m$  is the concentration of the electrophore and TR is the displacement ratio (transfer ratio).<sup>39</sup> The DR limits the fractional change in the background signal that can be recognized. The greater the DR, the lower the  $C_{lim}$ . For the chlorinated phenols, the DR was determined by measuring the steady-state

current for the electrophore at 450 mV and dividing it by the corresponding peak-peak noise (~ 3 - 4 pA) at concentrations from 50  $\mu$ M – 1 mM. There was a clear dependence of DR on the electrophore concentration up to 0.8 mM. As the electrophore concentration increased, the DR increased from 150 at 50  $\mu$ M to 1530 at 0.8 mM. In addition, as the concentration of the electrophore increased, the magnitude of displacement by the 2-chlorophenol, 3-chlorophenol, and 2,4-dichlorophenol also increased. For example, with 0.5 mM ferrocene carboxylic acid, the magnitudes of the 2-chlorophenol, 3-chlorophenol, and 2,4-dichlorophenol were 37, 49, and 14 pA, respectively. When the concentration of the electrophore was increased to 0.8 mM the negative peak magnitudes increased to 102, 161, and 40 pA, respectively. Above this electrophore concentration, no additional increase in the chlorinated phenol signal was seen. This could be due to the high background signal resulting from the electrophore. This makes it more difficult to measure changes in the background signal due to displacement by a solute. Thus, 0.8 mM was determined to be the optimum electrophore concentration for the indirect detection. It's worth noting that DR is related to  $C_m$  so decreasing the electrophore concentration will not necessarily improve the detection limit because DR is simultaneously reduced.<sup>47</sup>

The separation efficiency and the detection figures of merit for 2-chlorophenol, 3-chlorophenol, and 2,4-dichlorophenol were evaluated. Table 6.3 contains a summary of the data. The peaks for these three pollutants were well-resolved with separation efficiencies of 101,000, 224,000, and 69,000 plates/m



for 2-chlorophenol, 3-chlorophenol, and 2,4-dichlorophenol, respectively. A linear dynamic range for all three is seen to range between 30 and 600  $\mu\text{M}$  with correlation coefficients greater than 0.996. The sensitivities for all three solutes are between 300 and 900  $\text{pA}/\text{mM}$  and are lower than those observed in direct amperometry. The concentration limits of quantitation were 30  $\mu\text{M}$  (4 ppm) for 2- and 3-chlorophenol, and 50  $\mu\text{M}$  (8 ppm) for 2,4-dichlorophenol at a  $\text{S}/\text{N} \geq 3$ . These values are higher than those observed in direct amperometry. The mass limits of quantitation, based on a 1.1 nL injection volume, are from 5 to 10 pg. The electrode response reproducibility was excellent for 10 injections with values less than  $3.2 \pm 0.7\%$  for all three solutes. The diamond microelectrode exhibited low peak-to-peak noise (3 - 4 pA) and stable background current under the imposed electrophoretic conditions. The background current at the detection potential remained stable over periods of days. In fact, the electrode could be used for several weeks without any response attenuation. In summary, the results indicate that the diamond microelectrode functions well for the indirect amperometric detection of the chlorinated phenols. The linear dynamic range is lower, the sensitivity is lower and the lowest concentration measured and detected is higher for the three pollutants as compared to direct amperometry. However, the response reproducibility and response stability are equally as good. The figures of merit reported herein compare favorably with those reported for other in indirect amperometric detection studies.<sup>40,42</sup>

**Table 6.3 Detection Figures of Merit for Chlorinated Phenols in CZE with Indirect Amperometric Detection.<sup>b</sup>**

Compound	2-CP	3-CP	2,4-DCP
<b>Linear Dynamic Range (<math>\mu\text{M}</math>)</b>	30 - 600	30 - 600	50 - 600
<b>Correlation Coefficient, <math>r^2</math></b>	0.999	0.997	0.996
<b>Sensitivity (pA/mM)</b>	774 $\pm$ 143	906 $\pm$ 108	339 $\pm$ 29
<b>Concentration LOQ (<math>\mu\text{mol/L}</math>)</b>	30 (S/N = 6)	30 (S/N = 6)	50 (S/N = 6)
<b>Estimated Mass LOQ (pg)</b>	4.7	4.7	9.8
<b>Peak Height RSD% (n =10)</b>	3.2 $\pm$ 0.7	1.6 $\pm$ 0.8	3.0 $\pm$ 0.8
<b>Efficiency (plates/m)</b>	101,000	224,000	69,000

<sup>b</sup> CE-EC parameters:  $E_{inj} = 8 \text{ kV}$ ;  $t_{inj} = 3 \text{ s}$ ; capillary dimensions =  $30 \mu\text{m}$  i.d. x 76 cm long;  $E_{sep} = 20 \text{ kV}$ ; and  $E_{det} = 0.45 \text{ V}$ . The data is based on the response of 3 microelectrodes and are reported at the 95% confidence level. LOQ = limit of quantitation (the minimum concentration of analyte injected and measured). The mass limit of quantitation was estimated from the calculated injection volume for methanol, 1.1 nL.

### 6.3. Conclusions

Analysis of aqueous solutions containing chlorinated phenols was accomplished by capillary electrophoresis with direct and indirect amperometric detection using a boron-doped diamond microelectrode. The diamond microelectrode, used in the end-column arrangement, exhibited a low and stable background current with low peak-to-peak noise and good electrochemical

activity for the pollutants without any conventional pretreatment. The electrode performance was evaluated in terms of the linear dynamic range, sensitivity, limit of quantitation, and response precision for the detection of several priority pollutants (2-chlorophenol, 3-chlorophenol, 4-chlorophenol, 2,4-dichlorophenol, 2,4,6-trichlorophenol, and pentachlorophenol). The diamond microelectrode yielded good detection figures of merit for these contaminants in the direct amperometric mode with no evidence of any deactivation or electrode fouling. As an example, the lowest concentration measured for 2-chlorophenol was 100 nM or 13 ppb (S/N = 3) and the relative standard deviation of the peak height for 9 injections was  $4.7 \pm 0.5\%$  (est. 1.1 nL inj.). The separation efficiency ranged between 85,000 and 302,000 plates/m for the seven solutes.

The microelectrode was also employed for the indirect detection of the chlorinated phenols. In this approach, which is useful for detecting electroinactive solutes, ferrocene carboxylic acid was added to the run buffer as the electrophore. Good detection figures of merit were also achieved for the separation and detection of 2-chlorophenol, 3-chlorophenol, and 2,4-dichlorophenol in this mode, although the lowest concentration measured were higher than those obtained by direct amperometric detection. For example, the lowest concentration measured for these pollutants was in the mid micromolar range (1-10 ppm) with excellent response reproducibility of  $3.2 \pm 0.8\%$ , or less.

## 6.4. References

1. Holland, L.A.; Leigh, M.A.; *Electrophoresis* **2002**, *23*, 3649.
2. Deterding, L.J.; Parker, C.E.; Perkins, J.R.; Moseley, M.A.; Jorgenson, J.W.; Tomer, K.B.; *J. Chromatogr.* **1991**, *554*, 329.
3. Foret, F.; Krivankova, L.; Bocek, P.; *Capillary Zone Electrophoresis 1993* VCH Verlagsgesellschaft, Weinheim.
4. You, T.Y.; Yang, X.R.; Wang, E.; *Electroanalysis*, **1999**, *11*, 459.
5. He, Y.; Pang, H.M.; Yeung, E.S.; *J. Chromatogr. A* **2000**, *894*, 179.
6. Kang, S.H.; Wei, W.; Yeung, E.S.; *J. Chromatogr. B* **2000**, *744*, 149.
7. Voegel, P.D.; Zhou, W.; Baldwin, R.P.; *Anal. Chem.* **1997**, *69*, 951.
8. Swiney, K.; Bornhop, D.J.; *Electrophoresis* **2000**, *21*, 1239.
9. Matysik, F.-M.; *Electrophoresis* **2002**, *23*, 400.
10. Baldwin, R.P.; *Electrophoresis* **2000**, *21*, 4017.
11. Ewing A.G.; Wallingford, R.A.; Olefirowicz, T.M.; *Anal. Chem.* **1989**, *61*, 292A.
12. Lacher, N. A.; Garrison, K. E.; Lunte, S.M.; *Electrophoresis* **2001**, *22*, 2526.
13. Cvacka, J.; Quaiserova, V.; Park, P.; Show, Y.; Muck, A. Jr.; Swain, G.M.; *Anal. Chem.* **2003**, *75*, 2678.
14. Shin, D.; Sarada, B.V.; Tryk, D.A.; Fujishima, A.; *Anal. Chem.* **2003**, *75*, 530.
15. Wang, J.; Chen, G.; Chatrathi, M.P.; Fujishima, A.; Tryk, D.A.; Shin, D.; *Anal. Chem.* **2003**, *75*, 935.
16. Bard, A.J.; Faulkner, L.R.; *Electrochemical Methods Fundamentals and Applications*, 2<sup>nd</sup> ed.; John Wiley & Sons: New York, **2001**.
17. Zoski, C.G.; Mirkin, M.V.; *Anal. Chem.* **2002**, *74*, 1986.

18. Muna, G.W.; Tasheva, N.; Swain, G.M.; *Environ. Sci. Technol.* **2004**, *38*, 3674.
19. Matysik, F-M.; *J. Chromatogr.* **1996**, *742*, 229.
20. Wallingford, R.A.; Ewing A.G.; **1987**, *59*, 1762.
21. Qian, J.H.; Wu, Y.Q.; Yang, H.; Michael, A.C.; *Anal. Chem.* **1999**, *71*, 4486.
22. Lacher, N. A.; Lunte, S.M.; Martin, R.S.; *Anal. Chem.* **2004**, *76*, 2482.
23. Huang, X.; Zare, R.N.; Sloss, S.; Ewing, A.G.; *Anal. Chem.* **1991**, *63*, 189.
24. Lu, W.; Cassidy, R.M.; *Anal. Chem.* **1994**, *66*, 200.
25. Gehardt, G.C.; Cassidy, R.M.; Baranski, A.S.; *Anal. Chem.* **1998**, *70*, 2167.
26. Wang, J. *Analytical Chemistry*, Wiley, New York, **1994**, p. 61.
27. Ugland, K.; Lundanes, E.; Greibrokk, T.; Bjorseth, A.; *J. Chromatogr.* **1981**, *213*, 83.
28. Terashima, C. Rao, T.N.; Sarada, B.V.; Tryk, D.A.; Fujishima, A.; *Anal. Chem.* **2002**, *74*, 895.
29. Mardones, C.; Rios, A.; Valcarcel, M.; *Electrophoresis*, **1999**, *20*, 2922.
30. Martinez, D.; Pocurull, E.; Marce, R.M.; Borull, F.; Calull, M.; *J. Chromatogr.* **1996**, *734*, 367.
31. Gonnord, M.F.; Collet, J.; *J. Chromatogr.* **1993**, *645*, 327.
32. Jauregui, O.; Puignou, L.; Galceran, M.T.; *Electrophoresis* **2000**, *21*, 611.
33. Hilmi, A.; Luong, J.H.T.; Nguyen, A.; *J. Chromatogr.* **1997**, *761*, 259.
34. Luong, J.H.T.; Hilmi, A.; Nguyen, A.; *J. Chromatogr.* **1999**, *864*, 323.
35. Wang, J.; Chatrathi, M.P.; Tian, B.; *Anal.Chim. Acta* **2000**, *416*, 9.

36. Gaitonde, C.D.; Pathak, P.V.; *J. Chromatogr.* **1990**, *514*, 389.
37. Gattrell, M.; Kirk, D.W.; *J. Electrochem. Soc.* **1993**, *140*, 903.
38. Gattrell, M.; Kirk, D.W.; *J. Electrochem. Soc.* **1993**, *140*, 1534.
39. Doble, P.; Haddad, P.R.; *J. Chromatogr.* **1999**, *834*, 189.
40. Olefirowicz, T.M., Ewing, A.G.; *J. Chromatogr.* **1990**, *499*, 713.
41. Woolley, A.T.; Lao, K.; Glazer, A.N; Mathies, R.A.; *Anal. Chem.* **1998**, *70*, 684.
42. Matysik, F.M.; Marggraf, D.; Glaser, P.; Broekaert, J.A.C.; *Electrophoresis* **2002**, *23*, 3711.
43. Desiderio, C.; Fanali, S.; Gebauer, P.; Bocek, P.; *J. Chromatogr.* **1997**, *772*, 81.
44. Macka, M.; Haddad, P.R.; Gebauer, P.; Bocek, P.; *Electrophoresis* **1997**, *18*, 1998.
45. Wang, T., Hartwick, R.A.; *J. Chromatogr.* **1992**, *607*, 119.
46. Li, G.; Locke, D.C.; *J. Chromatogr.* **1995**, *669*, 93.
47. Foret, F.; Fanali, S.; Ossicini, L.; Bocek, P.; *J. Chromatogr.* **1989**, *470*, 299.

## **CHAPTER 7**

# **Chlorinated Phenol Analysis Using Solid Phase Extraction Coupled with Amperometric Detection**

### **7.1. Introduction**

The analysis of phenols in water supplies is an important analytical problem because of their presence in waste water effluents and their potential to enter to water supply from point sources, such as landfills.<sup>1</sup> Capillary electrophoresis (CE) is an important analytical tool in environmental analysis.<sup>2</sup> Many of the detection methods employed with CE for chlorinated phenol analysis do not achieve the low detection limits (e.g., 1 ppb for PCP) required for water quality monitoring. Therefore, new approaches for the sensitive and stable detection of these pollutants is an important area of research. In the previous Chapter, it was demonstrated that CE-EC, with a diamond microelectrode can be used to analyze for chlorinated phenols in standard aqueous solutions down to the mid to low ppb level. The linear dynamic range can be extended and the detection limit lowered if an extraction and preconcentration step is utilized. In

this Chapter, the application of solid phase extraction (SPE) with the CE-EC method is reported.

Techniques, such as liquid-liquid (LLE), solid phase extraction (SPE) and solid-phase microextraction (SPME) are routinely used for analyte preconcentration and sample clean up. Liquid-liquid extraction (LLE), for instance, has been widely employed for analyte preconcentration and is a step in several standard methods for phenol analysis (EPA methods 604, 625 and 8041).<sup>3-5</sup> LLE, however, suffers from several undesirable features including the requirement for a large volume of organic solvent, foam formation, a lengthy analysis time and difficulty with automation. Solid phase extraction (SPE) is a sample enrichment procedure that does not suffer from the same undesirable features. SPE requires low eluent volumes, involves short analysis times, is easy to automate and can even be integrated on-line. Even in the off-line mode, it is a less time-consuming and more efficient preconcentration method than LLE. SPE is not only used to extract trace levels of organic compounds from aqueous samples but also to reduce the effect of interfering components in the sample matrix. One important parameter to be considered with SPE is the selectivity of the stationary phase for the solute of interest, especially when compounds are to be extracted from complex matrices.<sup>6</sup>

The most widely used solid phases for the extraction and enrichment of phenolic compounds are C<sub>8</sub> and C<sub>18</sub> phases chemically bonded to silica, carbon



black and polymeric resins.<sup>7-10</sup> Retention of phenols from water samples by C<sub>8</sub> and C<sub>18</sub> material is the result of a reversed-phase mechanism. The effectiveness of an extraction is given by the analyte recovery, which is defined as the ratio of the number of molecules extracted to the number of molecules loaded onto the stationary phase. Another performance parameter is the breakthrough volume. This is the maximum sample volume that can be passed through the sorbent while still maintaining, at least theoretically, 100% retention of the solute molecules. The breakthrough volume depends on the sorbent surface area available for solute retention as well as the free energy of the interaction between solute and the sorbent. In aqueous media, polar solutes have the lowest breakthrough volumes due to their high solubility in the aqueous phase particularly with C<sub>8</sub> and C<sub>18</sub> solid phases. Highly cross-linked packing materials, such as LiChrolut EN, Styrosorb and Macronet Hypersol, Isolute ENV, HYSphere-1 and ENVI-Chrom P, have higher breakthrough volumes for polar analytes.<sup>10-15</sup> These stationary phases are chemically stable over a broad range of pH, which extends the applicability of the method, and the cross-linking increases the specific surface area and allows for greater  $\pi$ - $\pi$  interaction between the analytes and the solid phase.<sup>6</sup>

The ENVI-Chrom P columns used in this work were apparently developed specifically for the extraction of polar compounds from aqueous media. The solid phase consists of small, nonionic, styrene-divinylbenzene copolymer beads that offer a much greater surface area than does a typical silica-based packing.<sup>16</sup>

Phenols are sometimes difficult to retain on C-18 modified silica under reversed phase conditions, mainly due to their greater solubility in water (at least for the less chlorinated ones) than in organic matrices. The numerous active aromatic sites available in ENVI-Chrom P columns enables strong interaction with the aromatic phenols, thereby improving the recovery rates. Retention of the phenols occurs by a reversed-phase partitioning mechanism as well as by  $\pi$ - $\pi$  interaction. Chlorinated phenol recoveries of greater than 90% have been observed with this solid phase material.<sup>16</sup>

This Chapter describes the use of off-line SPE with the CE-EC method to analyze chlorinated phenols in spiked river water. Electrochemical detection was performed with a diamond microelectrode - a new electrode material that provides a highly sensitive, reproducible and stable response for the oxidative detection of these pollutants.

## **7.2. Results and Discussion**

### **7.2.1. Separation and Amperometric Detection of Chlorinated Phenols**

As described previously, decoupling the separation voltage from the electrode signal is a critical issue in CE-EC. Decoupling was accomplished in this work by using end-column detection. The microelectrode was positioned near the end of the capillary at a distance estimated to be 20 – 30  $\mu\text{m}$ , being controlled by adjusting the capillary. The microelectrode response was relatively unaffected by the separation voltage with acceptable signal-to-noise ratios and minimal

potential shifts observed. The average peak-to peak noise at the detection potential ranged from 0.5 -1 pA.

Electrophoretic separation of the chlorinated phenols was accomplished using a mixed 10/20 mM borate/phosphate run buffer at pH 8.4, a 76-cm-long fused silica capillary (30  $\mu\text{m}$  i.d.) and a separation voltage of 20 kV.<sup>17</sup> The sample was injected electrokinetically by applying 10 kV for 3s. The injected volume of an electroosmotic flow marker, methanol, was calculated to be 1.4 nL under these conditions. Based on the migration time, the applied voltage and the column length, the EOF was calculated to be  $6.2 \times 10^{-4} \text{ cm}^2/\text{Vs}$ . After applying the detection potential, the separation voltage was then turned on, and the detection electrode's background current was allowed to stabilize prior to an injection. This usually occurred within 3 - 4 minutes after separation voltage turn-on.

Figure 7.1 displays a typical electropherogram obtained for a standard solution of 2-chlorophenol (2-CP), 3-chlorophenol (3-CP), 4-chlorophenol (4-CP), 2,4-dichlorophenol (2,4-DCP), 2,4,6-trichlorophenol (2,4,6-TCP) and pentachlorophenol (PCP). Each analyte concentration was 40  $\mu\text{M}$  and the detection potential was 1.05 V.<sup>17</sup> Separation of all six pollutants is accomplished in less than 14 min and all migration times were very reproducible over an 8-h period of use (RSD  $\leq$  0.5 %). The separation efficiencies ( $N = \frac{41.7(t_m / w_{0.1})^2}{b/a + 1.25}$ )

where  $w_{0.1}$  is the width of the peak at 10% from the base,  $b/a$  is the asymmetry

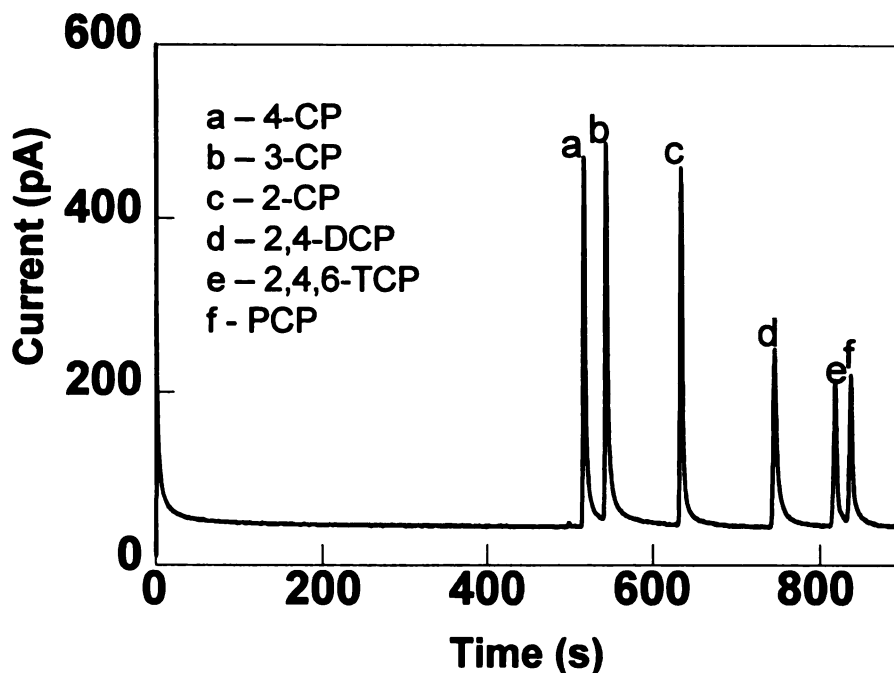


**Figure 7.1** An electropherogram for a standard solution of chlorinated phenols recorded in a 10/20 mM borate/phosphate run buffer, pH 8.4, by direct amperometry at 1.05 V (vs. Ag/AgCl). Separation voltage = 20 kV. Capillary = 30  $\mu\text{m}$  i.d. x 76 cm long. Injection = 10 kV for 3s. Solute concentration = 40  $\mu\text{M}$ .

factor) were 61,000, 78,000, 116,000, 60,000, 144,000, and 139,000 plates/m for 4-CP, 3-CP, 2-CP, 2,4-DCP, 2,4,6-TCP and PCP, respectively. The low separation efficiencies for some analytes is due to the asymmetry arising from peak tailing due to mass transport across the microelectrode during elution, as discussed previously. Previous work showed that the diamond electrode (both planar and microelectrode architectures) exhibited good figures of merit for the oxidative detection of chlorinated phenols in FIA-EC, LC-EC and CE-EC.<sup>17,18</sup> For example, the lowest concentration injected and detected via LC-EC ranged from 12 to 133 ppb, depending on the pollutant.<sup>18</sup>

### **7.2.2. Off-line Coupling of SPE with CE-EC**

The previously reported CE-EC method, using a diamond microelectrode, achieved detection limits that were below the health advisory levels of 40, 20 and 4000 ppb for 2-chlorophenol, 2,4-dichlorophenol and phenol, respectively. However, the method did not yield the 1 ppb detection limit required for pentachlorophenol. Therefore, an SPE procedure was implemented to extract the chlorinated phenols from the aqueous solution for preconcentration, thereby extending the linear dynamic range and lowering the limit of detection. Locally obtained river water was used as the sample matrix in which to test the method for the detection of chlorinated phenols. Prior to spiking with the chlorinated phenols, the river water was filtered through a nylon membrane with a 0.4  $\mu\text{m}$  pore size to remove solid particulates. The extraction process was evaluated using different applied volumes of spiked river water. By performing the analysis on a natural water sample, we were able to assess to what extent the matrix (e.g., humic and fulvic acids) of the river water affects the efficiency of the chlorinated phenol extraction. Humic matter can bind organic pollutants and cause a decrease in the breakthrough volume and a lowering of the recovery because only the soluble fraction will be enriched.<sup>13,19</sup> The interaction of pollutants with humic material will be pH dependent; therefore, the extraction of the chlorinated phenols from both acidic and neutral solution was evaluated. Preparation of the basic solution involved simply spiking the river water with the chlorinated phenols as the solution pH was  $\sim 7.5$ . Therefore, no pH adjustment was made. Preparation of the acidic solution involved spiking the river water with

the chlorinated phenols and adjusting the pH to 2.5 with a few drops of concentrated HCl. Acidification is a normal practice in water analysis in order to preserve the sample and to avoid partial deprotonation of low- $pK_a$  analytes. The recovery of each chlorinated phenol was determined by applying 50 mL of the river water spiked with 0.1 – 0.2 ppm of each chlorinated phenol. The recoveries for 2-chlorophenol, 3-chlorophenol, 4-chlorophenol, 2,4-dichlorophenol and pentachlorophenol remained fairly constant near 100 % from both low and high pH solutions, while the recovery for 2,4,6-trichlorophenol decreased from near 100% at low pH to 64 % at high pH (7-8). This decrease was caused by analyte binding with the humic acids.<sup>13</sup> Interaction of phenol having a low  $pK_a$  value with fulvic or humic acid material is known to occur at neutral pH.<sup>13</sup> Based on these results, the sample pH was adjusted to 2.5 in order to maximize the recovery of all the six pollutants. Calibration curves were prepared for standard solutions of each chlorinated phenol. Plots were made from concentrations ranging from 0.1 – 12.8 ppm for 2-chlorophenol, 3-chlorophenol and 4-chlorophenol; 0.2 – 16.3 ppm for 2,4-dichlorophenol; 0.2 – 19.7 ppm for 2,4,6-trichlorophenol and 0.3 – 26.6 ppm for pentachlorophenol (1 to 100  $\mu$ M). The linear regression correlation coefficients for all the plots were greater than 0.99. The spiked concentrations of the chlorinated phenols (0.1 to 0.2 ppm) fell within the linear dynamic range after preconcentration. Figure 7.2 shows an example of a calibration curve for the 2-chlorophenol that was used in calculation of the recovery. The percent recoveries ranged from 95 – 100% for all six pollutants as shown in Table 7.1. Given the fact that the phenols are usually present in natural water samples at trace levels,

application of a relatively large volume of a sample is often needed to achieve low limits of detection. Therefore, the percent recovery was also determined for a higher applied sample volumes (250 mL) spiked with chlorinated phenol concentrations ranging from 0.7 – 15 ppb. Good recoveries were observed for all the pollutants (greater than 95%). The relative standard deviation in the recovery values from measurement to measurement ranged between 1 and 4 %.

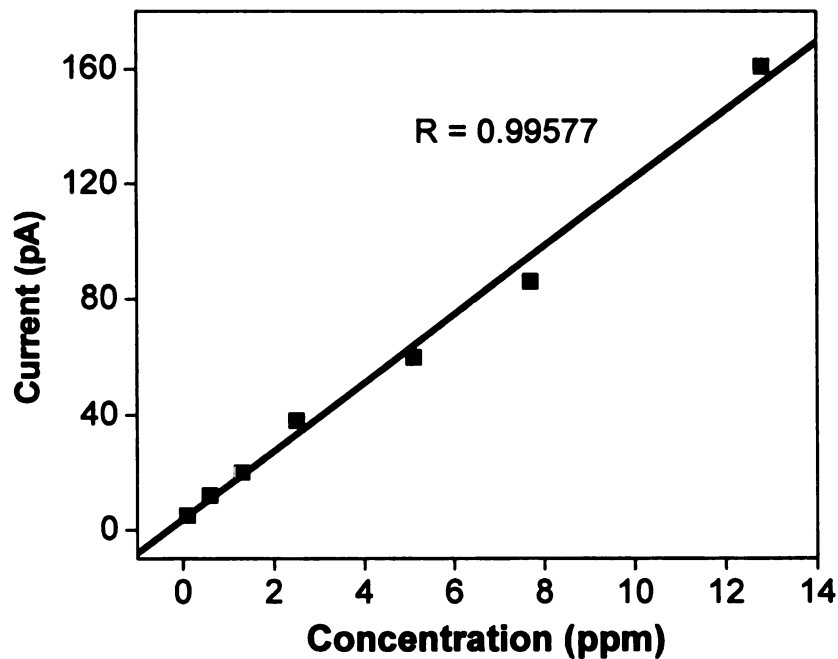


**Figure 7.2** Calibration curve for a river water sample spiked with different concentrations of 2-CP

**Table 7.1 Recovery of chlorinated phenols.<sup>c</sup>**

Analyte	% recovery	RSD% (n = 6)
2-chlorophenol	97	2.4
3-chlorophenol	96	3.0
4-chlorophenol	95	2.1
2,4-dichlorophenol	98	3.9
2,4,6-trichlorophenol	97	3.8
pentachlorophenol	100	1.0

<sup>c</sup>50 mL of the river water, pH 2.5, was spiked with 0.1 ppm of 2-CP, 3-CP and 4-CP, 0.2 ppm of 2,4-DCP and 2,4,6-TCP, and 0.3 ppm of PCP.

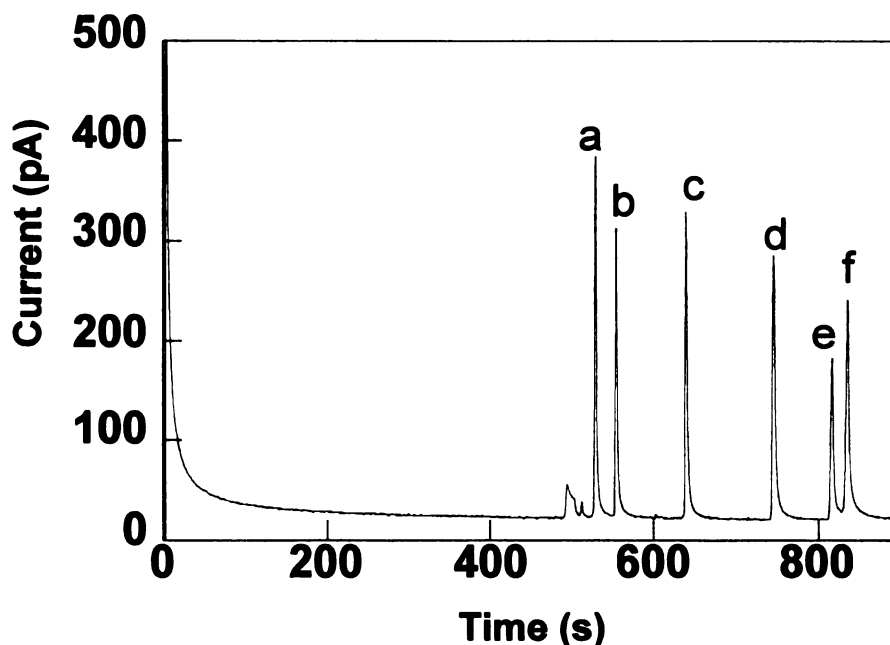


**Figure 7.3** An electropherogram for a river water SPE extract. 50 mL of the river water, pH 3.5, was spiked with 0.1 ppm of 2-CP, 3-CP and 4-CP, 0.2 ppm of 2,4-DCP and 2,4,6-TCP, and 0.3 ppm of PCP (1  $\mu$ M) and then extracted. Run buffer = 10/20 mM borate/phosphate, pH 8.4. Separation voltage = 20 kV. Capillary = 30  $\mu$ m i.d. x 76 cm long. Detection potential = 1.05 V (vs. Ag/AgCl). Injection = 10 kV for 3s.



Figure 7.3 shows a typical electropherogram obtained after SPE. The chlorinated peaks are sharp and well resolved for all six pollutants. Good separation efficiencies were obtained with plate numbers greater than 100,000 plates/m for all the analytes. A distorted peak of unknown origin appeared with a migration time of ~ 500 s. This peak was more pronounced in samples containing lower concentrations of the chlorinated phenols, but did not appear to interfere with the quantitation of the analytes. The response linearity for the total procedure was checked using 250 mL of river water spiked with different concentrations of each chlorinated phenol ranging from 0.02 – 200 ppb. Table 7.2 presents a summary of the separation and detection figures of merit. A wide linear dynamic range was achieved for each pollutant with correlation coefficients greater than 0.997. The linear dynamic range was 0.02 – 100 ppb for 2-chlorophenol, 3-chlorophenol and 4-chlorophenol, 0.04 – 130 ppb for 2,4-dichlorophenol, 0.2 – 150 ppb for 2,4,6-trichlorophenol and 0.05 – 200 ppb for pentachlorophenol. The good response sensitivity of the diamond microelectrode, as well as low peak-to-peak background noise (0.5 – 1 pA), enabled minimum detectable concentrations in the high ppt to low ppb range for all the pollutants. Good peak height response reproducibility was observed for all the pollutants with a nominal value of 5.4 %, or less. In summary, the diamond microelectrode exhibited good electroanalytical performance with a low peak-to-peak noise (0.5 to 1 pA), a low and stable background current under the electrophoretic conditions imposed, and a stable and reproducible response for the chlorinated phenols with no evidence of any electrode deactivation during

**Table 7.2 Detection Figures of Merit for Chlorinated Phenols using off-line SPE with Capillary Electrophoresis and Amperometric Detection<sup>d</sup>**

Analyte	LDR (ppb)	Sensitivity (pA/nM)	Response Precision (n=9)	LOQ (ppb)	Separation Efficiency (plates/m)
2-CP	0.02 – 100 $r^2 = 0.9984$	$3.2 \pm 1.4$	4.6	0.02 (S/N = 8)	185,000
3-CP	0.02 – 100 $r^2 = 0.9988$	$5.0 \pm 1.2$	5.2	0.02 (S/N = 3)	188,000
4-CP	0.02 – 100 $r^2 = 0.9979$	$5.3 \pm 0.8$	4.5	0.02 (S/N = 4)	179,000
2,4-DCP	0.04 – 130 $r^2 = 0.9982$	$1.9 \pm 0.5$	5.0	0.04 (S/N = 3)	173,000
2,4,6-TCP	0.20 – 150 $r^2 = 0.9998$	$1.2 \pm 0.3$	5.4	0.20 (S/N = 3)	292,000
PCP	0.05 - 200 $r^2 = 0.9991$	$1.7 \pm 0.8$	5.2	0.05 (S/N = 3)	172,000

<sup>a</sup> CE-EC parameters:  $E_{inj} = 10$  kV;  $t_{inj} = 3$  s; capillary dimensions = 30  $\mu$ m i.d. x 76 cm long;  $E_{sep} = 20$  kV; and  $E_{det} = 1.05$  V. LOQ = limit of quantitation (the minimum concentration of analyte injected and measured). The data is based on the response of 3 diamond microelectrodes.

extended use. Additionally, no pretreatment was required for electrode activation making the procedure more reproducible and less time consuming. The low and stable peak-to-peak variations in the background current allowed for low detection limits to be achieved. These results are in agreement with previous reports that diamond thin-film electrodes are useful for the stable detection of chlorinated phenols with high resistance to surface deactivation and fouling.<sup>17,18,20</sup> No deactivation of the diamond microelectrode was observed in

this work at the chlorophenol concentrations studied; therefore, an electrode could be used in measurements for weeks. The low limit of detection, the wide linear dynamic range, the excellent response precision and the superb response stability obtained with diamond shows that the SPE/CE-EC method could be employed for analysis of these priority pollutants in drinking water or in more complex environmental samples like river water. Other examples of where this method could be applied are in monitoring of chlorinated phenols in landfill leachates where the concentration ranges from the sub-ppb to ppm levels<sup>21,22</sup> or in coal tar distillation plant or wood preservation site waste in which the concentrations in waste ground water can be at ppm levels.<sup>23,24</sup>

Finally, it is important to evaluate how this method compares against others reported on in the literature. In general, it appears that no analytical method, without some form of sample enrichment, is capable of achieving the low detection limit required for PCP (1 ppb), as mandated by EPA. SPE is now a common sample enrichment method that can be utilized in combination with any analytical method to increase the linear dynamic range and to lower the detection limit for an analyte.<sup>25</sup> Chlorinated phenol analysis has been carried out using SPE and gas chromatography (GC), liquid chromatography (LC) and CE.<sup>2,3,13,26-33</sup> with electrochemical, UV/Vis and mass spectrometric detection. Chlorinated phenol limits of detection in the low (~ 2) to mid (~0.05) ppb range ( $S/N \geq 3$ ) are typical for preconcentration factors of 250 to 500, depending on the analyte. For example, Cheung et al. reported a detection limit for PCP of 0.05 ppb using GC-

MS.<sup>26</sup> Galceran et al. reported a detection limit of 0.04 ppb for PCP using LC-EC.<sup>27</sup> Bruijnsvoort et al. reported a detection limit of 0.2 ppb for PCP using CE-EC (MEKC).<sup>33</sup> The detection limits reproducibly obtained with the CE-EC method are as good or better than those reported in the literature. Moreover, the response reproducibility for this CE-EC method is superior to that reported for the other methods. The most noteworthy feature of this method, as compared to the others using electrochemical detection, is the stable response and the fact that no reconditioning or self-cleaning is necessary for optimum electrode performance.

### **7.3. Conclusions**

An analytical method with improved detection figures of merit over commonly employed methods is described for chlorinated phenol analysis in river water. SPE was employed for sample enrichment and CE-EC was used for efficient separation and detection of the electroactive chlorinated phenols. A key enabling feature of this method is the use of a diamond microelectrode for electrochemical detection. The method provides detection figures of merit superior to other methods reported on in the literature and exceeds EPA requirements for drinking water monitoring in terms of the MCL for pentachlorophenol (1 ppb) and the health advisory action levels for 2-chlorophenol, 2,4-dichlorophenol and phenol (40, 20 and 4000  $\mu\text{g/L}$  (ppb), respectively). Diamond outperforms all other bare metal and carbon electrodes for the amperometric detection of chlorinated phenols, in large part, because of

its resistance to deactivation and fouling. Rapid deactivation and fouling plague EC detection with other electrode materials and limit its application for the detection of phenols and chlorinated phenols. Diamond exhibited good electroanalytical performance with a low peak-to-peak noise (0.5 to 1 pA), a low and stable background current under the electrophoretic conditions imposed, and a sensitive, reproducible and stable oxidation response for the chlorinated phenols over many days to weeks of use. Reproducible detection limits for all the chlorinated phenols were in the mid ppt range with the exception of 2,4,6-trichlorophenol which was in the high ppt range. The power of CE separations, the simplicity of electrochemical detection, and the properties of this new electrode material render this method viable for chlorinated phenol analysis in real water.

## 7.4. References

1. Heberer, T.; Stan, H.; *Anal. Chim. Acta.* **1997**, *341*, 21.
2. Martinez, D.; Cugat, M.J.; Borrull, F.; Calull, M. *J. Chromatogr. A*, **2000**, *902*, 65.
3. EPA Method 604, *Phenols*, in Federal Register, Environmental Protection Agency, Part VIII, 40 CFR Part 136, Washington DC, **1984**, 58.
4. EPA Method 625, *Base/Neutrals and Acids*, in Federal Register Environmental Protection Agency, Part VIII, 40 CFR Part 136, Washington DC, **1984**, 153.
5. EPA Method 8041, *Phenols by Gas Chromatography: Capillary Column Technique*, Environmental Protection Agency, Washington DC, **1995**, 1.
6. Leon-Gonzalez, M.E.; Prez-Arribas, L.V. *J. Chromatogr. A* **2000**, *902*, 3.
7. Pocurull, E.; Marce, R.M.; Borrull, F.; *Chromatographia.* **1995**, *41*, 521.
8. Achilli, G.; Cellerino, G.P.; Melzi d'Eril, G.; Bird, S.; *J. Chromatogr. A* **1995**, *697*, 357.
9. Somsen, G.W.; Jagt, I.; Gooijer, C.; Velthorst, N.H.; Brinkman, U.A.Th, Visser, T.; *J. Chromatogr. A* **1996**, *756*, 145.
10. Pichon, V.; Hennion, M.C.; *J. Chromatogr. A* **1994**, *665*, 269.
11. Pocurull, E.; Marce, R.M.; Borrull, F.; *J. Chromatogr. A* **1996**, *738*, 1.
12. Fiehn, O.; Jekel, M.; *Anal. Chem.* **1996**, *68*, 3083.
13. Puig, D.; Barcelo, D.; *J. Chromatogr. A* **1996**, *733*, 371.
14. Rodriguez, I.; Llompарт, M.P.; Cela, R.; *J. Chromatogr. A* **2000**, *885*, 291.
15. Pocurull, E.; Calull, M.; Marce, R.M.; Borrull, F.; *J. Chromatogr. A* **1996**, *719*, 105.
16. Supelco, *Application Notes*, [www.sigma-aldrich.com](http://www.sigma-aldrich.com) accessed February 2005

17. Muna, G.W.; Quaiserova-Mocko, V.; Swain, G.M.; *Electroanalysis*, **2005**, *17*, 1160.
18. Muna, G.W.; Tasheva, N.; Swain, G.M.; *Environ. Sci. Technol.* **2004**, *38*, 3674.
19. Porchmann, J.; Stottmeister, U.; *Chromatographia*, **1993**, *36*, 207
20. Terashima, C. Rao, T.N.; Sarada, B.V.; Tryk, D.A.; Fujishima, A.; *Anal. Chem.* **2002**, *74*, 895.
21. Vollmuth, S.; Niessner, R.; *Chemosphere* **2002**, *30*, 2317
22. Gade, B.; Layh, M.; Westermann, H.; Amsoneit, N.; *Waste Manage. Res.* **1996**, *14*, 553.
23. Thornton, S.F.; Quigley, S.; Spence, M.J.; Banwart, S.A.; Bottrell, S.; Lemer, D.N.; *J. Contam. Hydrol.* **2001**, *53*, 233.
24. Galceran, M.; Jauregui, O.; *Anal. Chim. Acta* **1995**, *304*, 75.
25. Cheung, J.; Wells, R.J.; *J. Chromatogr. A* **1997**, *771*, 203.
26. Reitzel, L. A.; Ledin, A.; *2 J. Chromatogr. A* **2002**, *972*, 175.
27. Galceran, M.; Jauregui, O., *Anal. Chim. Acta* **1995**, *304*, 75.
28. Cardellicchio, N.; Cavalli, S.; Piangerelli, V.; Giandomenico, S.; Ragone, P.; *Fresenius J. Anal. Chem.* **1997**, *358*, 749.
29. Pocurull, E.; Sanchez, G.; Borrull, F.; Marce, R.M.; *J. Chromatogr. A* **1995**, *696*, 31.
30. Bangheri, H.; Saraji, M.; *J. Chromatogr. A* **2001**, *910*, 87.
31. Mardones, C.; Rios, A.; Valcarcel, M.; *Electrophoresis*, **1999**, *20* 2922.
32. Bruijnsvoort, M.; Sanghi, S.K.; Poppe, H.; Kok, W. Th.; *J. Chromatogr. A* **1997**, *757*, 203.

## CHAPTER 8

### Summary

1. Boron-doped microcrystalline and nanocrystalline diamond exhibited a wide potential window, a low background current and good responsiveness for  $\text{Fe}(\text{CN})_6^{-3/4}$ ,  $\text{Ru}(\text{NH}_3)_6^{+2/+3}$ ,  $\text{IrCl}_6^{-2/-3}$ , and methyl viologen ( $\text{MV}^{+2/+1/0}$ ) without any surface pretreatment. The quasi-reversible voltammetry for all the couples indicated that the diamond electrodes has sufficient charge carrier density over the wide potential window range to support a rapid electron transfer. More sluggish kinetics were found for 4-tertbutylcatechol and  $\text{Fe}^{+2/+3}$ . The sluggish kinetics are attributed to weak surface adsorption for the former, and to the absence of catalyzing surface carbonyl groups for the latter.

2. Chlorinated phenols can be quantitatively oxidized at both boron-doped microcrystalline and nanocrystalline. The electro-oxidation reaction mechanism appears to proceed in a similar manner at both diamond types, regardless of the differences in film morphology and microstructure. The oxidation of phenol, 2-CP, and 4-CP leads to the formation of surface confined hydroquinone/p-



benzoquinone and catechol/o-benzoquinone redox couples, whereas the oxidation of 3-CP and PCP do not.

3. FIA-EC and HPLC-EC results indicate that chlorinated phenols can be stably and reproducibly detected at constant potential at diamond electrodes. Both microcrystalline and nanocrystalline are responsive for these analytes without extensive pretreatment and provide a stable response over time with minimal electrode fouling. The response precision for all the chlorinated phenols were 2 – 6% on both diamond types. The limits of quantitation were in low ppb levels (9 – 27 ppb).

4. The use of boron-doped diamond microelectrode in capillary electrophoresis with both direct and indirect amperometric detection yielded excellent detection figures of merit in direct amperometry in terms of the linear dynamic range, limit of quantitation, response precision, and response stability. The minimum concentration measured ( $S/N \geq 3$ ) was 100 nM (13 ppb) for 2-chlorophenol, 3-chlorophenol and 4-chlorophenol, and 500 nM (47-133 ppb) for phenol, 2,4-dichlorophenol, 2,4,6-trichlorophenol, and pentachlorophenol. Good peak height reproducibility was observed for all analytes with a nominal value of  $5.6 \pm 0.5\%$ , or less. Good detection figures of merit were also observed in indirect amperometry. The concentration limits of quantitation were 30  $\mu\text{M}$  (4 ppm) for 2- and 3-chlorophenol, and 50  $\mu\text{M}$  (8 ppm) for 2,4-dichlorophenol at a  $S/N \geq 3$ . These values are higher than those observed in direct amperometry.

The electrode response reproducibility was excellent for 10 injections with values less than  $3.2 \pm 0.7\%$  for 2-chlorophenol, 3-chlorophenol, and 2,4-dichlorophenol.

5. Coupling the CE-EC method to SPE extended the linear dynamic range and lowered the limit of detection exceeding the EPA requirements for drinking water monitoring in terms of the MCL for pentachlorophenol (1 ppb) and the health advisory action levels for 2-chlorophenol, 2,4-dichlorophenol and phenol (40, 20 and 4000  $\mu\text{g/L}$  (ppb), respectively).

Boron-doped diamond thin-film electrodes is a new electrode that provides electrochemists with a new material for a number of electrochemical technologies which could not be carried out previously due to limitation by the stability of the electrode material. Among these applications is the electrochemical detection and remediation of chlorinated phenols. Thus, with diamond, these areas of research will greatly benefit from its unique properties.

The electroanalytical assays developed in this work provide an inexpensive, reliable, fast, and sensitive method for monitoring chlorinated phenols in the aqueous environments. The methods meet the EPA recommendations for the analysis of chlorinated phenols in drinking water. Therefore, they can be implemented for electrochemical technologies for water quality monitoring without being limited by the stability of the electrode material.

MICHIGAN STATE UNIVERSITY LIBRARIES



3 1293 02736 5356